To the Graduate Council:

I am submitting herewith a dissertation written by Hanna M. Moussa " Estimation of Absorbed Fraction to the Anterior Nose from Inhaled Beta Emitters." I have examined the final copy of this dissertation for form and content and recommend that it be accepted in partial fulfillment of the requirements for the degree of Doctor of Philosophy, with a major in Nuclear Engineering.

Lawrence Townsend

Lawrence Townsend, Major Professor

We have read this dissertation
And recommend its acceptance

Keith T. Eckerman

Lawrence J. Miller

Accepted for the Council:

Interim Vice Provost and
Dean of the Graduate School

ESTIMATION OF ABSORBED FRACTION TO THE ANTERIOR NOSE FROM INHALED BETA EMITTERS

A Dissertation

Presented for the

Doctor of Philosophy Degree

The University of Tennessee, Knoxville

Hanna M. Moussa

December 2000

Copyright © Hanna M. Moussa, 2000
All rights reserved.

To my beloved wife (Dr. Naima Moustaïd Moussa) whose patience and encouragement made this journey possible, to my children Sami Ibrahim and Zaina Linda, for their love and inspiration.

ACKNOWLEDGMENTS

I wish to express my most heartfelt gratitude to my advisor, Dr. Lawrence Townsend for his guidance, support, exceptional mentoring and friendship throughout the duration of this research. I also sincerely thank Dr. K. Eckerman, from Oak Ridge National Laboratory, for his interest in this work and his insightful sharing of resources and ideas. Special appreciation is extended to Dr. R. Pevey for his time, encouragement and helpful discussions throughout this work.

I am most appreciative to Dr. Laurence Miller, Dr. A. Ruggles of the Department of Nuclear Engineering and Dr. J.E. Lyne of the Department of Mechanical, Aerospace, and Engineering Science, for their interest in this work and for devoting their valuable time to review and critique this work.

I am most grateful to both the former and the present head of the Nuclear Engineering Department, Dr. T. W. Kerlin and Dr. H. L. Dodds, for their encouragement and support during my tenure in the department. Many thanks go to Mr. Gary Graves and Mr. Richard Bailey for their unconditional technical help for the past several years. Additional thanks go to many students in the Nuclear Engineering department especially Dr. Townsend's advisees, for their help, assistance and friendship.

Finally, I express my appreciation to my wife Naima and my children Sami and Zaina. Without their patience, endless love and support, I could not have reached this milestone.

ABSTRACT

The main purpose of this research is to introduce a new and more realistic geometry for the anterior nose region (ET_1) as an alternative to the one provided in ICRP Publication 66. For a more accurate estimation of electron absorbed fraction (AF) to the nuclei of basal cells in the ET_1 region, the proposed new geometry (frustum of a cone) replaces the cylinder geometry, which was used in ICRP 66.

Since the electron absorbed fraction (AF) data in ICRP 66 are calculated based on the nose size for an adult Caucasian male, a second purpose of this research is to investigate how the nose size (different ethnic groups) and nose tissue composition (male, female and adolescent), affects the electron absorbed fraction values.

The third aim of this research is to develop a Monte Carlo program to estimate the electron energies that emerge from the surface of spherical dust particles. Given that electrons can be located anywhere between the center and the surface of the sphere, we vary the sphere radius from 0.5 to 50 μm and investigate the effects of self-absorption on the emitted electron energies and absorbed fraction.

LIST OF ACRONYMS

ICRP: The International Commission on Radiation Protection.

NCRP: The National Council on Radiation Protection and Measurements.

ET_1: The anterior nose (two nasal vestibules).

MCNP4B: The Monte Carlo Code for Neutron, Proton and Electron transport.

EGS4: The electron gamma shower code.

URT: The upper respiratory tract.

LRT: The lower respiratory tract.

LN: The lymph node.

N-P: The nasopharyngeal region.

T-B: The tracheobronchial region.

BB: The bronchial region.

bb: The bronchiolar region.

P: The pulmonary region.

AI: The alveolar-interstitial region.

AMAD: The activity median aerodynamic diameter.

TABLE OF CONTENTS

CHAPTER ..... *PAGE*

1. **Introduction** 1

1.1 Background 1

1.2 Statement of the Problem 2

1.3 Objective of the Research 4

1.4 Impact and Originality 5

2. **Literature Review** 7

2.1 Introduction 7

2.2 Review of Lung Model of ICRP Publication 2 9

2.3 Review of Lung Model of ICRP Publication 30 11

2.4 Review of the Lung Model of ICRP Publication 66 14

2.5 Model Comparison Between ICRP 30 and ICRP 66 16

2.6 Tissue Composition of the Anterior Nose (ET_1) 17

2.7 Physiology of Anterior Nose (ET1) 19

2.8 ICRP Publication 66 Model of the Nose 20

2.9 Recent Research on the Anterior Nose (ET_1) 22

2.10 Electron Absorbed Fraction (AF) 23

2.11 Use of Electron Absorbed Fraction (AF) 23

3. Monte Carlo Methods **26**

3.1 Introduction 26

3.2 History of Monte Carlo Method 27

3.3 Monte Carlo Method 29

3.4 Overview of Monte Carlo Code MCNP4B 30

3.4.1. The Specification of the Problem Geometry 31

3.4.1.1 Surface Cards 31

3.4.1.2 Cell Cards 32

3.4.2. Materials Description and Cross-Section Evaluation 33

3.4.2.1 Material Cards 33

3.4.3. Source Card 34

3.4.4. The Type of Answers or Tallies Desired 35

3.4.5. Variance Reduction Techniques 36

3.4.6. Physics Description 38

3.4.7. Energy Cut Off Card 40

3.4.8. Esteps and substeps 41

3.4.9. NPS History Cut Off Card 42

3.5 Sabrina Software 42

4. Electron Absorbed Fraction Using MCNP4B **43**

4.1 Introduction 43

4.2 Morphometric and Dosimetric Model 47

4.3 MCNP4B Input Model 48

4.3.1 Number of Histories Experiment 49

4.3.2 E step and Substeps Experiment 51

4.3.3 Physics Parameters Experiment 54

4.4 Electron Absorbed Fraction Using MCNP4B vs. EGS4 (Code Differences) 58

4.5 Source Location in the Upper Half Cylinder (Case 1) 61

4.5.1 Discussion 61

4.6 Source Location in the Lower Half Cylinder (Case 2) 63

4.6.1 Discussion 63

4.7 The Effect of Surface Area on the Electron Absorbed Fraction 65

4.7.1 10%, 25%, 50%, and 75% Increases in the Surface Area (Case 3) 65

4.7.2 Discussion 65

4.7.3 10%, 25%, 50%, and 75% Decreases in the Surface Area (Case 4) 67

4.7.4 Discussion 68

4.8 Radius Changes and Electron Absorbed Fraction (Case 5) 70

4.8.1 Discussion 70

4.9 The Effect of External Thickness on Electron Absorbed Fraction (Case 6) 72

4.9.1 Discussion 72

4.10 Electron Absorbed Fraction Using MCNP4B (Material Effect) (Case 7) 74

4.10.1 Discussion 74

4.11 Effect of Gender and Age on the Electron Absorbed Fraction (Case 8) 76

4.11.1 Discussion 77

4.12 MCNP4B vs. MCNP4C 79

4.13 Absorbed Fraction as a Function of Basal Cell Depth 79

4.14 Discussion and Conclusion 83

5. The New Nose Model (Truncated Cone Model) 88

5.1 Introduction 88

5.2 Proposed Model for the Interior Nose 90

5.3 Measurement and Calculation 91

5.4 MCNP4B Input 95

5.4.1 Surface and Cell Card for Truncated Cone Model (original case) 96

5.5 Electron Absorbed Fraction for Cylinder vs. Truncated Cone Model Using MCNP4B (Geometrical Differences) 96

5.5.1 Discussion 97

5.6 Model Validation 99

5.6.1 Discussion 101

5.7 Convergnce of Cone Electron Absorbed Fraction to Cylinder Absorbed Value 101

5.7.1 Discussion 103

5.8 Dimension of the Upper, Lower Half of the Truncated Cone 103

5.8.1 Upper Half Dimensions 105

5.8.2 Lower Half Dimensions 105

5.8.3 Source Located on the Upper Half Cone (Case Study 1).....106

5.8.4 Source Located in the Lower Half Cone (Case Study 2).....106

5.8.5 Comparisons Between Cases 1 and 2 and the Original Case 107

5.8.6 Discussion.....107

5.9 The Effect of Surface Area on the Electron Absorbed Fraction.....109

5.9.1 8%, and 45% Increases in the Surface Area (Case 3)...109

5.9.2 Comparison of Case Study 3 to the Original Case.....109

5.9.3 8%, and 45% Decreases in the Surface Area (Case 4)..111

5.9.4 Comparison of Case study 4 to the Original Case 111

5.10 The Effect of Bottom Radius on the Electron Absorbed Fraction.....113

5.10.1 8% and 45% Increases in the Bottom Radius (Case 5).113

5.10.2 Comparison Between Case 5 and the Original Case.....114

5.10.3 Conclusion 117

5.10.4 8% and 45% Decreases in the Bottom Radius (Case6).....117

5.10.5 Comparison Between Case 6 and the Original Case 119

5.10.6 Conclusion 122

5.11 Discussion and Conclusion.....122

6 The Effect of Dust Particle Size on Electron Absorbed Fractions.....126

6.1 Introduction.....126

6.2 Dust Particle Composition.....127

6.3 Dust Particle Range and Stopping Power.....128

6.4 Distance the Electron Will Travel Inside the Dust Particle.....129

6.5 Number of Histories Experiment.....132

6.6 Comparing the Average Distance Obtained From Equation 6.4 to 6.9.....135

6.7 Program Details.....137

6.8 Calculations and Results.....138

6.8.1 Discussion.....140

6.9 Program Validation.....150

6.9.1 Results.....150

6.9.2 Discussion.....155

6.10 Code, Geometry and Dust Effects on the Electron Absorbed Fraction.....155

6.11 Conclusion.....156

7 Summary, Conclusions and Recommendations for Future Work.....159

7.1 Summary and Conclusions.....159

7.2 Recommendations for Future Work.....160

REFERENCES.....163

APPENDICES **170**

PERMISSION **171**

VITA **172**

LIST OF TABLES

TABLE ..... ***PAGE***

Table 2.1 The elemental composition (percentage by mass), mass density ρ (kg m^{-3}) and electron density η_0 (m^{-2} x 10^{26}) of soft tissue 18

Table 2.2 The elemental composition (percentage by mass), mass density ρ (kg m^{-3}) and electron density η_0 (m^{-2} x 10^{26}) of newborn soft tissue 19

Table 4.1 Radionuclides (20) with the highest ET_1 dose when the effective dose is set to 20 mSv for an intake of 5 μm by workers 45

Table 4.2 The energy deposition in region 3 (basal cells region). The estimated relative error, the standard deviation and the computer running time 51

Table 4.3 The calculated Esteps in regions C_1, C_2, C_3 and C_4 corresponding to monoenergetic electrons of energy ranging from 0.0485 MeV to 4 MeV using the energy values specified in Table H.2. of ICRP Publication 66 55

Table 4.4 Energy deposition and computer running time for 0.0485, 0.07, 0.1, 0.15, 0.3, 0.8, 1.0 1.5, and 4.0 MeV electrons corresponding to the various physics parameters 56

Table 4.5 Electron absorbed fraction results using MCNP4B and EGS4 (ICRP 66) for a cylinder model, the standard deviation (for MCNP4B data), and the percentage difference 60

Table 4.6 Electron absorbed fraction results using MCNP4B for a cylinder model (the surface source distributed uniformly on the inner surface of the upper half of the cylinder) and the standard deviation 175

Table 4.7 Electron absorbed fraction taken from Table 4.5 (second column)and Table 4.6 and the percentage differences 176

Table 4.8 Electron absorbed fraction results using MCNP4B for a cylinder model (the surface source distributed uniformly only on the inner surface of the lower half cylinder) and the standard deviation 177

Table 4.9 Electron absorbed fraction taken from Table 4.5 (second column) and Table 4.8 and the percentage differences 178

Table 4.10 Electron absorbed fraction results using MCNP4B for a cylinder model (the surface source distributed uniformly on a 22 cm^2 inner cylinder surface) and the standard deviation (materials used are air and water) 179

Table 4.11 Electron absorbed fraction results using MCNP4B for a cylinder model (the surface source distributed uniformly on a 25 cm^2 inner cylinder surface) and the standard deviation (the materials used are air and water) 180

Table 4.12 Electron absorbed fraction results using MCNP4B for a cylinder model (the surface source distributed uniformly on a 30 cm^2 inner cylinder surface) and the standard deviation (the materials used are air and water) 181

Table 4.13 Electron absorbed fraction results using MCNP4B for a cylinder model (the surface source distributed uniformly on a 35 cm^2 inner cylinder surface) and the standard deviation (the materials used are air and water) 182

Table 4.14 Electron absorbed fraction taken from Table 4.5 (second column) and Table 4.10 and the percentage differences 183

Table 4.15 Electron absorbed fraction taken from Table 4.5 (second column) and Table 4.11 and the percentage differences 184

Table 4.16 Electron absorbed fraction taken from Table 4.5 (second column) and Table 4.12 and the percentage differences 185

Table 4.17 Electron absorbed fraction taken from Table 4.5 (second column) and Table 4.13 and the percentage differences 186

Table 4.18 Electron absorbed fraction results using MCNP4B for a cylinder model (the surface source distributed uniformly on a 18 cm^2 inner cylinder surface) and the standard deviation (the materials used are air and water) 187

Table 4.19 Electron absorbed fraction results using MCNP4B for a cylinder model (the surface source distributed uniformly on a 15 cm^2 inner cylinder surface) and the standard deviation (the materials used are air and water) 188

Table 4.20 Electron absorbed fraction results using MCNP4B for a cylinder model (the surface source distributed uniformly on a 10 cm^2 inner cylinder surface) and the standard deviation (the materials used are air and water) 189

Table 4.21 Electron absorbed fraction results using MCNP4B for a cylinder model (the surface source distributed uniformly on a 5 cm^2 inner cylinder surface) and the standard deviation (the materials used are air and water) 190

Table 4.22 Electron absorbed fraction taken from Table 4.5 (second column) and Table 4.18 and the percentage differences 191

Table 4.23 Electron absorbed fraction taken from Table 4.5 (second column) and Table 4.19 and the percentage differences 192

Table 4.24 Electron absorbed fraction taken from Table 4.5 (second column) and Table 4.20 and the percentage differences 193

Table 4.25 Electron absorbed fraction taken from Table 4.5 (second column) and Table 4.21 and the percentage differences 194

Table 4.26 Electron absorbed fraction results using MCNP4B for a cylinder model (the surface source distributed uniformly on a 20 cm^2 inner cylinder surface with a radius of 0.3 cm) and the standard deviation 195

Table 4.27 Electron absorbed fraction results using MCNP4B for a cylinder model (the surface source distributed uniformly on a 20 cm^2 inner cylinder surface with a radius of 0.35 cm) and the standard deviation 196

Table 4.28 Electron absorbed fraction results using MCNP4B for a cylinder model (the surface source distributed uniformly on a 20 cm^2 inner cylinder surface with a radius of 0.76394 cm) and the standard deviation 197

Table 4.29 The percentage deviations in the electron absorbed fractions for cylinders of 20 cm^2 inner surface area with 0.25 cm and 0.3 cm radius 198

Table 4.30 The percentage deviations in the electron absorbed fractions for cylinders of 20 cm^2 inner surface with 0.25 cm and 0.35 cm radius 199

Table 4.31 The percentage deviations in the electron absorbed fractions for cylinders of 20 cm^2 inner surface with 0.25 cm and 0.76394 cm radius 200

Table 4.31 The Electron absorbed fraction and its standard deviation results from using MCNP4B for a cylinder model, the surface area is 20 cm^2, the radius is 0.25 cm and the external thickness beyond the basal cells is 0.095 cm 201

Table 4.32 The Electron absorbed Fraction and its standard deviation results from using MCNP4B for a cylinder model, the surface area is 20 cm^2, the radius is 0.25 cm and the external thickness beyond the basal cells is 0.195 cm 202

Table 4.33 The percentage deviations in the electron absorbed fractions for cylinders of 20 cm^2, inner surface of 0.25 cm and 0.295 cm and 0.095 cm (thickness of soft tissue beyond the basal cell layer) 203

Table 4.34 The percentage deviations in the electron absorbed fractions for cylinders of 20 cm^2, inner surface of 0.25 cm and 0.295 cm and 0.195 cm (thickness of soft tissue beyond the basal cell layer).....204

Table 4.35 Electron absorbed fraction results using MCNP4B for a cylinder model (the surface source distributed uniformly on a 20 cm^2 inner cylinder surface, the cylinder radius is 0.25) and the standard deviation. (the materials used are air and adult male soft tissue) 205

Table 4.36 The percentage deviations in the electron absorbed fractions for cylinders of 20 cm^2 inner surface and 0.25 cm radius (materials used are air and water vs. air and soft tissue)..... 206

Table 4.37 Electron absorbed fraction results from MCNP4B for female model (the nose size is 92% of the male nose (18.4 cm^2) inner surface area with 0.25 cm radius, the material is air and adult female soft tissue and the external tissue thickness beyond the target (basal cell) is 0.195 cm..... 207

Table 4.38 Electron absorbed fraction results from MCNP4B for the adolescent model (the nose size is 50% of the male nose (10 cm^2) inner surface area with 0.25 cm radius; the material is air and newborn soft tissue; the external tissue thickness beyond the target (basal cells) is 0.095 cm).....208

Table 4.39 The percentage difference in the electron absorbed fraction for male and female cylindrical models (the materials used for male model is air and adult male soft tissue, and for the female model is air and adult female soft tissue).....209

Table 4.40 The percentage differences in the electron absorbed fraction for male and adolescent cylindrical model (the materials used for male model is air and adult male soft tissue and for adolescent model is air and newborn tissue).....210

Table 4.41 The percentage differences in the electron absorbed fraction obtained for cylinder source with 10 cm^2 inner surface area and 0.76394 cm radius using MCNP4B and MCNP4C..... 211

Table 4.42 Electron absorbed fraction results using MCNP4C for a cylinder model (the surface source distributed uniformly on a 10 cm^2 inner cylinder surface, the cylinder radius is 0.76394 cm) and the standard deviation (the materials used are air and adult male soft tissue) 212

Table 4.43 Electron absorbed fraction as a function of basal cells depths for electron energy of 100 Kev 213

Table 5.1 Electron absorbed fraction results using MCNP4B for a truncated cone model (the surface source is distributed uniformly on a 10 cm^2 inner truncated cone surface, the top and bottom radiuses are 0.3974 cm and 0.76394 cm respectively) and the standard deviation 220

Table 5.2 Electron absorbed fraction results using MCNP4B for a cylinder model (the surface source is distributed uniformly on a 10 cm^2 inner cylinder surface) and the standard deviation 221

Table 5.3 The percentage differences in the electron absorbed fractions for truncated cone model (Table 5.1) vs. cylinder model (Table 5.2), the surface source is distributed uniformly on a 10 cm^2 inner surface area in both models. The cylinder radius is 0.25 cm while the truncated cone top and bottom radii are 0.76394 cm and 0.3979 cm respectively 222

Table 5.4 Electron absorbed fraction results for outer and inner bounds of an elliptical nasal vestibule (two truncated cones of 13.159 cm^2 and 6.298 cm^2 surface areas) using MCNP4B code and the original electron absorbed fraction from Table 5.1 (truncated cone) 223

Table 5.5 Electron absorbed fraction results using MCNP4B for an open cylinder (the surface area and radius is 10 cm^2 and 0.7639 cm) and the standard deviation 224

Table 5.6 Electron absorbed fraction results using MCNP4B for an open truncated cone model (the surface area is 10 cm^2, the top and bottom circle radii are 0.3979 cm and 0.7639 cm) and the standard deviation 225

Table 5.7 Electron absorbed fraction results using MCNP4B for an open truncated cone model (the surface area is 10 cm^2, the top and bottom circle radii are 0.5199 cm and 0.7639 cm) and the standard deviation 226

Table 5.8 Electron absorbed fraction results using MCNP4B for a truncated cone model (the surface area is 10 cm^2, the top and bottom circle radii are 0.6419 cm and 0.7639 cm) and the standard deviation 227

Table 5.9 Electron absorbed fraction results using MCNP4B for a truncated cone model (the surface source is distributed uniformly on a 5 cm^2 upper half of the inner truncated cone surface) and the standard deviation 228

Table 5.10 Electron absorbed fractions for a truncated cone model with the source uniformly distributed on 10 cm^2 inner surface area (from Table 5.1a) and 5 cm^2 upper half of the inner surface area (from Table 5.4) and the percentage differences 229

Table 5.11 Electron absorbed fraction results using MCNP4B for a truncated cone model (the surface source is distributed uniformly on a 5 cm^2 lower half of the inner truncated cone surface) and the standard deviation 230

Table 5.12 Electron absorbed fractions for a truncated cone model with the source uniformly distributed on 10 cm^2 inner surface area (from Table 5.1) and 5 cm^2 lower half of the inner surface area (from Table 5.11) and the percentage differences 231

Table 5.13 Electron absorbed fraction results using MCNP4B for a truncated cone model (the surface source is distributed uniformly on a 10.8 cm^2 inner truncated cone surface) and the standard deviation 232

Table 5.14 Electron absorbed fraction results using MCNP4B for a truncated cone model (the surface source is distributed uniformly on a 14.5 cm^2 inner truncated cone surface) and the standard deviation 233

Table 5.15 Electron absorbed fractions for a truncated cone model with the source uniformly distributed on 10 cm^2 inner surface area (from Table 5.1) and 10.8 cm^2 inner surface area (from Table 5.13) and the percentage differences.....234

Table 5.16 Electron absorbed fractions for a truncated cone model with the source uniformly distributed on 10 cm^2 inner surface area (from Table 5.1) and 14.5 cm^2 inner surface area (from Table 5.14) and the percentage differences.....235

Table 5.17 Electron absorbed fraction results using MCNP4B for a truncated cone model (the surface source is distributed uniformly on a 9.2 cm^2 inner truncated cone surface) and the standard deviation 236

Table 5.18 Electron absorbed fraction results using MCNP4B for a truncated cone model (the surface source is distributed uniformly on a 5.5 cm^2 inner truncated cone surface) and the standard deviation 237

Table 5.19 Electron absorbed fractions for a truncated cone model with the source uniformly distributed on 10 cm^2 inner surface area (from Table 5.1) and 9.2 cm^2 inner surface area (from Table 5.17) and the percentage differences.....238

Table 5.20 Electron absorbed fractions for a truncated cone model with the source uniformly distributed on 10 cm^2 inner surface area (from Table 5.1) and 5.5 cm^2 inner surface area (from Table 5.18) and the percentage differences.....239

Table 5.21 Electron absorbed fraction results using MCNP4B for a truncated cone model (the inner surface area is 10 cm^2, the bottom radius is 0.825 cm) and the standard deviation.....240

Table 5.22 Electron absorbed fraction results using MCNP4B for a truncated cone model (the inner surface area is 10 cm^2, the bottom radius is 1.1077 cm) and the standard deviation.....241

Table 5.23 Electron absorbed fractions for a truncated cone model with the source uniformly distributed on 10 cm^2 inner surface area (from Table 5.1) and same source area with a bottom radius of 0.825 cm (Table 5.21) and the percentage differences 242

Table 5.24 Electron absorbed fractions for a truncated cone model with the source uniformly distributed on 10 cm^2 inner surface area (from Table 5.1) and same source area with a bottom radius of 1.1077 cm (Table 5.22) and the percentage differences 243

Table 5.25 Electron absorbed fractions for a cylinder model with the source uniformly distributed on 10 cm^2 inner surface area (from Table 5.2) and a truncated cone with the same source area and top and bottom radii of 0.3979 cm and 0.825 cm (Table 5.21) and the percentage differences 244

Table 5.26 Electron absorbed fractions for a cylinder model with the source uniformly distributed on 10 cm^2 inner surface area (from Table 5.2) and truncated cone with the same source area and top and bottom radii of 0.3979 cm and 1.1077 cm (Table 5.22) and the percentage differences 245

Table 5.27 Electron absorbed fraction results using MCNP4B for a truncated cone model (the inner surface area is 10 cm^2, the bottom radius is 0.7028 cm) and the standard deviation.....246

Table 5.28 Electron absorbed fraction results using MCNP4B for a truncated cone model (the inner surface area is 10 cm^2, the bottom radius is 0.4202 cm) and the standard deviation.....247

Table 5.29 Electron absorbed fractions for two identical truncated cones, the source uniformly distributed on 10 cm^2 inner surface area (from Table 5.1), the second truncated cone is similar to the first one except that its radius decreases by 8% of its original length and the percentage differences 248

Table 5.30 Electron absorbed fractions for two identical truncated cones, the source uniformly distributed on 10 cm^2 inner surface area (from Table 5.1), the second truncated cone is similar to the first one except that its radius decreases by 45% of its original length and the percentage differences 249

Table 5.31 Electron absorbed fractions for a cylinder model with the source uniformly distributed on 10 cm^2 inner surface area (from Table 5.2) and truncated cone with the same source area and top and bottom radius of 0.3979 cm and 0.7028 cm (Table 5.28) and the percentage differences 250

Table 5.32 Electron absorbed fractions for a cylinder model with the source uniformly distributed on 10 cm^2 inner surface area (from Table 5.2) and a truncated cone with the same source area and top and bottom radii of 0.3979 cm and 0.4202 cm (Table 5.30) and the percentage differences 251

Table 6.1 The element mass fraction for the soil composition used for the environmental dust particle 127

Table 6.2 The electron energy (MeV), the range (CSDA), and the stopping power in dust particles (results from the Matlab® program).....258

Table 6.3 The average distance the electron will travel inside the dust using 100 histories. The first column has the dust particle radius, the second and third columns have the average distances using equation 6.4 and 6.9 respectively, the fourth column has the differences between both sets of data 260

Table 6.4 The average distance the electron will travel inside the dust using 1000 histories. The first column has the dust particle radius, the second and third columns have the average distances using equation 6.4 and 6.9 respectively, the fourth column has the differences between both sets of data 261

Table 6.5 The average distance the electron will travel inside the dust using 10,000 histories. The first column has the dust particle radius, the second and third columns have the average distances using equation 6.4 and 6.9 respectively, the fourth column has the differences between both sets of data 261

Table 6.6 The average distance the electron will travel inside the dust using 100,000 histories. The first column has the dust particle radius, the second and third columns have the average distances using equation 6.4 and 6.9 respectively, the fourth column has the differences between both sets of data 262

Table 6.7 The probability in each energy bin for mono-energetic electrons of energies between 0.0485 and 4 MeV emerging from a spherical dust particle with radius of 0.500 μm 268

Table 6.8 The average electron absorbed fractions vs. energies in MeV for a spherical dust particle with a 0.500 μm radius 269

Table 6.9 The probability in each energy bin for mono-energetic electrons of energies between 0.0485 and 4 MeV emerging from a spherical dust particle with radius of 0.750 μm 270

Table 6.10 The average electron absorbed fractions vs. energies in MeV for a spherical dust particle with a 0.750 μm radius 271

Table 6.11 The probability in each energy bin for mono-energetic electrons of energies between 0.0485 and 4 MeV emerging from a spherical dust particle with radius of 1.00 μm 272

Table 6.12 The average electron absorbed fractions vs. energies in Mev for a spherical dust particlewith a 1.000 μm radius 273

Table 6.13 The probability in each energy bin for mono-energetic electrons of energies between 0.0485 and 4 MeV emerging from a spherical dust particle with radius of 1.500 μm 274

Table 6.14 The average electron absorbed fractions vs. energies in MeV for a spherical dust particle with a 1.500 μm radius 275

Table 6.15 The probability in each energy bin for mono-energetic electrons of energies between 0.0485 and 4 MeV emerging from a spherical dust particle with radius of 2 μm 276

Table 6.16 The average electron absorbed fractions vs. energies in MeV for a spherical dust particle with a 2.000 μm radius 277

Table 6.17 The probability in each energy bin for mono-energetic electrons of energies between 0.0485 and 4 MeV emerging from a spherical dust particle with radius of 2.500 μm 278

Table 6.18 The average electron absorbed fractions vs. energies in MeV for a spherical dust particle with a 2.500 μm radius....279

Table 6.19 The probability in each energy bin for mono-energetic electrons of energies between 0.0485 and 4 MeV emerging from a spherical dust particle with radius of 3.500 μm 280

Table 6.20 The average electron absorbed fractions vs. energies in MeV for a spherical dust particle with a 3.500 μm radius....281

Table 6.21 The probability in each energy bin for mono-energetic electrons of energies between 0.0485 and 4 MeV emerging from a spherical dust particle with radius of 5.000 μm 282

Table 6.22 The average electron absorbed fractions vs. energies in MeV for a spherical dust particle with a 5.000 μm radius....283

Table 6.23 The probability in each energy bin for mono-energetic electrons of energies between 0.0485 and 4 MeV emerging from a spherical dust particle with radius of 7.500 μm 284

Table 6.24 The average electron absorbed fractions vs. energies in MeV for a spherical dust particle with a 7.500 μm radius....285

Table 6.25 The probability in each energy bin for mono-energetic electrons of energies between 0.0485 and 4 MeV emerging from a spherical dust particle with radius of 10.00 μm 286

Table 6.26 The average electron absorbed fractions vs. energies in MeV for a spherical dust particle with a 10.000 μm radius....287

Table 6.27 The probability in each energy bin for mono-energetic electrons of energies between 0.0485 and 4 MeV emerging from a spherical dust particle with radius of 15.00 μm 288

Table 6.28 The average electron absorbed fractions vs. energies in MeV for a spherical dust particle with a 15.000 μm radius....289

Table 6.29 The probability in each energy bin for mono-energetic electrons of energies between 0.0485 and 4 MeV emerging from a spherical dust particle with radius of 20.00 μm 290

Table 6.30 The average electron absorbed fractions vs. energies in MeV for a spherical dust particle with a 20.000 μm radius....291

Table 6.31 The probability in each energy bin for mono-energetic electrons of energies between 0.0485 and 4 MeV emerging from a spherical dust particle with radius of 25.00 μm 292

Table 6.32 The average electron absorbed fractions vs. energies in MeV for a spherical dust particle with a 25.000 μm radius....293

Table 6.33 The probability in each energy bin for mono-energetic electrons of energies between 0.0485 and 4 MeV emerging from a spherical dust particle with radius of 35.00 μm 294

Table 6.34 The average electron absorbed fractions vs. energies in MeV for a spherical dust particle with a 35.000 μm radius....295

Table 6.35 The probability in each energy bin for mono-energetic electrons of energies between 0.0485 and 4 MeV emerging from a spherical dust particle with radius of 50.00 μm 296

Table 6.36 The average electron absorbed fractions vs. energies in MeV for a spherical dust particle with a 50.000 μm radius....297

Table 6.37 The average electron absorbed fractions vs. energies in MeV for a spherical dust particle with a 0.500 μm radius....299

Table 6.38 The average electron absorbed fractions vs. energies in MeV for a spherical dust particle with a 0.750 μm radius....300

Table 6.39 The average electron absorbed fractions vs. energies in MeV for a spherical dust particle with a 1.000 μm radius....301

Table 6.40 The average electron absorbed fractions vs. energies in MeV for a spherical dust particle with a 1.500 μm radius....302

Table 6.41 The average electron absorbed fractions vs. energies in MeV for a spherical dust particle with a 2.000 μm radius....303

Table 6.42 The average electron absorbed fractions vs. energies in MeV for a spherical dust particle with a 2.500 μm radius....304

Table 6.43 The average electron absorbed fractions vs. energies in MeV for a spherical dust particle with a 3.5000 μm radius....305

Table 6.44 The average electron absorbed fractions vs. energies in MeV for a spherical dust particle with a 5.000 μm radius....306

Table 6.45 The average electron absorbed fractions vs. energies in MeV for a spherical dust particle with a 7.5000 μm radius....307

Table 6.46 The average electron absorbed fractions vs. energies in MeV for a spherical dust particle with a 10.000 μm radius....308

Table 6.47 The average electron absorbed fractions vs. energies in MeV for a spherical dust particle with a 15.000 μm radius....309

Table 6.48 The average electron absorbed fractions vs. energies in MeV for a spherical dust particle with a 20.000 μm radius....310

Table 6.49 The average electron absorbed fractions vs. energies in MeV for a spherical dust particle with a 25.000 μm radius....311

Table 6.50 The average electron absorbed fractions vs. energies in MeV for a spherical dust particle with a 35.000 μm radius....312

Table 6.51 The average electron absorbed fractions vs. energies in MeV for a spherical dust particle with a 50.000 μm radius....313

Table 6.52 Electron absorbed fraction results for various energies MeV calculated by Monte Carlo method using equation 6.4 and using the real radius for a dust particle radius of 2.5 μm....314

Table 6.53 Electron absorbed fraction results for various energies MeV calculated by Monte Carlo method using equation 6.4 and using the real radius for a dust particle radius of 5.0 μm....315

Table 6.54 Electron absorbed fraction results for various energies MeV calculated by Monte Carlo method using equation 6.4 and using the real radius for a dust particle radius of 20 μm....316

Table 6.55 Electron absorbed fraction results for various energies MeV calculated by Monte Carlo method using equation 6.4 and using the real radius for a dust particle radius of 50 μm....317

Table 6.56 Electron absorbed fraction for cylinder model using EGS4 (in absence of dust particle) vs. electron absorbed fraction for truncated cone using MCNP4B (in the presence of 20 μm radius) and the percentage differences....318

LIST OF FIGURES

FIGURE ..... *PAGE*

Figure 2.1 Regions of deposition used in the respiratory model of ICRP 2 10

Figure 2.2 Regions of deposition and retention used in the respiratory tract model of ICRP 30 12

Figure 2.3 Deposition of dust in the respiratory system used in the lung model of ICRP 30 13

Figure 2.4 Anatomical region of respiratory tract 15

Figure 2.5 Anatomy of extrathoracic region 16

Figure 2.6 Model of target cell nuclei (basal cells) in wall of ET_1 region (nasal vestibule) 18

Figure 2.7 Lateral wall of each half of the nasal cavity 20

Figure 2.8 Source on the inner surface of ET_1 region 21

Figure 3.1 The event log for an incident neutron on fissionable materials 30

Figure 4.1 The equivalent dose (Sv) to ET_1 region as a result of inhalation intake by workers limited to an effective dose of 20 mSv of Type F, M, and S chemical forms 45

Figure 4.2 The geometric model used to derive the electron absorbed fraction data for electrons in ET_1 50

Figure 4.3 Electron absorbed fraction (AF) results from MCNP4B and EGS4 codes for a cylinder model vs. energy (MeV) 59

Figure 4.4 Electron absorbed fraction vs. Energy (MeV) taken from Table 4.5 (cylinder with the source equally distributed on its inner surface area (20 cm^2) and from Table 4.6 (cylinder with the source equally distributed on its upper half inner surface) 62

Figure 4.5 Electron absorbed fraction vs. Energy (MeV) taken from Table 4.5 (cylinder with the source equally distributed on its inner surface area (20 cm^2) and from Table 4.8 (cylinder with the source equally distributed on its lower half inner surface) 64

Figure 4.6 Electron absorbed fraction vs. energy (MeV) for cylinders with inner surface areas of (1) 20 cm^2, (2) 22 cm^2, (3) 25 cm^2, (4) 30 cm^2, and (5) 35 cm^2 66

Figure 4.7 Electron absorbed fraction vs. energy (MeV) for cylinders with inner surface areas of (1) 20 cm^2, (2) 18 cm^2, (3) 15 cm^2, (4) 10 cm^2, and (5) 5 cm^2 69

Figure 4.8 Electron absorbed fraction vs. Energy (MeV) for cylinders with radii of (1) 0.25 cm, (2) 0.3 cm, (3) 0.35 cm and (4) 0.76394 cm respectively 71

Figure 4.9 Electron absorbed fraction results from using MCNP4B for three cylinders (the external thickness beyond the basal cells are (1) 0.295 cm, (2) 0.195 cm and (3) 0.095 cm respectively, the surface area is 20 cm^2 and the radius is 0.25 cm) 73

Figure 4.10 Electron absorbed fraction results using MCNP4B for two identical cylinders (the materials used are(1) air and water and (2) air and tissue) 75

Figure 4.11 Electron absorbed fraction vs. energy (MeV) for male, female and adolescent cylindrical models (note the materials used are air and soft tissue) 78

Figure 4.12 Electron Absorbed fractions in all ET_1 regions using the cylinder model and MCNP4B code 80

Figure 4.13 Electron absorbed fraction in the basal cells region using MCNP4 (B&C) and a cylinder model (10 cm^2 inner surface area and 0.76394 cm radius) 81

Figure 4.14 Electron absorbed fraction in the basal cells region using MCNP4C and a cylinder model (10 cm^2 inner surface area and 0.76394 cm radius) for energies from 0.06 MeV to 0.09 MeV 82

Figure 4.15 Electron absorbed fraction vs. distance (μm) from the surface source for 100 Kev incident electron 84

Figure 5.1 The shape of Mr. Moussa's right nasal vestibule 92

Figure 5.2 The proposed model for one vestibule and all covered layers 93

Figure 5.3 Electron absorbed fractions for cylinder models (0.25 cm radius, 20 cm^2 and 10 cm^2 surface areas) and a truncated cone model (10 cm^2 surface area and 0.76394 cm and 0.39788 cm bottom and top radius) 98

Figure 5.4 Two truncated cones bounding the elliptical nasal vestibule, all three regions have the same height (2.57 cm) 100

Figure 5.5 Electron absorbed fraction for the original, outer and inner truncated cones 102

Figure 5.6 Electron absorbed fraction vs. Energy (MeV) using cylinder and truncated cone models 104

Figure 5.7 Electron absorbed fractions for the truncated cone models vs. Energy (MeV) 108

Figure 5.8 Electron absorbed fractions vs. energy (MeV) for the truncated cone model (different surface areas) 110

Figure 5.9 Electron absorbed fraction using different truncated cone surface area vs. energy (MeV) 112

Figure 5.10 Electron absorbed fraction ratio for the truncated cone with bottom radius of 0.825 cm to the original truncated cone (bottom radius of 0.76394 cm) 115

Figure 5.11 Electron absorbed fraction ratio for the truncated cone with bottom radius of 1.1077 cm to the original truncated cone (bottom radius of 0.76394 cm) 116

Figure 5.12 Percentage differences in the electron absorbed fractions listed in Tables 5.25 and 5.26. 118

Figure 5.13 Electron absorbed fraction ratio for truncated cone with bottom radius of 0.7028 cm to the original truncated cone (bottom radius of 0.76394 cm)....120

Figure 5.14 Electron absorbed fraction ratio for truncated cone with bottom radius of 0.4202 cm to the original truncated cone (bottom radius of 0.76394 cm)....121

Figure 5.15 Percentage differences in the electron absorbed fractions obtained from Table 5.31 and Table 5.32 123

Figure 6.1 The birth of an electron in spherical volume and the distance it will travel to the surface 131

Figure 6.2 100 random numbers generated 133

Figure 6.3 1000 random numbers generated 134

Figure 6.4 10,000 random numbers generated 134

Figure 6.5 100,000 random numbers generated 134

Figure 6.6 Distance traveled by an electron using equations 6.4 and 6.9 (100 histories are used) 135

Figure 6.7 Distance traveled by an electron using equations 6.4 and 6.9 (1000 histories are used) 136

Figure 6.8 Distance traveled by an electron using equations 6.4 and 6.9 (10,000 histories are used) 136

Figure 6.9 Distance traveled by electron using equations 6.4 and 6.9 (100,000 histories are used) 137

Figure 6.10 Electron absorbed fraction vs. energy (MeV) for dust particle radii of (1) 1 μm, (2)2.5 μm, (3) 7.5 μm, (4) 20 μm, (5) 50 μm , and (6) for absorbed fractions obtained from ICRP 66 (no self-absorption). 139

Figure 6.11 Histogram of electron absorbed fraction vs. energy (MeV). (1) values are displayed from ICRP 66 (no self-absorption) and (2) with the effect of self-absorption in a 1.5 μm particle radius (small dust particle size) 141

Figure 6.12 Histogram of electron absorbed fraction vs. energy (MeV). (1) values are displayed from ICRP 66 (no self-absorption) and (2) with the effect of self-absorption in a 2 μm particle radius (small dust particle size) 142

Figure 6.13 Histogram of electron absorbed fraction vs. energy (MeV). (1) values are displayed from ICRP 66 (no self-absorption) and (2) with the effect of self-absorption in a 2.5 μm particle radius (small dust particle size) 143

Figure 6.14 Histogram of electron absorbed fraction v. energy (MeV). (1) values are displayed from ICRP 66 (no self-absorption) and (2) with the effect of self-absorption in a 10 μm particle radius (intermediate dust particle size) 144

Figure 6.15 Histogram of electron absorbed fraction vs. energy (MeV). (1) values are displayed from ICRP 66 (no self-absorption) and (2) with the effect of self-absorption in a 15 μm particle radius (intermediate dust particle size) 145

Figure 6.16 Histogram of electron absorbed fraction vs. energy (MeV). (1) values are displayed from ICRP 66 (no self-absorption) and (2) with the effect of self-absorption in a 20 μm particle radius (intermediate dust particle size) 146

Figure 6.17 Histogram of electron absorbed fractions vs. energy (MeV). (1) values are displayed from ICRP 66 (no self-absorption) and (2) with the effect of self-absorption in a 25 μm dust radius (large dust particle size) 147

Figure 6.18 Histogram of electron absorbed fraction vs. energy (MeV). (1) values displayed from ICRP 66 (no self-absorption) and (2) with the effect of self-absorption in a 35 μm particle radius (large dust particle size) 148

Figure 6.19 Histogram of electron absorbed fraction vs. energy (MeV). (1) values are displayed from ICRP 66 (no self-absorption) and (2) with the effect of self-absorption in a 50 μm dust radius (large dust particle size) 149

Figure 6.20 Electron absorbed fraction vs. energy (MeV) using (1) cylinder with no-self absorption, (2) truncated cone with no self-absorption, (3) truncated cone with self absorption (monte carlo program), (4) truncated cone with self-absorption (equation 6.4), and (5) truncated cone with self-absorption (actual radius 2.5 μm). 151

Figure 6.21 Electron absorbed fraction vs. energy (MeV) using (1) cylinder with no-self absorption, (2) truncated cone with no self-absorption, (3) truncated cone with self absorption (monte carlo program), (4) truncated cone with self-absorption (equation 6.4), and (5) truncated cone with self-absorption (actual radius 5 μm). 152

Figure 6.22 Electron absorbed fraction vs. energy (MeV) using (1) cylinder with no-self absorption, (2) truncated cone with no self-absorption, (3) truncated cone with self absorption (monte carlo program), (4) truncated cone with self-absorption (equation 6.4), and (5) truncated cone with self-absorption (actual radius 20 μm). 153

Figure 6.23 Electron absorbed fraction vs. energy (MeV) using (1) cylinder with no-self absorption, (2) truncated cone with no self-absorption, (3) truncated cone with self absorption (monte carlo program), (4) truncated cone with self-absorption (equation 6.4), and (5) truncated cone with self-absorption (actual radius 50 μm). 154

Figure 6.24 Comparison of the electron absorbed fraction for the cylinder model using (1) EGS4 code in the absence of self-absorption and the electron absorbed fraction obtained with (2) MCNP4B for a truncated cone with self-absorption by a 20 μm dust particle 157

LIST OF PLATES

1. CD –ROM- Appendices ..... In Pocket

CHAPTER 1

Introduction

1.1 Background

Increasing knowledge of the anatomy and physiology of the respiratory tract make it possible to estimate more accurately the exposure/dose from inhaled radioactive particles. Consequently, the National Council on Radiation Protection and Measurements (NCRP) and the International Commission on Radiation Protection (ICRP) issued recent reports (NCRP No.125 and ICRP Publication 30) to reflect these new developments. Moreover, rapid innovations in technology and computer software have inspired researchers to develop new approaches to apply this technology to various fields including anatomy and dosimetry.

The nasal vestibule region (ET_1) is that part of the anterior nasal cavity extending from the nostrils to the curved ridge of the limen nasi. As indicated in ICRP Publication 66 (ICRP 1994, p 12), the total surface area of the nasal vestibules in a Caucasian male is 20 cm^2 and its equivalent average diameter (air passage) is 5 mm. In ICRP Publication 66 (ICRP 1994, p 84), it is noted that the sensitive targets in the

ET_1 region are the nuclei of basal cells (cells at risk), which are assumed to occur uniformly throughout a 10 μm thick layer of tissue at 40 μm depth (ICRP 1994).

1.2 Statement of the Problem

Although several improvements were made from 1959 to 1993 to more accurately measure the dose to various anatomic regions of the respiratory tract, several deficiencies remain and additional revisions are needed. Our research focuses on the ET_1 (nasal vestibules) region. The dose is estimated to the nuclei of basal cells in the ET_1 region assuming that the deposition of radioactive materials occurs on the inner surface of the nasal vestibule (ICRP 1994, p 84). A cylindrical tube of appropriate dimensions (inner radius of 5 mm and surface area of 20 cm^2) is used to model the nasal vestibules. The Electron Gamma Shower (EGS4) transport code (Nelson *et al.* 1985), which models the production of both knock-on electrons and bremsstrahlung above a certain energy threshold (taken to be 1 keV for these calculations), was used in ICRP 66 to calculate the electron absorbed fractions for mono-energetic electrons. The materials used in the analysis were air and water to simulate tissue (ICRP 1994, p 462). It is assumed that the radionuclide source is uniformly distributed on the inner surface of the cylindrical tube (ICRP 1994, p 87). This ICRP 66 cylinder model applies to adult Caucasian males. Consequently, the resulting electron absorbed fractions are used to calculate the effective dose to Caucasian males. This calculated effective dose is relatively high in the extrathoracic airways (anterior nose) (Nelson *et al.* 1997).

Also, for dosimetery purposes, all of the electron absorbed fractions estimated in ICRP Publication 66, are assumed to be independent of the age and body size (ICRP 1994, p 87). In addition, in the above model, no consideration is made for a different nose composition (i.e., male, female and adolescent noses). Moreover, self-absorption for source particles with different sizes was not calculated in ICRP Publication 66.

Accordingly, the goal of the present research is to calculate the electron absorbed fraction to the nuclei of the basal cells located beneath the epithelium layer in the wall of the nasal vestibule region (ET_1), as illustrated in Figure 2.6. Our proposed model differs from the ICRP publication 66 model by more realistically taking into account the geometry of the airway of ET_1 region. We consider each nasal vestibule shape as the frustum of a cone. The radionuclide source is assumed to be spread uniformly on the inner surface of the frustum of the cone. The ET_1 size (the size of the frustum of the cone) is varied so that all ethnic groups are considered. We also consider the ET_1 material composition (the composition is different between male, female and adolescent) in our estimation, and investigate whether variations of the ET_1 materials significantly change the calculated electron absorbed fraction. The effect of self-absorption on the electron energy is investigated for spherical dust particles, with diameters ranging from 1 μm to 100 μm.

1.3 Objectives of the Research

The overall goal of this research is to use a novel approach to more accurately calculate the electron absorbed fraction to ET_1. First, we use the Monte Carlo code MCNP4B to reproduce the data published in ICRP Publication 66 (ICRP 1994, p. 466) considering the same model used in ICRP 66 for the ET_1 region. Also we investigate any changes in the electron absorbed fraction due to the code used, by comparing the results obtained from MCNP4B to those published in ICRP 66, which are based on the Electron Gamma Shower code (EGS4). Second, we investigate the changes in the electron absorbed fraction when a more realistic geometry is used (frustum of a cone versus cylinder) by comparing results obtained from MCNP4B for both cylinder and truncated cone models. Third, we use the Monte Carlo code MCNP4B to investigate the effect of nose size and material composition on the calculated electron absorbed fraction by varying the ET_1 size to account for different ethnic groups, genders and ages. Finally, using Matlab® software, we develop a Monte Carlo program to estimate the energies of electrons emerging from the surface of spherical particles of various diameters given that the electrons are originally emitted anywhere between the center and the surface of the dust. The self-absorption effect reduces the electron energy and consequently the electron absorbed fraction.

1.4 Impact and Originality of the Work

Several cases of cancers of the extrathoracic region ET_1 have been documented (Lodde *et al.* 1998). Sinonasal cancers have also been reported in humans as a result of exposure to cadmium and nickel (Jarup *et al.* 1998). Excess nasal cancers have been observed in patients receiving head and neck exposures (Batsaki *et al.* 1976). Sinonasal cancers were also found in humans as a result of systemic contamination by radium (Evans *et al.* 1969).

The highest deposition fractions of inhaled aerosol particles (with 5 μm AMAD) and consequently the highest doses were found in region ET_1 and ET_2 (Nelson *et al.* 1997). The most frequent site from which the basal cell carcinomas arise is the external nasal vestibule (ET_1). This risk, as discussed in ICRP Publication 66, is especially related to the inhalation of large particles because of their propensity to deposit on the first surface with which they come into contact (ICRP 1994, p 27). However, it is assumed that radioactive particles will not cause epithelial tumors, and therefore neither the dimensions of ET_1 nor the detailed morphometry of the nasal airways of people of different body sizes are available (NCRP 1997 Report No. 125, p20). By contrast, the electron absorbed fractions to ET_1 for electrons have been estimated (ICRP 1994, p 466). This estimation was based solely on a surface source. The assumption was that the radioactive particles were deposited on the inner surface of

the ET_1 (inner surface cylinder with proper dimensions) and are retained there and decay over a long period of time.

The main contribution of the present work is to investigate a new, more realistic and accurate geometry for ET_1 than the cylinder geometry used in ICRP Publication 66. This new geometry (frustum of a cone) is used with the MCNP4B code to calculate the electron absorbed fraction to the basal cells in the ET_1 region. While satisfying the main objective, we also investigate the effects of self-absorption on the electron energy. This approach is novel and provides a new, more useful and appropriate geometry to model the electron absorbed fraction from/to the ET_1 region.

CHAPTER 2

Literature review

2.1 Introduction

Inhalation via the respiratory tract and the nasal airway is the major route of entry into the human body, particularly for workers in radioactive and foreign particle environments in the workplace. However, this can also be true for the general public as a result of accidental releases of radioactive materials from industry (nuclear power plants), medical operations, and as a result of environmental radon. The biological response caused by these inhaled particles depends on several factors including, but not limited to, the following:

- The site of deposition in the respiratory tract.
- The physiological or toxic effects within the target tissue.
- The physical and chemical properties (the particulate form, size, density and hygroscopicity).

The physical and chemical properties determine the extent to which the material is inhalable. It can be entrained in air inspired through the mouth or nose, and either exhaled or deposited in the respiratory tract. It also determines the penetration of the inhaled particulate, the retention times or rates of clearance, and the rate of absorption into blood and translocation for other compartment tissues.

Other important physiological factors include breathing characteristics at the time of intake. These factors are respiratory rate and volume, breathing through the nose, mouth, or both, and whether or not respiratory tissues are normal or altered because of smoking, disease, or exposure to other toxic materials. Since the biological response depends on the above factors, estimates of health risk as a consequence of exposure to airborne radionuclides are also influenced by these factors. Therefore, it is very rare for two individuals exposed under the same circumstances to have the same biological responses and the same health consequences. Consequently, to protect workers and the general public against health effects resulting from exposure to air-borne radioactive materials, a limit should be derived for radionuclide exposure (i.e., limit of inhalation). Therefore a dosimetric modeling of the respiratory tract for radiation protection was developed taking into account the best knowledge available at that time.

2.2 Review of Lung Model of ICRP Publication 2

The 1959 report of ICRP Publication 2 on permissible dose for internal radiation was published to derive secondary limits for adult radiation workers. The ICRP Publication 2 lung model was used to derive the Maximum Permissible Concentrations (MPCs) for air that were used with great success to protect radiation workers for over 30 years. The main objective, in designing the lung model in this report, was to predict whether or not the radionuclides in the deposited particles were directly absorbed into the systemic circulation or passed through the GI tract where they might absorbed. In the ICRP publication 2 lung model (ICRP 1959, p 153), shown in Figure 2.1, the standard man respiratory tract was divided into two general regions, the upper respiratory tract (URT), and the lower respiratory tract (LRT). In ICRP Publication 10 (ICRP 1968, p 3), it is noted that the deposition of particulate matter in the respiratory tract was considered to be 50 percent in the URT, all of which was cleared to the GI tract in 1 day, and 25 percent deposition in the LRT. The fate of the deposited particles in the LRT depended upon their solubility. Readily soluble particles were assumed to be completely taken up into the body during 1 day, whereas, for other less soluble particles, half of the deposited particles (12.5 percent of the inhaled particles) were cleared mechanically to the GI tract within 1 day and the other half of the deposited particles (12.5 percent of the inhaled particles) were absorbed with a half-life of 120 days. Only the activity in the LRT region was considered in performing the

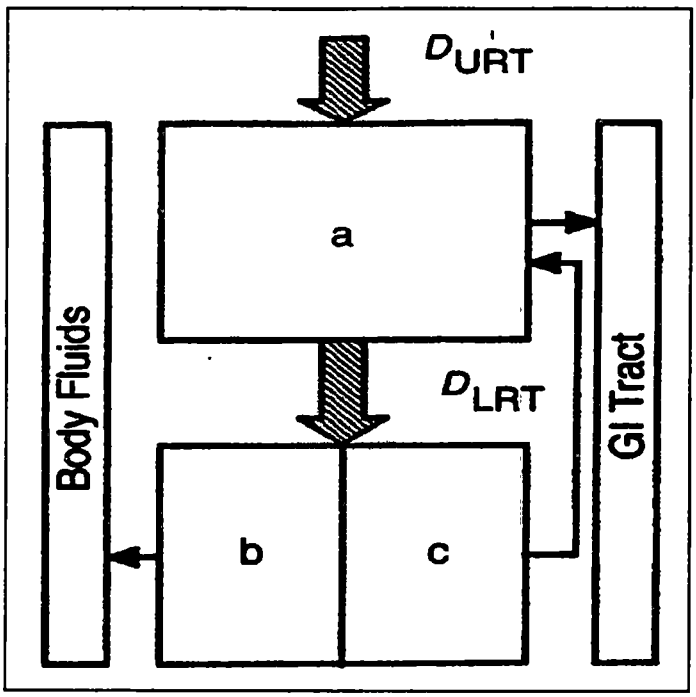


Figure 2.1 Regions of deposition used in the respiratory tract model of ICRP 2. (Reproduced with permission).

radiation dose calculations. The LRT was considered as a single homogeneous structure with no lymph nodes (LN) and a mass of 1000 g.

The limitations of the lung model of ICRP Publication 2 were:

- The lung was considered as a single 1000-gram organ.
- The deposition did not depend on the particle size.
- No crossfire from sources located in other organs was considered.
- The clearance did not depend on the solubility of the material.

- The kinetics of the lung clearance was not fully defined.
- The anatomy of the respiratory tract was not defined.

2.3 Review of Lung Model of ICRP Publication 30

The report, "Limits for Intakes of Radionuclides by Workers" was issued in ICRP Publication 30 in 1978. It was based on the 1966 report of the Task Group on Lung Dynamics. It was designed to derive secondary limits for adult radiation workers and to retain the simplicity of the ICRP Publication 2 model, while making some improvement by accounting for the aerosol diameter size in the deposition model. The respiratory tract model of ICRP Publication 30 (ICRP 1979) was much more sophisticated than that of ICRP Publication 2 in that it more clearly separated aspects of particle deposition, mechanical clearance, and dissolution of deposited particles. In ICRP Publication 30, the model divided the respiratory tract into three distinct regions (NCRP 1998): (1) the nasopharyngeal (N-P) region; (2) the tracheobronchial (T-B) region; (3) the pulmonary (P) region and the lung-associated lymph node (LN). Figure 2.2 shows the lung retention model and the above mentioned regions. These three regions have clear anatomical definitions as their names suggest. Also in ICRP Publication 30, and for the purpose of radiation protection, compounds were divided into three general solubility categories: Compounds estimated to be rapidly absorbed from P region in matter of days (Class D), moderately soluble compounds absorbed over a period of weeks to months (Class W), and relatively insoluble compounds

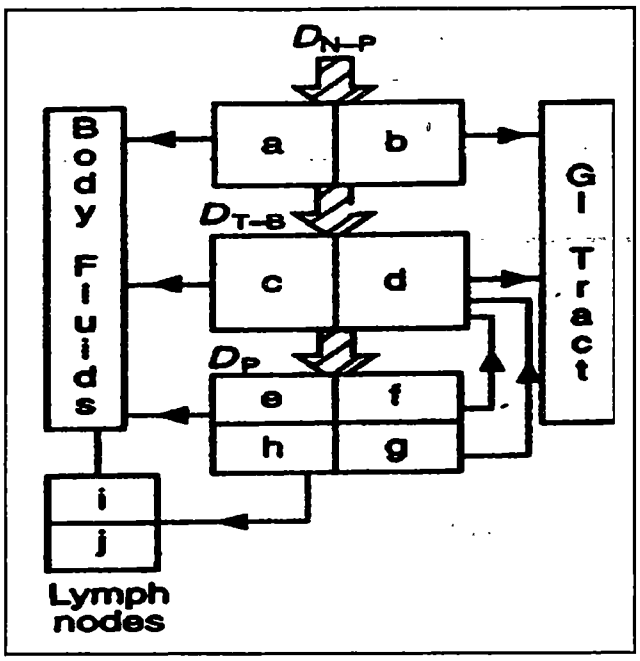


Figure 2.2 Regions of deposition and retention used in the respiratory tract model of ICRP 30. (Reproduced from ICRP 30 with permission).

absorbed over a period of years (Class Y). Moreover, the relationships between deposition and particle sizes were introduced in ICRP Publication 30. Figure 2.3 shows a plot of the deposition probability versus aerodynamic particle size. It is worth mentioning that the only respiratory tract target in Publication 30 is the lung, a 1-kg composite of the trachea, the bronchial tree, the pulmonary parenchyma, and the pulmonary lymph nodes. Therefore, the extrathoracic region (ET_1 and ET_2) has no counterpart in the Publication 30 model.

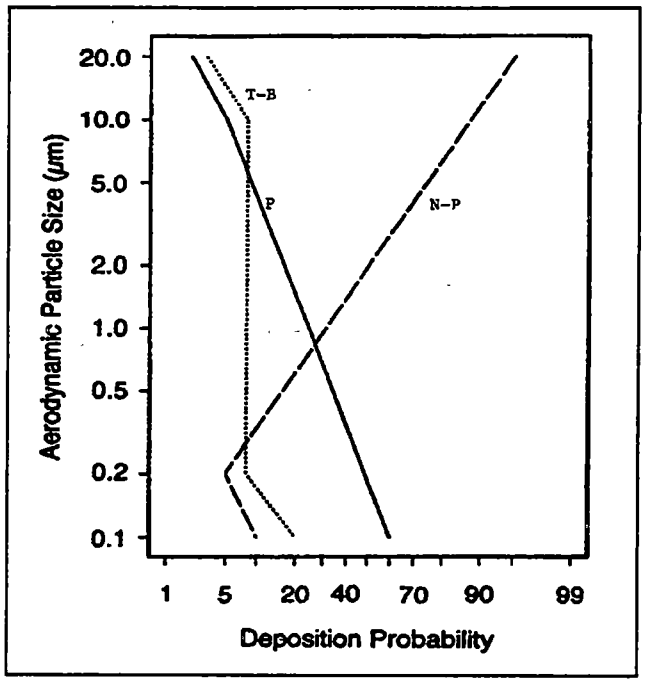


Figure 2.3 Deposition of dust in the respiratory system used in the lung model of ICRP 30. (Reproduced from ICRP 30 with permission).

The limitations of the lung model of ICRP Publication 30 were:

- The lung was still considered as a single 1000-gram organ.
- The dose to the N-P region was ignored.
- It was a conservative model designed for adult radiation workers.
- The model did not evaluate bioassay data.

2.4 Review of the Lung Model of ICRP Publication 66

The respiratory tract model shown in Figure 2.4, and published in ICRP Publication 66, is a revision of the ICRP Publication 30 model, that was motivated by an increased knowledge of anatomy. In this model the N-P region is named the extrathoracic region. The T-B region is divided into two regions, the bronchial region (BB) and the bronchiolar region (bb). The P region became the alveolar-interstitial region (AI). As noted in ICRP Publication 66 (ICRP 1994, p. 8), the lymph node system became part of all regions except the anterior nose region (ET_1). In this model the dissolution is usually represented as a simple exponential rate, which can occur from any of the compartments except the anterior nose (ET_1). There is a separate depth for critical cells for each nasal and T-B subregion. Average doses are calculated for the LN and P region. In ICRP Publication 66 (ICRP 1994, p. 8), the extrathoracic region (ET) is divided into two regions, the anterior nose (ET_1) and the posterior nose (ET_2), which includes the posterior nasal passage, larynx, pharynx, and the mouth. Figure 2.5 shows the anatomical regions of ET_1 and ET_2. The respiratory function of the anterior nose as noted in ICRP Publication 66, is an air conditioning function. Once the air passes through the nose it will be warmed, humidified and filtered, also the nasal hairs have a sensory function (ICRP 1994, p. 123). Also, the size, surface area, and configuration of the anterior nose (ET_1) is different from one person to another depending on gender, age and ethnic group (ICRP 1994, p. 19).

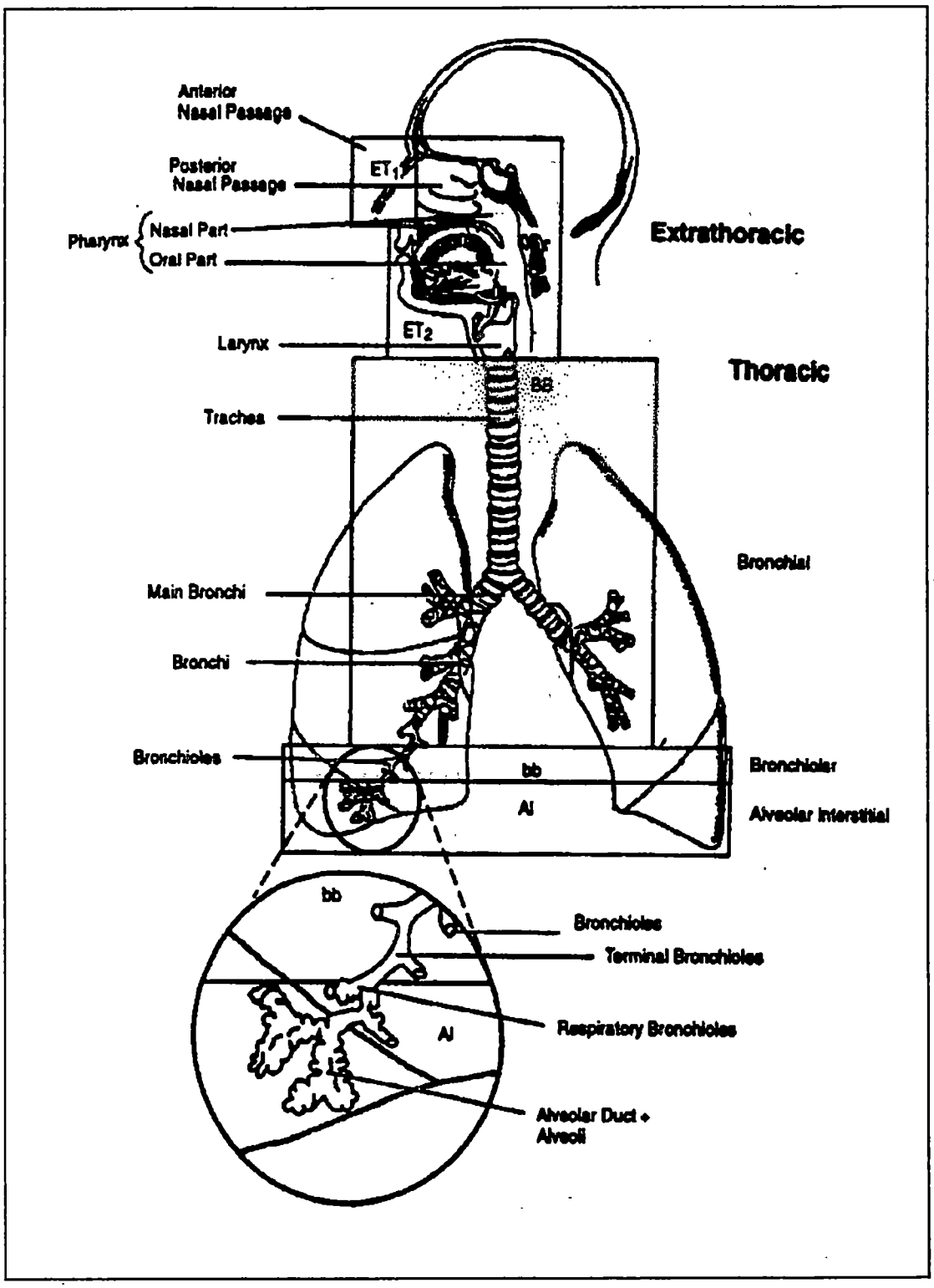


Figure 2.4 Anatomical region of respiratory tract. (Reproduced from ICRP66 with permission).

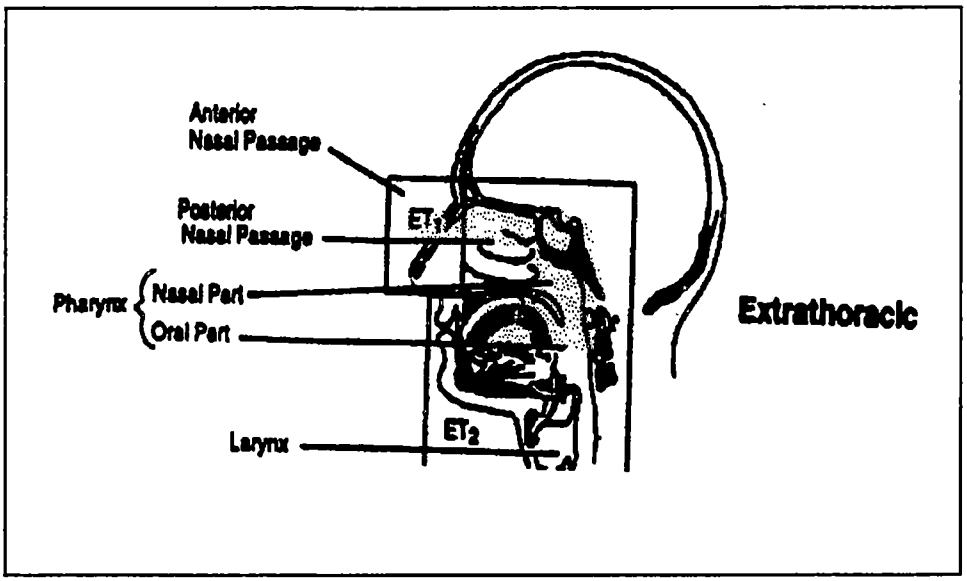


Figure 2.5 Anatomy of extrathoracic region. (Reproduced from ICRP 66 with permission).

2.5 Model Comparison Between ICRP 30 and ICRP 66

- Both models are applicable to a reference individual, not a particular person.
- ICRP 66 is designed for evaluating bioassay data while ICRP 30 is not.
- ICRP 66 is designed to be realistic instead of being conservative.
- ICRP 66 is more complex than ICRP 30.

2.6 Tissue Composition of the Anterior Nose (ET_1)

The average values for the target cell nuclei depths given in ICRP Publication 66 were estimated to be 40 to 50 μm (Bond *et al*, 1988); (Harkema *et al.* 1987), this value representing the best judgment. The wall of the ET_1 region (nasal vestibules) is lined by keratinized squamous epithelium (skin type tissue). Figure 2.6 shows a simplified model of a section through the wall of the ET_1 region. The dimensions assigned to the nasal vestibule for dosimetry purpose are indicated as follows:

A. The average thickness of keratinized stratified squamous epithelium is 50 μm.

B. The average depth of basal cell nuclei is 40 to 50 μm.

C. The total surface area is 20 cm^2.

D. The equivalent average diameter of air passage is 5 mm.

E. The tissue in the ET_1 region is considered to be a soft tissue.

The elemental compositions and densities for the soft tissue for adult males, females and newborns are given in Tables 2.1 and 2.2 taken from the International Commission on Radiation Units and Measurements report No. 46 (ICRU 1991, p 11).

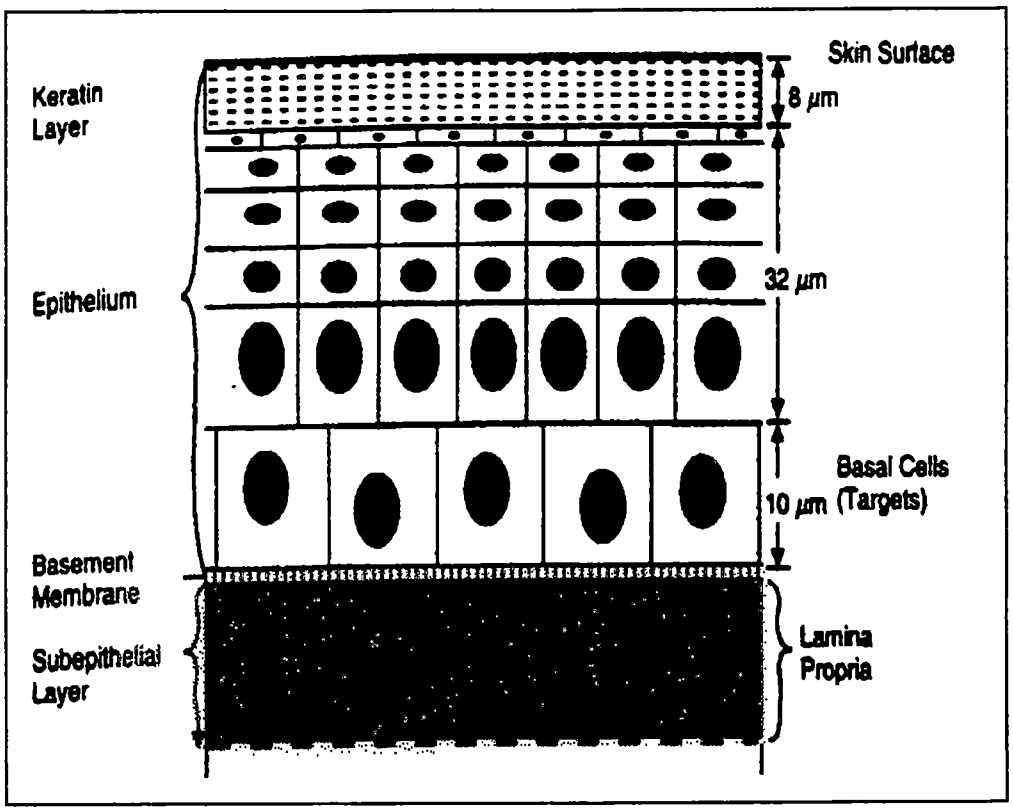


Figure 2.6 Model of target cell nuclei (basal cells) in wall of ET_1 region (nasal vestibule) (Reproduced from ICRP 66 with permission).

Table 2.1 The elemental composition (percentage by mass), mass density ρ (kg m^{-3}) and electron density η_0 (m^{-2} x 10^{26}) of soft tissue.

	H	C	N	O	Na	P	S	Cl	K	ρ	η_0
Adult Male	10.5	25.6	2.7	60.2	0.1	0.2	0.3	0.2	0.2	1030	3420
Adult Female	10.6	31.5	2.4	54.7	0.1	0.2	0.2	0.1	0.2	1020	3390

Table 2.2 The elemental composition (percentage by mass), mass density ρ (kg m^{-3}) and electron density η_0 (m^{-2} x 10^{26}) of newborn soft tissue.

	H	C	N	O	Na	Mg	P
	10.625	14.964	1.681	71.830	0.075	0.019	0.179
Newborn	S	Cl	K	Ca	Fe	ρ	η_0
	0.240	0.079	0.301	0.003	0.004	1030	3420

2.7 Physiology of the Anterior Nose (ET_1)

The anterior nose (ET_1) is pyramidal in shape. The nasal septum, in a normal nose, divides the nasal cavity into symmetrical halves. The airway starts with the nostrils. Figure 2.7 shows one nasal vestibule. Each nostril opens directly into one vestibule, the slightly extended forward portion of the nasal cavity. The vestibule is lined with skin. In its lower half are sebaceous glands and hairs protruding into the airstream. Air entering the nasal vestibule travels upward, then undergoes changes in direction beyond the nasal valve so that the air travels horizontally through the main nasal passages to the posterior nose (ET_2). The nasal valve has the smallest cross section area along the respiratory tract. It is noted by the National Council on Radiation Protection and Measurements (NCRP) that less than three percent of humans have circular nostrils, the rest have elliptical nostrils (NCRP 1997 report No. 125, p. 6). The nostrils of adults measure 1.5 cm to 2 cm anteroposteriorly and 0.5 cm to 1 cm transversely (ICRP 1994).

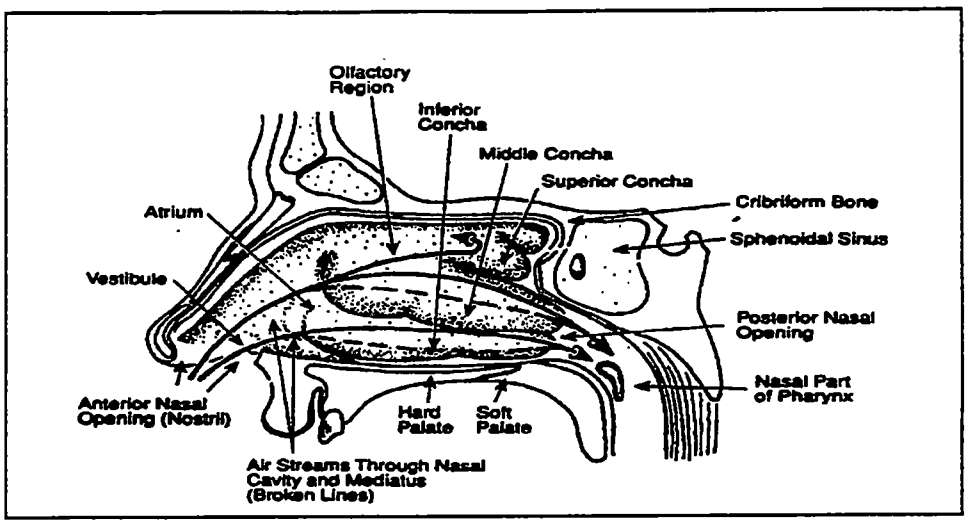


Figure 2.7 Lateral wall of each half of the nasal cavity (Reproduced from ICRP 66 with permission).

2.8 ICRP Publication 66 Model of the Nose

In ICRP Publication 66, a cylindrical tube of 5 mm diameter and an inner surface area of 20 cm^2 is used to model the nasal vestibules (ICRP 1994, p. 85). The electron absorbed fraction is calculated for the basal cell nuclei (cells at risk) located at an average depth of 40 μm (average thickness of keratinized stratified squamous epithelium). The Electron Gamma Shower (EGS4) transport code, which models the production of both knock-on electrons and bremsstrahlung above a certain energy threshold (taken to be 1 keV for these calculations), is used to calculate the electron absorbed fractions for mono-energetic electrons. As noted in ICRP 66, the materials used in the EGS4 code are air and water to simulate tissue (ICRP 1994, p. 462). Figure 2.8 shows the cross-section of the cylinder radiation source and target that apply to the interior nose region (ET_1).

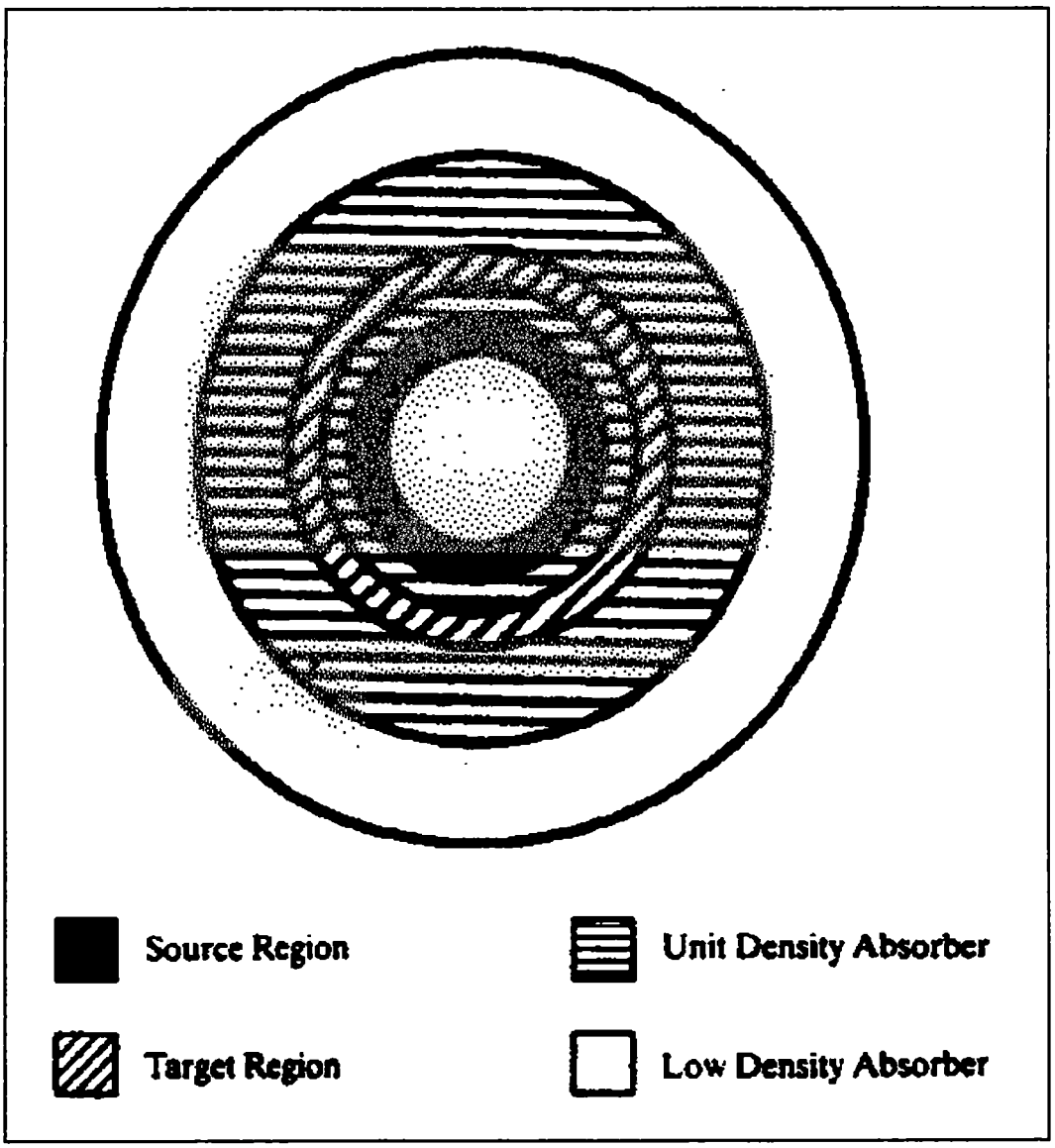


Figure 2.8 Source on the inner surface of ET_1 region (Reproduced from ICRP 66 with permission).

2.9 Recent Research on Anterior Nose (ET_1)

Since the nasal vestibule ET_1 is the first filter in the human respiratory tract model (HRTM), it has a major effect in estimating the dose from inhaled particles to the lung and to ET_1. Therefore understanding the filtration efficiency and the factors involved in this filtration is essential for the above purpose. Consequently, research has focussed in two directions:

- Define more accurately the nasal vestibule dimensions.

- Determine the effect of the nasal dimensions on the particle deposition.

Nasal vestibule dimensions vary significantly among individuals. Previous research conducted in this area (Cheng *et al.* 1996) conclude that it is necessary to include the information on the biological variability in the extrathoracic filtration (nasal vestibule dimension) to define the population-wide lung dosimetry resulting from aerosol intakes.

Computer modeling of the nasal airway and inhaled gas uptake in rats, monkeys, and humans has been performed (Subramaniam *et al.* 1998). A three-dimensional computational fluid dynamics model of airflow in rats, monkeys and in human nasal passages was described. These models can be used to answer quantitative

questions about regional delivery of an inhaled gas to specific sites of the nose, and to provide accurate information about anatomical structure and its effects on airflow and uptake in detail. Also nose shapes based on mathematical modeling of the human nasal passages were developed (Brin *et al.* 1997). None of these models were used to estimate the doses to the ET_1 from inhaled radioactive particles.

2.10 Electron Absorbed Fraction (AF)

The electron absorbed fraction (*AF*), as defined in ICRP Publication 66, is the fraction of energy emitted by a specific radiation R in a specific source tissue S that is absorbed in a specific target tissue T. The average fraction of energy absorbed in a target tissue T per emission of radiation R in source S is given by:

$$AF(T \leftarrow S)_R = E(T \leftarrow S)_R / \dot{E}_R \qquad 2.1$$

where $E(T \leftarrow S)_R$ is the average energy (in MeV) absorbed by the target tissue T per emission of radiation R in source S, and E_R is the energy (in MeV) of the radiation.

2.11 Use of Electron Absorbed Fraction (AF)

The electron absorbed fraction (*AF*) is used to calculate the Specific Effective Energy (*SEE*) which is defined as the energy (in MeV), suitably modified for radiation quality, imparted per gram of target tissue (T) as a consequence of the

emission of a specified radiation (R) from a transformation occurring in the source (S). For any given radionuclide, the specific effective energy (SEE) at age t is defined in the ICRP Publication 66 (ICRP 1994, p. 80) as

$$SEE\,(T \leftarrow S;t) = \sum_R \frac{w_R E_R Y_R AF\,(T \leftarrow S;t)_R}{M_T(t)} \qquad 2.2$$

where w_R is the radiation weighting factor for radiation R, E_R is the energy of radiation R, Y_R is the yield of radiation per nuclear transformation, and $AF\,(T \leftarrow S;t)_R$ is the fraction of the energy of radiation R emitted in S, which is absorbed in the target tissue T at age t, and M_T (t) is the mass of the target tissue at age t.

The specific effective energy *SEE* is used to calculate the equivalent dose rate at age t in organ T of an individual of age t_0 at the time of intake (inhalation or ingestion). The equation used to calculate the equivalent dose in ICRP Publication 66, is:

$$H_T(t,t_0) = c\sum_s \sum_j q_{s,j}(t) SEE(T \leftarrow S;t)_j \qquad 2.3$$

where $q_{s,j}(t)$ is the activity of radionuclide j present in source organ at age t, and $SEE(T \leftarrow S;t)$ is the total energy absorbed per unit mass in the target T. The contributions of each radiation emitted by the radionuclide are weighted by their radiation weighting factors appropriate per nuclear transformation of the radionuclide in source region S, and c is the numerical constant required by the units of q and *SEE*.

The equivalent dose in the target organ accumulated by age 70 y due to a single intake of a radionuclide at age t_0, $H_T(t_0)$ is:

$$H_T(t_0) = c\int_{t_0}^{70}\sum_s\sum_j q_{s,j}(t)SEE(T \leftarrow S;t)_j dt. \qquad 2.4$$

CHAPTER 3

Monte Carlo Methods

3.1 Introduction

Many difficult problems in mathematics, physics and other sciences can be solved or simulated by using the Monte Carlo method. A Monte Carlo method does not solve the problem explicitly but rather simulates it by performing statistical sampling experiments on a computer. It is a method that can be used to solve problems with inherent probabilistic structure as well as those without probabilistic content. The advantages of using the Monte Carlo method over similar numerical methods that make use of N-point evaluations in M-dimensional space to produce approximations is the absolute error estimation. Most methods, unless they contain special structure, have an absolute error of estimate that decreases by the function $N^{(-1/M)}$. Alternatively, the Monte Carlo method has an absolute error of estimate that decreases by the function $N^{(-1/2)}$.

3.2 History of Monte Carlo Method

This method is named after the city in the Monaco principality, east of France on the Mediterranean Sea, which is famous with its gambling casino and its roulette tables. The Monte Carlo methodology development and namesake is dated to around 1944. However, there are a number of smaller, less documented or not fully identified cases of its use much earlier than 1944. As an example, in 1768, Buffon (French mathematician Georges Louis Leclerc Comte de Buffon) (Buffon, 1777) performed his famous experiment (Needle Experiment) to estimate the value of π (3.14....). The idea of this experiment was to drop an L-length needle at random on grid of parallel D-spaced lines. For L less than or equal D we acquire the following:

$$\text{P (needle intersects the grid)} = \frac{2L}{\pi D}$$

If we drop the needle N times and count R intersections we obtain

$$\text{P} = \text{R} / \text{N}, \text{ and } \pi = \frac{2LN}{RD}.$$

In 1899 Lord Rayleigh proved a solution of parabolic differential equations could be obtained by means of an approximation with a one-dimensional random walk without absorbing barriers. In 1908 W.S. Gosset used experimental sampling as a tool to aid his discovery of the distribution of the correlation coefficient. In the same year

Gosset also used sampling to help support his derivation of t-distribution, which he had arrived at by an uncertain and incomplete theoretical analysis.

The atomic bomb effort of World War II instilled the use of the Monte Carlo methods as a serious research tool. The complexities of random neutron diffusion in fissile material gave use to the Monte Carlo method as a means of a direct simulation of the probabilistic problems created by diffusion theory. Von Neumann and Ulam developed the "Russian roulette" and "splitting" methods for the solution of these problems early on in the random neutron diffusion work (Cooper *et al.* 1989). However, Harris and Herman Kahn later did the systematic development of these concepts in 1948 (Kahn *et al.* 1950). Around 1948 Fermi, Metropolis, and Ulam used the Monte Carlo method in their estimates of the Schrodinger equation's eigenvalues.

The newly developing theory of computational complexity in the 1970's gave better rationalization for the use of the Monte Carlo method as a serious research tool. The theory proposed a class of problems, which had a solution time that grows exponentially as a function of class size or M. The modernization of computers and the development of programming languages like C and Fortran allowed for the creation of generalized codes for the implementation of the Monte Carlo method. The first general code MCS was developed by Los Alamos National Laboratory in 1963, (Johansson *et al.* 1963). Finally in the late 1970's MCNP was created as a combination of previous neutron-gamma and photon codes (Cashwell *et al.* 1973). The final stages of

development have taken the Monte Carlo through the modernization of computers and programming languages to today's MCNP4B and MCNP4C (MCNP4C was not available when this project started in 1998). This code (MCNP4B) is culmination of over 500 person-years of sustained effort and paces the Monte Carlo method as a serious and important tool in modern physics (Hendricks *et al.* 1997).

3.3 Monte Carlo Method

The Monte Carlo method used by MCNP4B (The Monte Carlo N-Particle Transport Code System) does not solve an explicit equation, but rather obtains answers by simulating particle histories and recording some aspects of their average behavior. The average behavior of particles in the physical system is then inferred from the average behavior of the simulated particles using the central limit theorem. The statistical sampling process is based on the selection of random numbers - analogous to throwing dice in a gambling casino-hence the name "Monte Carlo". In other words, the Monte Carlo sampling technique is a theoretical experiment. In this experiment, each particle will be followed from the time and place it is created (source) until its death. The terminal category (absorption, escape, knock-on, etc) and probability distributions are randomly sampled using transport data to determine the outcome of each step of its history. Figure 3.1 shows the event log for a neutron incident on fissionable materials.

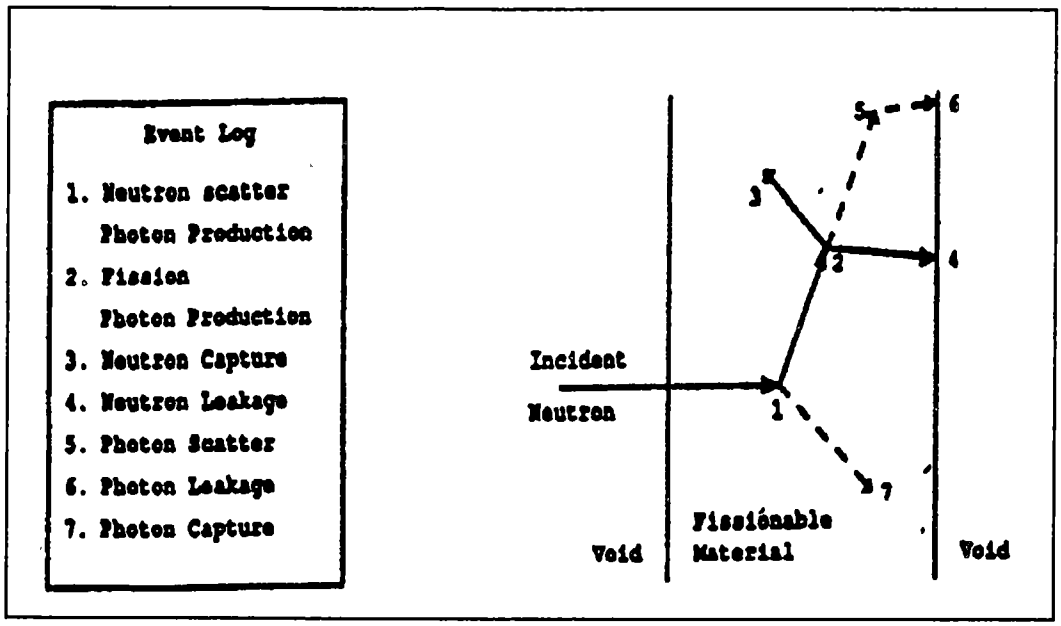


Figure 3.1 The event log for an incident neutron on fissionable materials. (Reproduced from MCNP4B manual).

3.4 Overview of Monte Carlo Code MCNP4B

Although various government and private organizations developed the Monte Carlo N-Particle Transport Code System (MCNP4B), the main contributor is the Transport Methods Group at Los Alamos National Laboratory, New Mexico. It is a general-purpose, continuous-energy, generalized-geometry, time-dependent, coupled Neutron-Photon-Electron Monte Carlo Transport Code. This code reads an input file that is created by the user. This input file (as discussed in the MCNP4B manual) contains information about the following items:

1. The specification of the problem geometry.

2. The description of the materials and selection of cross-section evaluations.

3. The location and characteristics of the neutron, photon, or electron sources.

4. The type of answers or tallies desired.

5. Any variance reduction techniques used to improve efficiency.

6. Physics description.

7. Energy cut off.

8. Number of histories desired.

3.4.1 The Specification of the Problem Geometry

The geometry of the problem can be described in the MCNP4B input deck by using two cards, a surface card and a cell card.

3.4.1.1 Surface Cards

Various types of surfaces can be expressed in the MCNP4B deck: plane, sphere, cylinder, cone, ellipsoid, hyperboloid, paraboloid...etc. Also the axes of these surfaces can be parallel to X, Y, or Z. Moreover surfaces can be expressed even if there axes are not parallel to X, Y, Z (for more information consult the MCNP4B manual

Table 3-1, page 3-14). On the surface card, the surface number is the first entry, the next entry indicates the surface type, and the remaining entries are the numerical coefficients of the equation of the surface. A point (x,y,z) is defined as having positive sense with respect to a surface when the expression for that surface evaluated at (x,y,z) is positive. Any point inside a sphere, cylinder, or cone is defined in a negative sense and outside in a positive sense. For more information consult the MCNP manual, page 1-22.

3.4.1.2 Cell Cards

The problem geometry can be specified by combining intersecting surfaces in the cell card. The first entry, the cell number, must begin in the first five columns. The second entry is the cell material number, which refers to the material number in the material card to be used. The third entry is the material density. A positive entry must be used if the user wishes to express the density in units of 10^{24} atoms/cm^3; otherwise the unit is expressed in g/cm^3. The fourth entry is the geometrical expression of the cell, which is performed by using numbers from the surface cards in combination of operators (complement operator, combination, intersection, outside and inside regions, above and below surfaces).

A copy of the MCNP4B input deck, identical to the input presented to Electron Gamma shower code (EGS4) to obtain the electron absorbed fractions to

basal cells from mono-energetic beta emitter (same geometry, same dimensions, and same materials) in ICRP Publication 66, can be found in Appendix A. In this input deck the complement operator has been used extensively to create the cell cards. The last entry on the cell cards is the cell parameters (optional), that indicate the cell's importance and the type of particles that enter these cells (neutron, photon, electron or any combination of these three particles). For more information about this subject consult the MCNP manual, page 1-24.

3.4.2 Materials Description and Cross-Section Evaluations.

The materials used in the problem can be described in the MCNP4B input deck by using the material cards.

3.4.2.1 Material Cards

The material (Mm) card is used to specify a material for all cells containing material entries. The first entry is material number (m #). The next two entries consist of the identification number (ZAID) of the constituent element or nuclide followed by the weight or atomic fraction (weight fraction if entered as a negative number of that element or nuclide). The nuclide identification number (ZAID) is used to identify the nuclide or the element to be transported in a specific problem. The form of the number as explained in MCNP4B manual is:

ZZZAAA.nnX, where

ZZZ is the atomic number of the nuclide or element.

AAA is the mass number of the nuclide, ignored for photons and electrons.

nn is the cross-section evaluation identifier; if blank or zero, a default cross-section will be used.

X is the class of data: C is continuous energy, D is discrete reaction; T is thermal; Y is dosimetry; P is photon; E is electron; and M is multigroup.

3.4.3 Source Cards

The first entry on this card is the source specification. There are four types of sources that can be expressed in MCNP: (1) the general source (SDEF); (2) the surface source (SSR); (3) the criticality source (KCODE); and (4) the user supplied source. The source distribution function can be specified on the SIn, SPn, SBn, DSn, SCn, SSW, and KSRC cards where SIn is the source information (describe the source region), the SPn is the source probability, the SBn is the source bias, DSn is the dependent source, SCn is the source comment, SSW is surface source write, and SSR is surface source read. For more information about the source specification consult the MCNP4B manual pages 3-40 and 3-53. The next entry on the source card is the source location (SUR = m, a source on surface m; POS = x, y, z, a source in a position x, y, z), the third entry is the source energy, the forth entry is the weight (WGT=w).

3.4.4 The Type of Answers or Tallies Desired

MCNP4B was designed to use seven tally types for neutron transportation, six basic photon tally types, and four basic electron tally types. All tallies are normalized per source particle unless changed by the user using the TALLYX subroutine, or normalized by weight in a criticality calculation using KCODE. The following tallies are taken from the MCNP4B manual page 3-64.

Mnemonic	TALLY Description	Fn. units	*Fn. units
F1:N or F1:P or F1:E	Current integrated over a surface	particles	MeV
F2:N or F2:P or F2:E	Flux averaged over a surface	particles/cm^2	MeV/cm^2
F4:N or F4:P or F4:E	Flux averaged over a cell	particles/cm^2	MeV/cm^2
F5a:N or F5a:P	Flux at a point or ring detector	particles/cm^2	MeV/cm^2
F:N or F6:N,P or F:P	Energy deposition averaged over a cell	MeV/g	jerk/g
F7:N	Fission energy deposition averaged over a cell	MeV/g	jerk/g
F8:P or F8:E or F8:P,E	energy distribution of pulses created in a detector.	pulses	MeV

or
+F8:E charge deposition charge

3.4.5 Variance Reduction Techniques

In Monte Carlo, the particles are transported either by analog or nonanalog models. The analog model uses the natural probabilities that various events occur (i.e., collision, fission, capture, etc.). Particles are followed from event to event, and the next event is always sampled (using the random number generator) from a number of possible next events according to the natural event probabilities. There are many cases for which the fraction of particles detected is very small, less than 10^{-6}. For these cases, the analog Monte Carlo model will fail to obtain a reliable answer. Therefore, it is more appropriate to use the nonanalog Monte Carlo Model, which attempts to follow the interesting particles that contribute more to the result rather than the uninteresting ones. The nonanalog Monte Carlo method will have the same expected tallies as the analog one if the excepted weight executing any random walk is preserved (i.e., a particle can be split into two identical pieces and the tallies of each piece are weighted by ½ of what the tallies would have been without the split). There are four classes of variance reduction techniques in MCNP:

A. *Truncation Method*: A variance reduction method in which unimportant parts of the geometry are not sampled (truncated); this method will speed up

the calculation. Specific truncation methods available in MCNP are energy cutoff and time cutoff.

B. *Population Control Method*: This method controls the number of samples taken in various regions of phase space. Many samples of low weight are tracked in an important region, while few samples of high weight are tracked in an unimportant one. An adjustment to the weight is made to ensure that the problem solution remains unbiased. Specific population control methods available in MCNP are geometry splitting and Russian roulette, energy splitting/roulette, weight cutoff, and weight windows.

C. *Modified Sampling Methods*: By this method, we alter the statistical sampling of a problem to increase the number of tallies per particles. For example, this can be done by sampling from any arbitrary distribution rather than from the physical probability as long as the particle weights are then adjusted to compensate. Modified sampling methods in MCNP include the exponential transform, implicit capture, forced collisions, source biasing, and neutron-induced photon production biasing.

D. *Partially Deterministic Methods*: The most complicated classes of variance reduction techniques. They circumvent the normal random walk process by using deterministic-like techniques, such as contorting of the random

number sequence or by next event estimators. In MCNP these methods include point detectors, DXTRAN, and correlated sampling.

Variance-reduction techniques in Monte Carlo calculations reduce the computer time required to obtain results of sufficient precision. Also, for many problems, a variance reduction technique is not just a way to speed up the problem but is absolutely necessary to get any answer at all. For more details about this subject consult the MCNP4B manual pages 2-114 to 2-142.

3.4.6 Physics Description

This card contains parameters used by the MCNP program in determining the particle physics when they are followed from event to event. For neutrons these parameters are EMAX and EMCNF, where EMAX is the upper limit for the neutron energy in MeV (entered by the user) and EMCNF is the energy boundary (MeV) above which neutrons are treated with implicit capture and below which they are treated with analog capture. For photons these parameters are EMCPF, IDES, and NOCOH. EMCPE is the upper energy limit (in MEV) for detailed photon physics treatment. IDES is set equal to 0 or 1. 0 if photons will produce electrons in MODE E (electron problem) or bremsstrahlung photons with the thick target bremsstrahlung model, and 1 if photons will not produce electrons. NOCOH can be equal to 0 or 1. 0 if coherent scattering occurs, and 1 if it does not. For electrons, these parameters are EMAX,

IDES, IPHOT, IBAD, ISTRG, BNUM, XNUM, RNOK and ENUM. EMAX is the electron energy limit in MeV (entered by the user). Electron cross sections and the stopping power data are generated on a logarithmic energy grid from the entered energy (EMAX) down to the global energy cutoff for electrons. IDES takes a value of either 0 or 1 (a switch to turn off electron production by photons). A value of 1 will turn off electron production (it does not turn off the pair production-produced annihilation photons). IPHOT takes a value of either 0 or 1 (a switch to trun off electron photon production by electrons). Avalue of 1 will trun off photon production. IBAD is a switch that takes values of either 0 or 1. 0 turns on the full bremsstrahlung angular distribution treatment. 1 turns on the simple approximate bremsstrahlung angular distribution treatment. The full detailed physics model is more accurate and just as fast as the simple treatment for electrons. ISTRG is also a switch that controls the continuous-energy slowing down treatment. If ISTRG = 1, the expected value for each collision is used; if ISTRG = 0 (default), the more realistic sampled value is used. Note that the option of using the expected value is useful for some comparisons in deterministic electron transport calculations. BNUM is used to control the sampling of bremsstrahlung photons produced along electron substeps. The default value (BNUM = 1) results in the analog number of bremsstrahlung tracks being sampled. If BNUM > 0, the number of bremsstrahlung photons produced is BNUM times the number that would be produced in the analog case. If BNUM = 0, the production of bremsstrahlung photons is turned off. XNUM is used to control the production of x-rays along the electron tracks. If XNUM = 1 (default), the analog number of tracks will be sampled, if

XNUM > 0, the number of x-ray photons produced is XNUM times the number that would be produced in the analog case. If XNUM = 0, the production of x-ray photons is turned off. RNOK is used to control the number of knock-on electrons produced in electron interactions. If RNOK = 1 (default), the analog number of tracks will be sampled. If RNOK > 0, the number of knock-on electors produced is RNOK times the analog number that would be produced in the analog case. If RNOK = 0, the production of x-ray photons is turned off. ENUM is used to control the generation of photon-induced secondary electrons. The default value (ENUM = 1) results in an analog treatment. If ENUM > 0, ENUM times the analog number of secondaries will be produced, and appropriate weight adjustment is made. If ENUM = 0, the generation of secondary electrons by photons will turned off (pair production is totally turned off). Note, because electron transport is slow, a judicious use of ENUM < 1 may often be appropriate.

3.4.7 Energy Cut Off Card

The parameters for this card are n, T, E, WC1, WC2, and SWTM, where n= N for neutrons, P for photons, and E for electrons; T = time cutoff in shakes (1 shake = 10^{-8} sec); E is the lower energy cutoff in MeV; WC1 and WC2 are weight cutoffs; SWTM is the minimum source weight. If the cutoff energies are desired for each cell, the user must use the ELPT card (cell-by-cell energy cutoff). The parameters for the ELPT card are: n, x_1, $x_2 \ldots x_i \ldots x_I$, where n = N for neutrons, P for photons, and E for

electrons, x_I = lower energy cutoff of cell i, and I is the number of cells in the problem (i.e., in the input deck in Appendix A, the cut off energy in the first cell is 0.0478 MeV, and 0.001 MeV for all other regions).

3.4.8 Esteps and Substeps

According to the MCNP4B manual, an electron step is the electron path length in a specific material corresponding to an average loss of 8.3% of the electron energy (this path length is energy and material dependent). In MCNP4B a condensed random walk is used, structured in terms of these electron steps. All precalculated and tabulated data for these electron steps are stored on an energy grid whose consecutive energy values obey the equation:

$$E_{n-1} - E_n = -\int_{s_{n-1}}^{s_n} \frac{dE}{ds}\, ds \qquad 3.1$$

where – dE/ds is the total stopping power in energy per unit length (energy and material dependent), s is the path length, and E_n is the electron energy at the n^{th} point in the grid.

In MCNP4B each electron step is further divided into smaller substeps in order to sample, more accurately, the angular deflections and the production of secondary particles. As a rule of thumb, MCNP4B requires that an electron should make at least ten substeps in any region of interest in the material through which the electrons are being transported. This is accomplished by using the continuous

slowing down range from Table 85 in the MCNP output and the following expression:

$$m = \frac{10R}{\rho L}, \qquad 3.2$$

where m is the number of substeps, R is the continuous slowing down approximation range in g cm^{-2}, ρ is the material density g cm^{-3}, and L is the thickness of the region in cm.

3.4.9 NPS History Cut Off Card

The parameter for this card is N, where N is the number of particle histories. This single entry is used to terminate the Monte Carlo calculation after N histories have been transported.

3.5 Sabrina Software

Sabrina is a graphics code primarily for use with the Monte Carlo N-particle MCNP to visualize 3-dimensional geometries in which MCNP and other codes simulate the transport of radiation. Sabrina performs geometry error checking, displays the tracks of Monte Carlo simulated particles, and translates solid body geometry descriptions to MCNP surface geometry.

CHAPTER 4

Electron Absorbed Fraction Using MCNP4B

4.1 Introduction

The current ICRP human respiratory tract model (HRTM) of Publication 66 enables calculations of the dose to the various regions of the respiratory tract following inhalation intakes of radionuclides to be made. Often the extrathoracic (ET) airways (ET_1 and ET_2) are the most highly irradiated tissue of the body following inhalation intakes (Nelson *et al.* 1997).

The high dose calculated for the extrathoracic airways, in particular the anterior portion of the nose or ET_1 region, is a consequence of: (1) a high fractional deposition of inhaled particles in the region (the ET_1 region is the first site of deposition); (2) the slow removal of deposited material from the region (removal is by extrinsic means, such as nose blowing and wiping at a transfer rate coefficient of 1/ day); and (3) the low tissue mass associated with the region. In addition, the HRTM assumes that absorption in blood occurs in all regions, with the notable exception of ET_1. Accordingly, the combination of low tissue mass and high number

ET_1. Accordingly, the combination of low tissue mass and high number of decays in the region leads to high doses to ET_1, particularly for short lived radionuclides.

The magnitude of these potential doses can be illustrated by examining the dose to the ET_1 region for a worker's inhalation intake limited to an effective dose of 20 mSv. Using the HRTM, the highest calculated ET_1 dose, 593 Sv, occurs for the Type F radionuclide ^{212}Pb, ($T_{1/2}$ = 10.6 hr). For Type M and S aerosols the highest doses are due to inhalation of ^{254}Fm ($T_{1/2}$= 3.24 hr) and ^{226}Ac ($T_{1/2}$ = 29 hr). Table 4.1 lists, for each absorption type, the 20 radionuclides with the highest ET_1 doses. Note that the tabulations include both alpha and beta, emitters with no common feature other than being short-lived. The calculated doses are shown graphically in Figure 4.1 for radionuclides with half-lives less than 1000 days for the various absorption types. The data of Table 4.1 and Figure 4.1 were generated assuming that the control of the individual radionuclides within the work place is solely based on constraining the committed effective dose to 20 mSv. Dose coefficients for the ET_1 region and the effective dose for workers were obtained from the ICRP CD-ROM*.

* Derived from the ICRP CD-ROM entitled "The ICRP Database of Dose Coefficients: Workers and Members of the Public," ISBN 0 08 042 7510 distributed by Elsevier Science Ltd.

Table 4.1 Radionuclides (20) with the highest ET_1 dose when the effective dose is set to 20 mSv for an intake of 5 μm by workers.

Type F		Type M		Type S	
Nuclide	H_{ET1} (Sv)	Nuclide	H_{ET1} (Sv)	Nuclide	H_{ET1} (Sv)
^{212}Pb	593	^{254}Fm	109	^{226}Ac	84
^{211}At	407	^{252}Fm	107	^{227}Pa	70
^{226}Ac	381	^{211}At	100	^{243}Pu	69
^{230}U	380	^{255}Fm	100	^{226}Th	64
^{224}Ac	338	^{226}Ac	91	^{107}Cd	63
^{214}Pb	337	^{254m}Es	81	^{180m}Ta	61
^{134m}Cs	223	^{238}Cm	79	^{64}Cu	60
^{197m}Hg	222	^{213}Bi	78	^{176m}Lu	56
^{211}Pb	200	^{212}Bi	76	^{195}Ir	56
^{212}Bi	200	^{227}Pa	75	^{245}Pu	52
^{197m}Hg	190	^{246}Cf	74	^{69m}Zn	52
^{209}Pb	181	^{127}Te	72	^{109}Pd	52
^{127}Te	180	^{83}Br	71	^{67}Cu	51
^{121}Sn	180	^{107}Cd	70	^{195m}Ir	51
^{213}Bi	177	^{243}Pu	69	^{179}Lu	51
^{193m}Pt	168	^{226Th}	67	^{105}Rh	50
^{199}Au	168	^{180m}Ta	65	^{178}Yb	49
^{67}Cu	166	^{121}Sn	64	^{137m}Ce	47
^{107}Cd	166	^{245}Am	63	^{31}Si	47
^{83}Br	165	^{257}Md	62	^{69}Zn	46

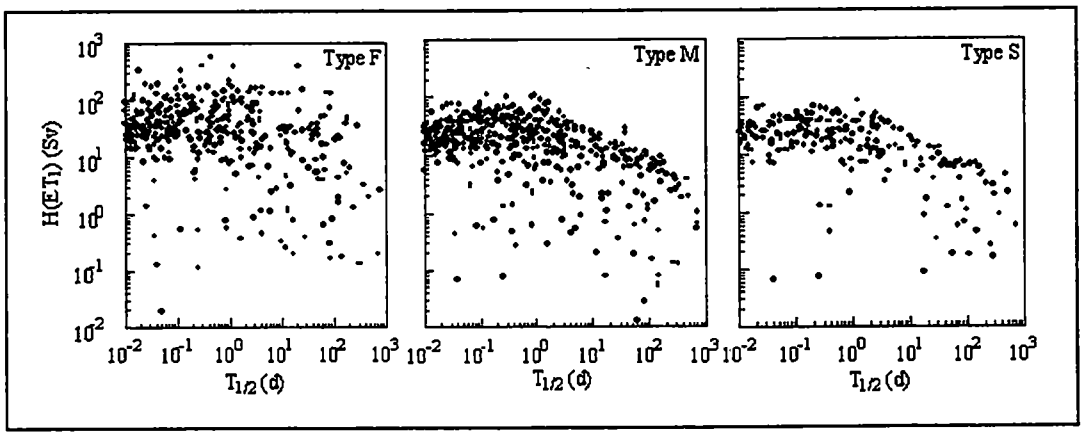


Figure 4.1 The equivalent dose (Sv) to ET_1 region as a result of inhalation intake by workers limited to an effective dose of 20 mSv of Type F, M, and S chemical forms.

In this chapter we use the MCNP4B code to obtain the electron absorbed fraction in ET_1 region of the nose using the same model used in ICRP Publication 66 (cylinder model). We do this for three reasons (1) to verify the electron absorbed fractions in ET_1 published in ICRP Publication 66; (2) to ensure that MCNP4B code is reliable for this type of estimation; and (3) to study the effect of changing the cylinder size (surface area and radius), the cylinder thickness beyond the target tissue, and the material composition on the electron absorbed fraction. The following cases are discussed in more detail to satisfy the third reason.

1. In cases 1 and 2 we change the source location on the cylinder inner surface (upper and lower half of the cylinder inner surface) to determine if change in the source location will affect the values of the electron absorbed fraction.

2. In case 3 and 4 we change (increased and decreased) the inner cylinder surface area to study how the electron absorbed fraction values are affected with the above changes.

3. In case 5 we increase the radius of the cylinder model to study its effect on the electron absorbed fraction.

4. In case 6 we increase the thickness of the cylinder beyond the target tissue to study its effect on the electron absorbed fraction.

5. In case 7 we replace the material composition in the cylinder model (previously air and water) with air and male soft tissue to study the material effect on the electron absorbed fraction.

6. In case 8 we investigate the effect of gender and age on the electron absorbed fraction.

4.2 Morphometric and Dosimetric Model

The HRTM divides the respiratory tract into four anatomical regions, as illustrated in Figure 2.4: (1) the extrathoracic region (ET), comprising the anterior nose (ET_1) and the posterior nasal passages (ET_2), which include the posterior nasal passage, larynx, pharynx, and the mouth; (2) the bronchial region (BB), consisting of the trachea and bronchi from which deposited materials are cleared by ciliary action; (3) the bronchiolar region (bb), consisting of the bronchioles and terminal bronchioles; and (4) the alveolar-interstitial region (AI), consisting of the ducts and alveoli. All regions contain lymphatic tissue (LN), although no lymphatic tissue is associated with ET_1. ICRP Publication 66 uses a simplified geometrical model in calculations of the fraction of the energy emitted within the airway that is absorbed in

the layer of tissue containing the basal cells. The electron absorbed fraction, *AF*, is the fraction of energy emitted by specified radiation *R* in a specified source region *S* that is absorbed in a specified target tissue *T*. The geometry assumed in these calculations is illustrated in Figure 2.6. As indicated in ICRP publication 66 (ICRP 1994, p. 84), the electron absorbed fractions are derived assuming that a monoenergetic electron emitter is uniformly deposited on the inner surface of the nasal vestibule. A cylindrical tube of appropriate dimensions (internal diameter of 5 mm and inner surface area of 20 cm^2) is used to model the nasal vestibules. The Electron Gamma Shower (EGS4) transport code (Nelson *et al.* 1985), which simulates the production of both knock-on electrons and bremsstrahlung above a certain energy threshold (taken to be 1 keV for these calculations), was used to calculate the electron absorbed fractions for mono-energetic electrons tabulated in Publication 66. The materials used in that analysis were air and water to simulate tissue.

4.3 MCNP4B Input Model

The calculated equivalent doses shown in Table 4.1 are sufficiently high and would severely damage the irradiated tissues. Since such damage has not been reported, it seems reasonable to consider that the computational procedures need further scrutiny. Therefore, noting that no other calculations of the electron absorbed fraction have been reported in the literature, we calculate the electron absorbed

fractions using the Monte Carlo N-Particle Transport Code System (MCNP4B) and compare the results with the ones existing in ICRP Publication 66, which are obtained using the EGS4 code. There are several parameters (i.e., number of histories, what physics parameters are used, and how many Esteps should be chosen in each region the particle traverses) in the MCNP4B input file that will affect, to various degrees, the results in the MCNP4B output. Therefore, during the process of creating the input deck, we evaluate these important parameters through a computer experiment using the results, which give us the best standard deviation, and our knowledge of the particle physics. Also some equations given in the MCNP4B manual related to the continuous slowing down approximation range and stopping power are used.

4.3.1 Number of Histories Experiment

An input file is created for use in the MCNP4B code in which the nasal vestibule is modeled by four concentric open cylinders (Figure 4.2). The inner region has a radius of 0.25 cm and is filled with air. The subsequent regions bounded by inner and outer cylinders represent tissue. The basal cell layer is the region between cylinders of radii 0.254 and 0.255 cm. The height of each cylinder is 12.732 cm, which corresponds to the inner cylinder having a surface area of 20 cm^2. In this experiment monoenergetic electrons with energies of 0.5 MeV are used to estimate the energy deposition. The source is expressed as a uniform surface source located on the inner surface of the first cylinder (see Figure4.2).

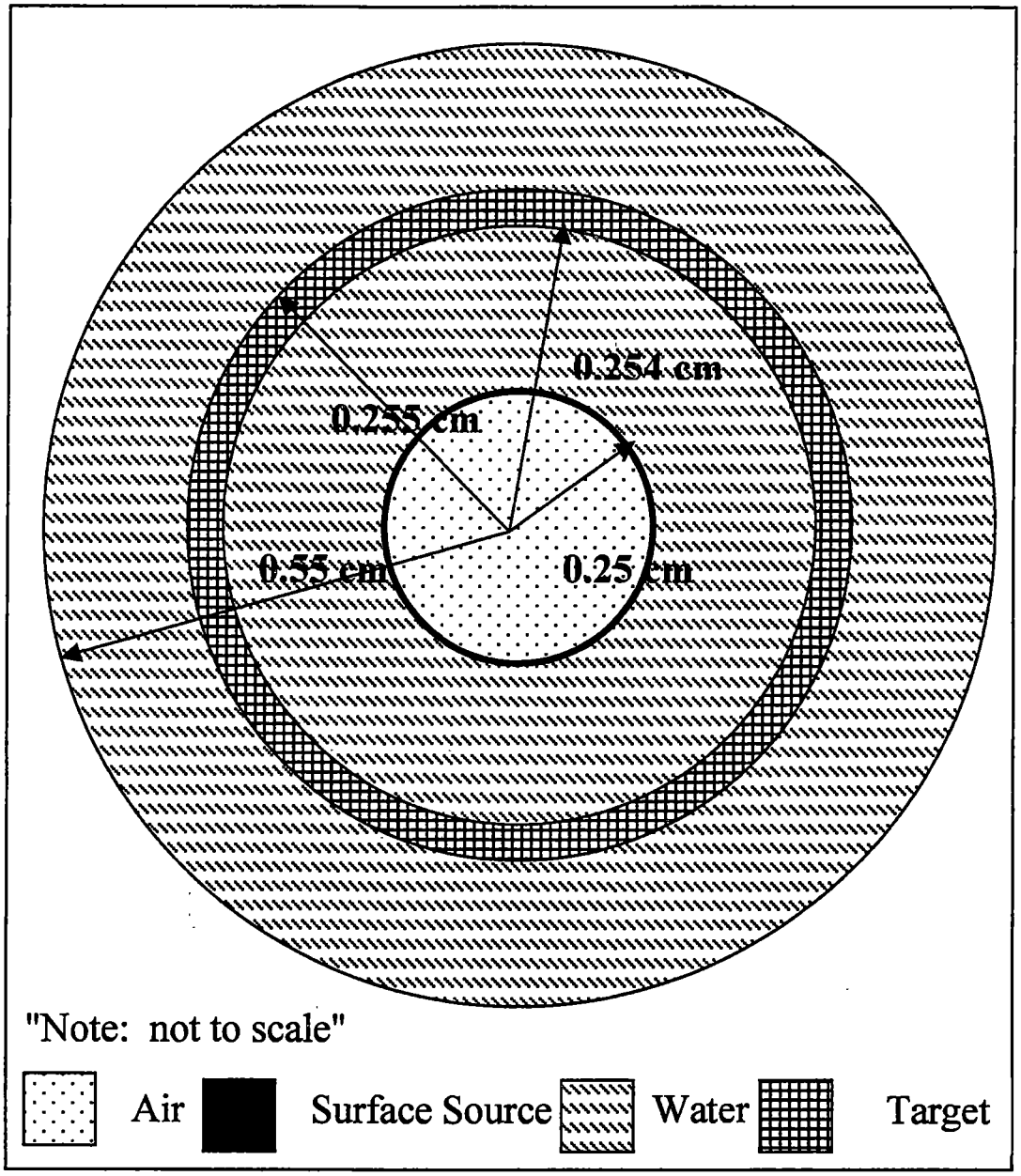


Figure 4.2 The geometric model used to derive the electron absorbed fraction data for electrons in ET_1.

The energy deposited in the specified regions are scored using MCNP's *f8 tally (the energy deposited in a specific cell as the result of electron transported in it). Each electron is transported until its kinetic energy is less than 0.0478 MeV within the inner cylinder or less than 0.001 MeV for all other regions.

Four separate runs of 1000, 10000, 50000 and 100,0000 histories are used to determine the suitable number of particle histories (NPS) to be used. Table 4.2 tabulates the output for each run. Since the lowest relative error and consequently the lowest standard deviation were obtained in the O_4 output file, 100,000 histories were selected for future MCNP4B runs.

4.3.2 E step and Substeps Experiment

According to the MCNP4B manual, an electron step is the electron path length in a specific material corresponding to an average loss of 8.3% of the electron energy (this path length is energy and material dependent). In MCNP4B a condensed

Table 4.2. The energy deposition in region 3 (basal cells region) and the estimated relative error, the standard deviation, and the computer running time.

Output name	Number of Histories	Energy Deposited(MeV)	Relative Error	Standard Deviation	Running Time(m)
O_1	1000	7.2698E-3	0.053	3.853E-4	0.61
O_2	10000	7.5916E-3	0.013	9.869E-5	5.45
O_3	50000	7.5508E-3	0.008	6.041E-5	26.88
O_4	100000	7.5230E-3	0.006	4.363E-5	53.64

random walk is used, structured in terms of these electron steps. All precalculated and tabulated data for these electron steps (e.g., stopping power, range, and radiation yield) are stored on an energy grid whose consecutive energy values obey the following equation:

$$E_{n-1} - E_n = -\int_{s_{n-1}}^{s_n} \frac{dE}{ds} ds \qquad 4.1$$

where (– dE/ds) is the total stopping power in energy per unit length (energy and material dependent), s is the path length, and E_n is the electron energy at the n^{th} point in the grid.

In MCNP4B each electron step is further divided into smaller substeps in order to sample, more accurately, the angular deflections and the production of secondary particles. As a rule of thumb, MCNP4B requires that an electron should make at least ten substeps in any region of interest in the material through which the electrons are being transported. This is accomplished by using the continuous slowing down range from Table 85 in the MCNP output and the following expression:

$$m_i = \frac{10R_i}{\rho_i L_i}, \qquad 4.2$$

where m_i is the number of substeps in material (region) i, ρ_i is the material density g/cm^3 in region i, L_i is the thickness of region i in cm, and R_i is the continuous slowing down approximation range in g/cm^2 in material (region) i, obtained by interpolation from Table 85 in the MCNP output corresponding to the electron's

energy when it enters material (region) i. It can be calculated using the following equation:

$$E_i = E - \sum_{\substack{n=1 \\ i \neq 1}}^{n=i-1} E_n \qquad 4.3$$

where E is the electron initial energy, E_n is the energy deposited in region(s) n (region(s) before region i). Initial MCNP calculations are performed for monoenergetic electrons of energies ranging from 0.0485 MeV to 4 MeV using the energy values specified in Table H.2. of ICRP Publication 66. In this initial calculation no Estep are introduced in the input. At each energy, the calculations involve tracking 100,000 electrons emitted uniformly from the surface of the inner cylinder. From Table 85 in the output we obtain the value of the continuous slowing down approximation range corresponding to the initial electron energy, then we use equation (4.2) to obtain the number of Estep in region (1).

A second MCNP calculation is performed for monoenergetic electrons with energies ranging from 0.0485 MeV to 4 MeV using the energy values specified in Table H.2. of ICRP Publication 66. In this calculation the calculated Estep is assigned to region 1 (on the material card), then at each energy, the calculations involve tracking 100,000 electrons emitted uniformly from the surface of the inner cylinder. From Table 85 in the output we obtain the value of the continuous slowing down approximation range corresponding to the initial electron energy. Then we use equation (4.2) to obtain the number of Estep in region (2). Also using the energy deposited in region (1) (from the MCNP output), we calculate the electron energy

before it enters region (2) using equation (4.3). The continuous slowing down approximation range corresponding to the calculated electron energy is obtained and used to calculate the Estep in region (2). The calculations proceed to regions 3 and 4 respectively. Table 4.3 summarizes the results of these calculations and shows the Estep for each region corresponding to each particular energy.

4.3.3 Physics Parameters Experiment

Monoenergetic electrons with energies of 0.0485 MeV, 0.07 MeV, 0.1 MeV, 0.15 MeV, 0.3 MeV, 0.8 MeV, 1.0 MeV, 1.5 MeV, and 4.0 MeV are used as inputs into MCNP4B to estimate the energy deposition with different physics parameters. A continuous running batch consisting of 45 input files (five files for each energy mentioned above) is created. The Estep obtained from the Estep experiment is included in these files. The physics parameters presented in the input files are:

Phys:e E 0 0 0 0 1 1 1 1

Phys:e E 0 0 0 1 1 1 1 0

Phys:e E 0 0 0 1 1 1 1 1

Phys:e E 0 0 0 0 1 1 1 1

Phys:e E 1 1 1 0 1 1 1 1

Table 4.3 The calculated Esteps in regions C_1, C_2, C_3 and C_4 corresponding to monoenergetic electrons of energy ranging from 0.0485 MeV to 4 MeV using the energy values specified in Table H.2. of ICRP Publication 66.

Energy (MeV)	Estep				Energy (MeV)	Estep			
	C_1	C_2	C_3	C_4		C_1	C_2	C_3	C_4
0.0485	21	1	1	1	0.2000	206	17	45	1
0.0500	22	1	1	1	0.2150	229	18	52	1
0.0550	26	2	1	1	0.2180	233	19	54	1
0.0600	30	2	1	1	0.3000	366	30	98	1
0.0650	34	3	1	1	0.4000	536	44	155	1
0.0700	39	3	1	1	0.5000	709	58	212	1
0.0750	44	3	1	1	0.6000	881	72	269	1
0.0800	48	4	1	1	0.7000	1050	86	326	1
0.0850	54	4	2	1	0.8000	1218	100	383	1
0.0900	59	5	3	1	0.9000	1381	114	438	1
0.0950	64	5	4	1	1.0000	1543	127	493	1
0.1000	70	6	5	1	1.5000	2311	193	756	1
0.1125	84	7	9	1	2.0000	3030	255	1005	4
0.1250	100	8	13	1	3.0000	4369	371	1473	5
0.1500	133	11	22	1	4.0000	5615	482	1916	6
0.1750	168	14	33	1					

where e stand for electron transport, E is the electron energy, and the next eight entries are for IDES, IPHOT, IBAD, ISTRG, BNUM, XNUM, RNOK, and ENUM (see chapter 3 for more details on those parameters). The results are tabulated in Table 4.4.

Since the energy deposition and consequently the electron absorbed fractions corresponding to each energy are almost the same using various physics parameters (except for low energy), we will use the switch ISTRG =1 (fourth entry after the energy in physics card), even though for low energy (0.0485 MeV) the effect of ISTRG =0 versus ISTRG=1 on the electron absorbed fraction is obvious

Table 4.4 Energy deposition and computer running time for 0.0485, 0.07, 0.1, 0.15, 0.3, 0.8, 1.0 1.5, and 4.0 MeV electrons corresponding to the various physics parameters.

Energy (MeV)	Phys	Estep				Energy Deposition	Computer Run Time (min)
		C1	C2	C3	C4		
0.0485	0 0 0 0 1 1 1 1	21	1	1	1	1.949E-04	3.7800
0.0485	0 0 0 1 1 1 1 0	21	1	1	1	4.563E-05	2.5200
0.0485	0 0 0 1 1 1 1 1	21	1	1	1	4.563E-05	2.4400
0.0485	0 0 0 0 1 1 1 0	21	1	1	1	1.949E-04	3.7700
0.0485	1 1 1 0 1 1 1 1	21	1	1	1	1.949E-04	3.7700
0.0700	0 0 0 0 1 1 1 1	39	3	1	1	5.492E-03	10.080
0.0700	0 0 0 1 1 1 1 0	39	3	1	1	5.168E-03	6.4100
0.0700	0 0 0 1 1 1 1 1	39	3	1	1	5.168E-03	6.4100
0.0700	0 0 0 0 1 1 1 0	39	3	1	1	5.492E-03	10.100
0.0700	1 1 1 0 1 1 1 1	39	3	1	1	5.492E-03	10.130
0.1000	0 0 0 0 1 1 1 1	70	6	5	1	8.938E-03	20.060
0.1000	0 0 0 1 1 1 1 0	70	6	5	1	9.128E-03	13.140
0.1000	0 0 0 1 1 1 1 1	70	6	5	1	9.128E-03	13.140
0.1000	0 0 0 0 1 1 1 0	70	6	5	1	8.938E-03	20.040
0.1000	1 1 1 0 1 1 1 1	70	6	5	1	8.938E-03	20.060
0.1500	0 0 0 0 1 1 1 1	133	11	22	1	9.066E-03	35.990
0.1500	0 0 0 1 1 1 1 0	133	11	22	1	9.448E-03	24.700
0.1500	0 0 0 1 1 1 1 1	133	11	22	1	9.448E-03	24.710
0.1500	0 0 0 0 1 1 1 0	133	11	22	1	9.066E-03	35.990
0.1500	1 1 1 0 1 1 1 1	133	11	22	1	9.066E-03	35.930
0.3000	0 0 0 0 1 1 1 1	366	30	98	1	7.525E-03	77.900
0.3000	0 0 0 1 1 1 1 0	366	30	98	1	7.728E-03	53.840
0.3000	0 0 0 1 1 1 1 1	366	30	98	1	7.728E-03	53.840
0.3000	0 0 0 0 1 1 1 0	366	30	98	1	7.525E-03	77.430
0.3000	1 1 1 0 1 1 1 1	366	30	98	1	7.525E-03	77.240
0.8000	0 0 0 0 1 1 1 1	1218	100	383	1	6.037E-03	190.30
0.8000	0 0 0 1 1 1 1 0	1218	100	383	1	6.147E-03	133.54
0.8000	0 0 0 1 1 1 1 1	1218	100	383	1	6.147E-03	133.75
0.8000	0 0 0 0 1 1 1 0	1218	100	383	1	6.037E-03	190.17
0.8000	1 1 1 0 1 1 1 1	1218	100	383	1	6.037E-03	190.15
1.0000	0 0 0 0 1 1 1 1	1543	127	493	1	5.818E-03	228.38
1.0000	0 0 0 1 1 1 1 0	1543	127	493	1	5.793E-03	153.95
1.0000	0 0 0 1 1 1 1 1	1543	127	493	1	5.793E-03	156.61
1.0000	0 0 0 0 1 1 1 0	1543	127	493	1	5.818E-03	228.46
1.0000	1 1 1 0 1 1 1 1	1543	127	493	1	5.818E-03	229.08
1.5000	0 0 0 0 1 1 1 1	2311	193	756	1	5.401E-03	268.42

Table 4.4 (continued)

Energy (MeV)	Phys	Estep				Energy Deposition	Computer Run Time (min)
		C1	C2	C3	C 4		
1.5000	0 0 0 1 1 1 1 0	2311	193	756	1	5.391E-03	198.41
1.5000	0 0 0 1 1 1 1 1	2311	193	756	1	5.391E-03	198.41
1.5000	0 0 0 0 1 1 1 0	2311	193	756	1	5.401E-03	268.41
1.5000	1 1 1 0 1 1 1 1	2311	193	756	1	5.401E-03	268.53
4.0000	0 0 0 0 1 1 1 1	5615	482	1916	6	5.209E-03	523.45
4.0000	0 0 0 1 1 1 1 0	5615	482	1916	6	5.192E-03	376.40
4.0000	0 0 0 1 1 1 1 1	5615	482	1916	6	5.192E-03	376.38
4.0000	0 0 0 0 1 1 1 0	5615	482	1916	6	5.209E-03	523.42
4.0000	1 1 1 0 1 1 1 1	5615	482	1916	6	5.209E-03	523.92

(1.949×10^{-4} versus 4.56257×10^{-5}, a factor of four). The reasons behind using ISTRG =1 are:

- Using ISTRG =1, the expected value for each collision is used instead of the realistic sampling value, this option of using the expected value is useful for some comparisons to deterministic electron transport calculations (MCNP4B manual, page 3-106).

- The computer running time is longer if ISTRG =0 (the computer time is also shown in Table 4.4.

A copy of the MCNP4B input deck, which is identical to the input used in ICRP Publication 66 with EGS4, can be found in Appendix A. In this input deck we

use the results obtained from the history experiment (100,000 histories), and the results from the physics parameter experiment (0 0 0 1 1 1 1 1). 31 input decks are created from the original one to account for 31 different energies and consequently to introduce different Esteps using the results in Table 4.3. The MCNP4B output results for the 31 input files (the energy deposition in cell number 3 and its relative error) are divided by the initial electron energy to obtain the electron absorbed fraction (*AF*) and its standard deviation.

4.4 Electron Absorbed Fraction Using MCNP4B vs. EGS4 (Code Differences)

Although both MCNP4B and EGS4 solve problems based on the Monte Carlo method, there are some numerical differences in their outputs, as illustrated in Figure 4.3 and Table 4.5. The differences for electrons with energies less than 80 keV increase as the energy decreases. In the EGS4 manual (Nelson *et al.* 1985), it is noted that further research is needed to properly account for the changes in cross section as a function of energy for low energy electrons (energy less that 80 keV). This may be the source of the increasing differences for electron energies less than 80 keV. When the electron initial energies exceed 80 keV, some numerical differences in the two sets of electron absorbed fractions are evident, typically about 20% (the largest deviation corresponding to an energy of 1 MeV).

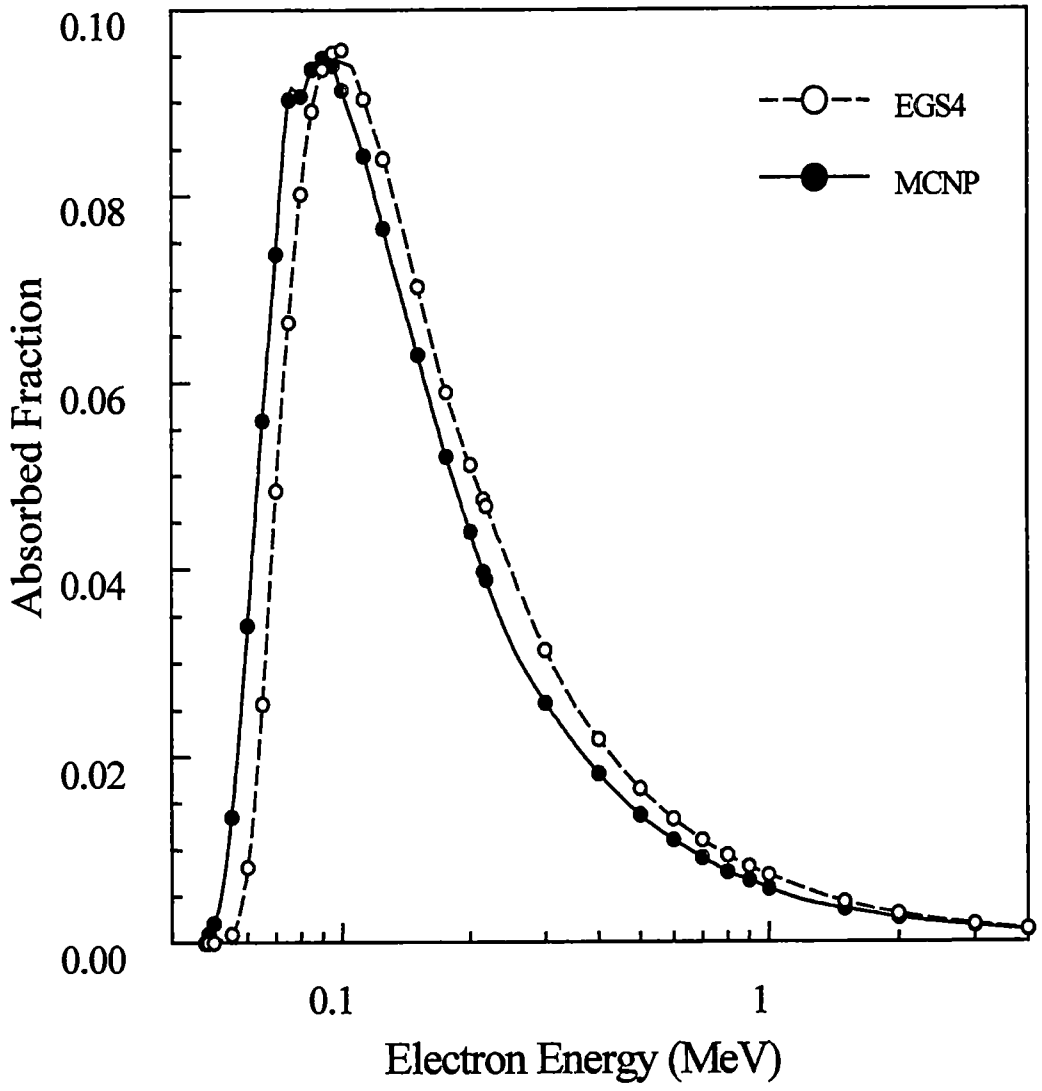


Figure 4.3 Electron absorbed fraction (AF) results from MCNP4B and EGS4 codes for a cylinder model vs. energy (MeV).

Table 4.5 Electron absorbed fraction results using MCNP4B and EGS4 (ICRP 66) for a cylinder model, the standard deviation (for MCNP4B data), and the percentage difference.

Electron Energy (MeV)	A.F (MCNP4B)	S.D (MCNP4)[a]	A.F (ICRP 66)[b]	%Difference[c]
0.0478[d]	0	0	0	0
0.0485	9.41E-04	4.86E-05	1.99E-06	47177.62
0.0500	2.09E-03	7.66E-05	4.05E-06	51603.70
0.0550	1.35E-02	2.07E-04	8.65E-04	1463.85
0.0600	3.40E-02	3.30E-04	8.13E-03	317.88
0.0650	5.59E-02	4.08E-04	2.57E-02	117.47
0.0700	7.38E-02	4.50E-04	4.84E-02	52.53
0.0750	9.03E-02	4.69E-04	6.65E-02	35.75
0.0800	9.07E-02	4.54E-04	8.02E-02	13.10
0.0850	9.36E-02	4.40E-04	8.91E-02	5.10
0.0900	9.48E-02	4.27E-04	9.36E-02	1.27
0.0950	9.40E-02	4.04E-04	9.54E-02	1.44
0.1000	9.13E-02	3.74E-04	9.57E-02	4.62
0.1125	8.43E-02	3.37E-04	9.04E-02	6.78
0.1250	7.65E-02	2.98E-04	8.40E-02	8.97
0.1500	6.30E-02	2.46E-04	7.03E-02	10.40
0.1750	5.21E-02	2.08E-04	5.90E-02	11.73
0.2000	4.40E-02	1.85E-04	5.12E-02	14.13
0.2150	3.97E-02	1.71E-04	4.75E-02	16.47
0.2180	3.89E-02	1.67E-04	4.68E-02	16.95
0.3000	2.58E-02	1.24E-04	3.14E-02	17.96
0.4000	1.82E-02	9.26E-05	2.19E-02	17.05
0.5000	1.37E-02	7.39E-05	1.66E-02	17.51
0.6000	1.10E-02	6.48E-05	1.33E-02	17.36
0.7000	9.10E-03	5.64E-05	1.10E-02	17.28
0.8000	7.55E-03	5.13E-05	9.34E-03	19.21
0.9000	6.66E-03	4.66E-05	8.15E-03	18.30
1.0000	5.79E-03	4.29E-05	7.25E-03	20.10
1.5000	3.59E-03	3.63E-05	4.36E-03	17.57
2.0000	2.65E-03	2.94E-05	3.07E-03	13.82
3.0000	1.75E-03	2.95E-05	1.93E-03	9.51
4.0000	1.30E-03	2.14E-05	1.41E-03	7.94

[a] The standard deviation calculated by using the relative error and the energy deposited from MCNP4B output (the estimated relative error x the energy deposited)/(electron initial energy).

[b] Electron absorbed fraction obtained using the Electron Gamma Shower (EGS4) Code.

[c] % difference = Absolute value of 100%x(*AF*(ICRP 66) – *AF*(MCNP4B))/*AF*(ICRP 66).

[d] The continuous slowing down approximation range (CSDA) is less than the depth of of the target.

4.5 Source Located in the Upper Half Cylinder (Case Study 1)

In this case study, the same input decks (31) used in section 4.4 are used again except that the source expression in the source card is modified so that the source is considered to be a surface source distributed uniformly only on the inner surface of the upper half (the source height is 6.366 cm). The outputs of these MCNP4B runs are summarized in Table 4.6 in Appendix B.

4.5.1 Discussion

A plot of the electron absorbed fractions versus the electron initial energy is presented in Figure 4.4. Plotted are the electron absorbed fraction data taken from Table 4.5 and the electron absorbed fraction data taken from Table 4.6 in Appendix B. The two plots lay on top of each other. The percentage differences between the electron absorbed fraction obtained from Table 4.5 and Table 4.6 are tabulated in Table 4.7 in Appendix B. The maximum percentage difference is 2.03%, which occurs at an energy of 0.08 MeV. Therefore, we consider that the electron absorbed fraction is the same in both cases.

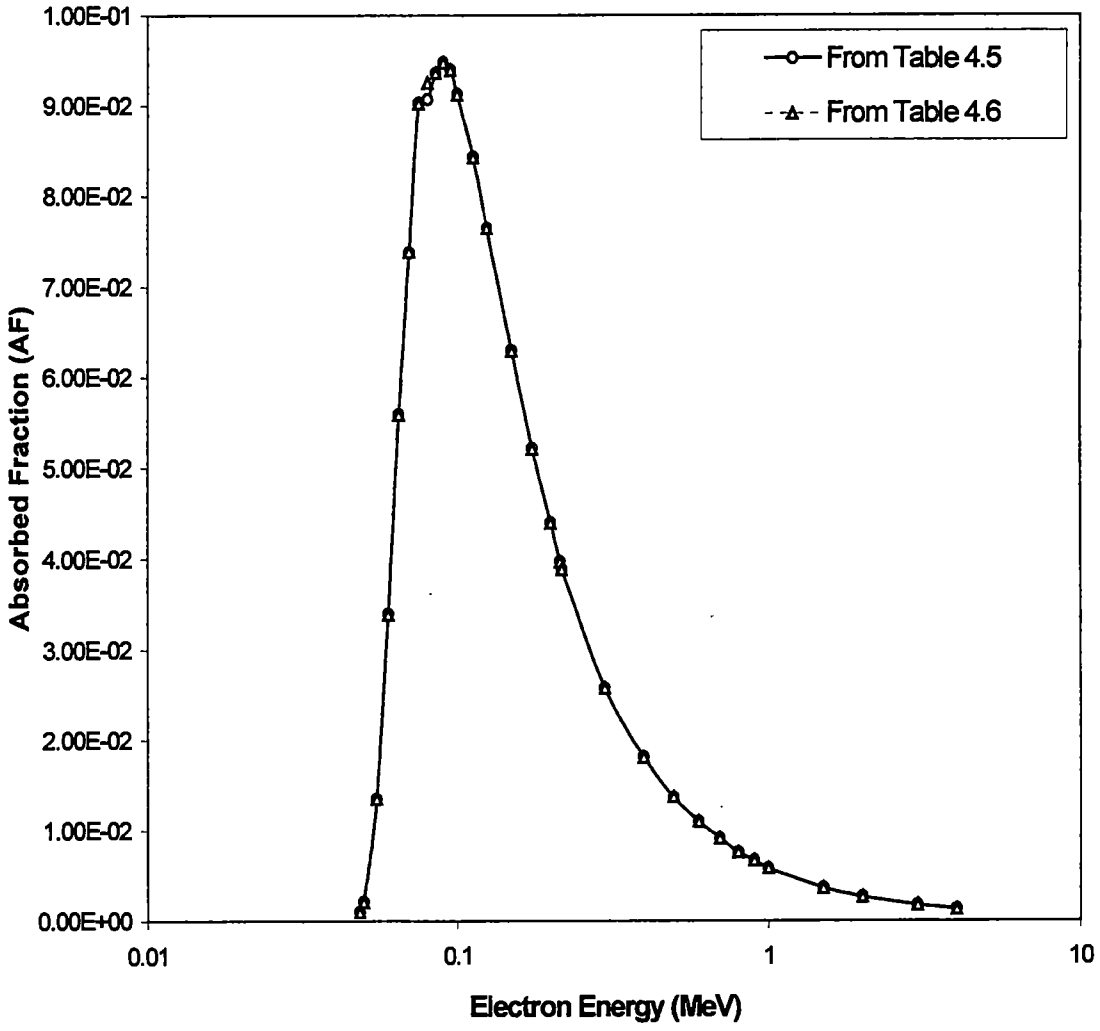


Figure 4.4 Electron absorbed fraction vs. electron energy (MeV) taken from Table 4.5 (cylinder with the source equally distributed on its inner surface area (20 cm^2) and from Table 4.6 (cylinder with the source equally distributed on its upper half inner surface).

4.6 Source Located in the Lower Half Cylinder (Case Study 2)

In this case study, the same input decks (31) used in section 4.4 are used again except that the source expression in the source card is modified so that the source is considered to be a surface source distributed uniformly only on the inner surface of the lower half (the source height is 6.366 cm). The outputs of these MCNP4B runs are summarized in Table 4.8 in Appendix B and in Figure 4.5.

4.6.1 Discussion

A plot of the electron absorbed fractions versus the electron initial energy is presented in Figure 4.5. Plotted are the electron absorbed fraction data taken from Table 4.5 and the electron absorbed fraction data taken from Table 4.8 in Appendix B. The two plots lay on top of each other. The percentage differences between the electron absorbed fraction obtained from Table 4.5 and Table 4.8 are tabulated in Table 4.9 in Appendix B. The maximum percentage difference is 2.05%, which occurs at an energy of 0.08 MeV. Therefore, we consider that the electron absorbed fraction is the same for both cases. Overall, for a cylinder model, the source location does not appear to matter.

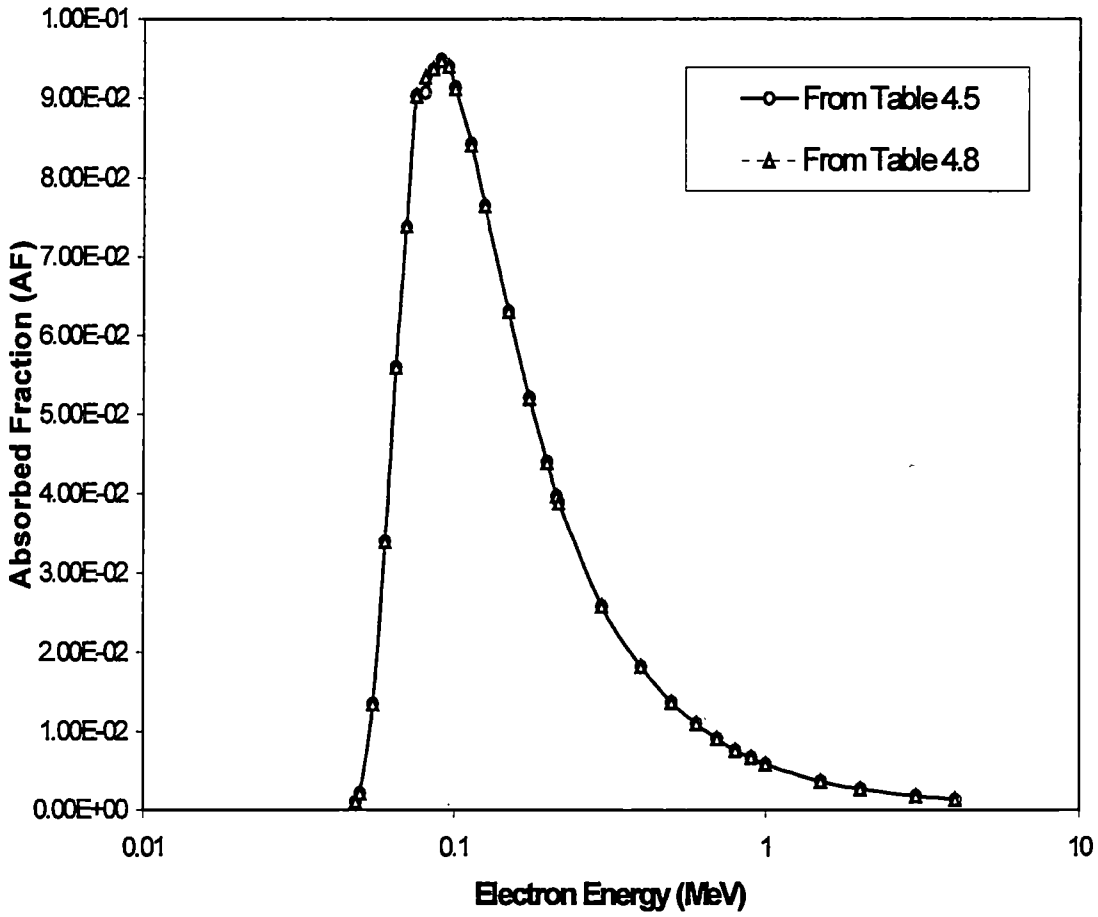


Figure 4.5 Electron absorbed fraction vs. energy (MeV) taken from Table 4.5 (cylinder with the source equally distributed on its inner surface area (20 cm^2) and from Table 4.8 (cylinder with the source equally distributed on its lower half inner surface).

4.7 The Effect of Surface Area on the Electron Absorbed Fraction.

To study changes in the electron absorbed fraction values due to the changes in the surface area of the cylindrical model, we change the original inner surface area (20 cm^2) by 10%, 25%, 50%, and 75%.

4.7.1 10%, 25%, 50%, and 75% Increases in the Surface Area (Case 3)

The input deck is used to create four new batches, each batch consisting of 31 input files where, in each file, the cell and surface cards are modified so that the height of the new cylinders corresponds to an inner surface area of 22 cm^2, 25cm^2, 30 cm^2 and 35 cm^2 given that the radius of the cylinders stays at 0.25 cm. (i.e., the cylinder heights are 14.006 cm, 15.915 cm, 19.098 cm, and 22.282 cm). Ultimately, since the source is distributed on the inner surface of each cylinder, the source height is the same as the cylinder height. The materials used are air and water. The outputs of the MCNP4B runs are summarized in Tables 4.10-4.13 in Appendix B.

4.7.2 Discussion

A plot of the electron absorbed fractions versus the electron initial energy is presented in Figure 4.6. Plotted are the electron absorbed fraction data taken from Table 4.5 and the electron absorbed fraction data taken from Tables 4.10-4.13 in

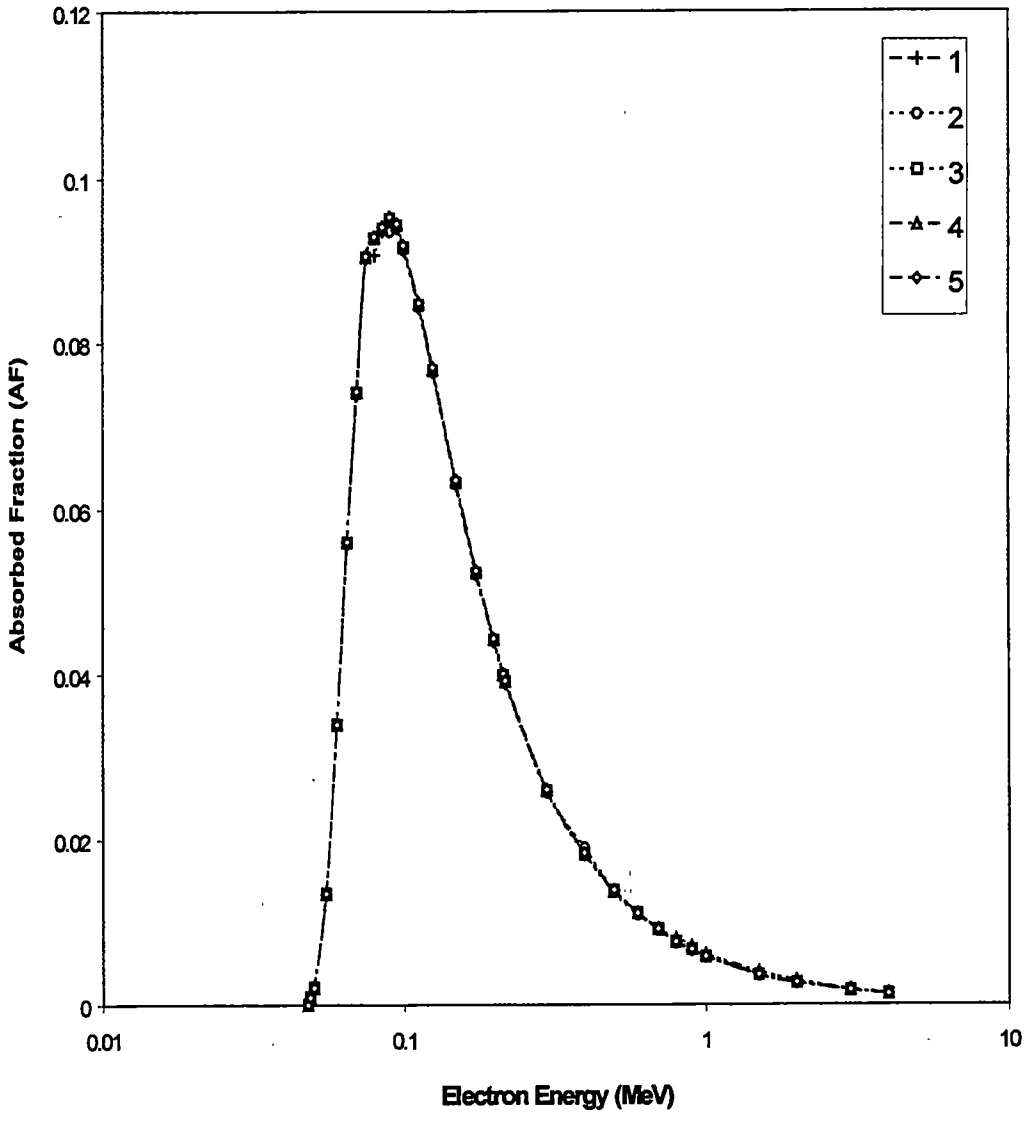


Figure 4.6 Electron absorbed fraction vs. energy (MeV) for cylinders with inner surface areas of (1) 20 cm^2, (2) 22 cm^2, (3) 25 cm^2, (4) 30 cm^2, and (5) 35 cm^2.

Appendix B. The five plots lay on top of each other. The percentage differences between the electron absorbed fraction obtained from Table 4.5 and Tables 4.10-4.13 are tabulated in Tables 4.14-4.17 in Appendix B, the maximum percentage differences are 2.21%, 2.32%, 2.43% and 2.54%. These maxima occur at 0.08 MeV. Since the maximum differences are relatively small, these results indicate that the electron absorbed fraction is nearly the same for all cases, and increases in the surface area do not effect the values of the electron absorbed fractions.

4.7.3 10%, 25%, 50%, and 75% Decreases in the Surface Area (Case 4)

The input deck is used to create four new batches, each batch consisting of 31 input files where, in each file, the cell and surface cards are modified so that the height of the new cylinders corresponds to an inner surface area of 18 cm^2, 15cm^2, 10 cm^2 and 5 cm^2 given that the radius of the cylinders stays at 0.25 cm. (i.e., the cylinder heights are 11.459 cm, 9.549 cm, 6.366 cm, and 3.183 cm). Ultimately, since the source is distributed on the inner surface of each cylinder, the source height is the same as the cylinder height. The materials used are air and water. The outputs of the MCNP4B runs are summarized in Tables 4.18-4.21 in Appendix B.

4.7.4 Discussion

A plot of the electron absorbed fractions versus the electron initial energy is presented in Figure 4.7. Plotted are the electron absorbed fraction data taken from Table 4.5 and the electron absorbed fraction data taken from Tables 4.18-4.21 in Appendix B. The percentage differences between the electron absorbed fractions obtained from Table 4.5 and Tables 4.18-4.21 are tabulated in Tables 4.22-4.25 in Appendix B. The maximum percentage differences are 1.87%, 1.71%, 4%, and 10.3%. These maxima occur at 0.08 MeV in Table 4.22 and 3 MeV in all other tables. Since the maximum differences are relatively small in the first and second tables, those results indicate that the electron absorbed fraction is nearly the same and decreasing the inner surface area of the cylinder by 10-25% does not appreciably effect the values of the electron absorbed fraction. However, when the decrease in the inner surface area of the cylinder is greater than 25%, the maximum percentage differences start to increase. Therefore, we note that the electron absorbed fraction will be affected by these decreases, and ultimately a new electron absorbed fraction should be obtained for noses smaller than the nose model used to obtained the electron absorbed fraction tabulated in Table 4.5. (i.e., noses of children and Asians).

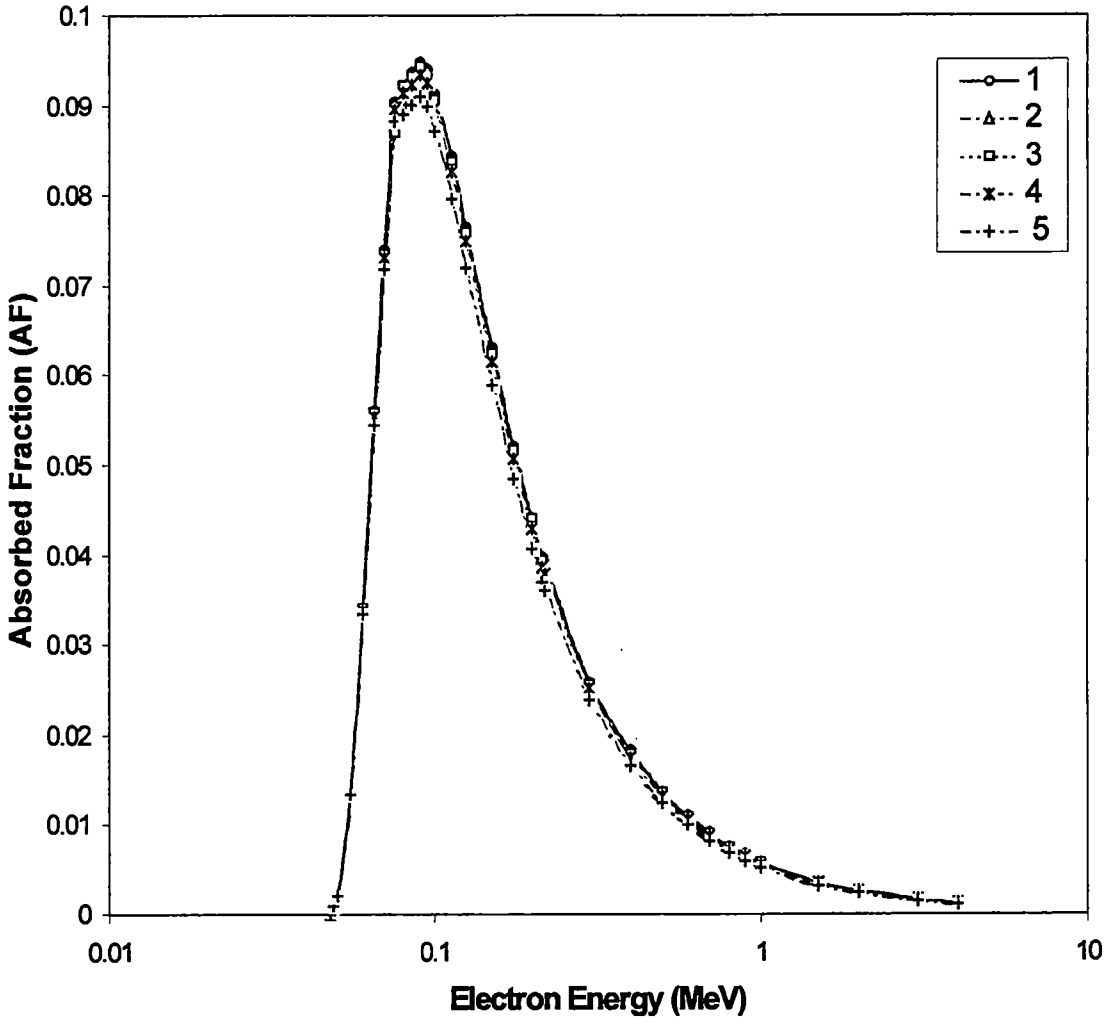


Figure 4.7 Electron absorbed fraction vs. energy (MeV) for cylinders with inner surface areas of (1) 20 cm^2, (2) 18 cm^2, (3) 15 cm^2, (4) 10 cm^2, and (5) 5 cm^2

4.8 Radius Changes and Electron Absorbed Fraction (Case 5)

To study the changes in the electron absorbed fraction values due to the changes in the radii of the cylindrical model, the original input deck is used to create three new batches. Each batch consisting of 31 input files where in each file, the cell and surface cards are modified, so that radius of the cylinder is changed to 0.3 cm, 0.35 cm and 0.76394 cm while fixing the inner surface area at 20 cm^2. Note that this results in different heights for the cylinder at each radius. The outputs of the MCNP4B runs are summarized in Tables 4.26-4.28 in Appendix B.

4.8.1 Discussion

A plot of the electron absorbed fractions versus the electron initial energy is presented in Figure 4.8. Plotted are the electron absorbed fraction data taken from Table 4.5 and the electron absorbed fraction data taken from Tables 4.26-4.28 in Appendix B. The percentage differences between the electron absorbed fraction obtained from 4.5 and Tables 4.26-4.28 are tabulated in Tables 4.29-4.31 in Appendix B. The maximum percentage differences are 6.67, 32.4, and 33.8. These maxima occur at 0.055 MeV, 4 MeV, and 0.06 MeV respectively. From the above differences, we conclude that the changes in the cylinder radius have a significant effect on the electron absorbed fraction. In reality, there are groups that have larger nostrils (equivalent diameter is about 1.6 cm to 2.5 cm; e.g., African nose).

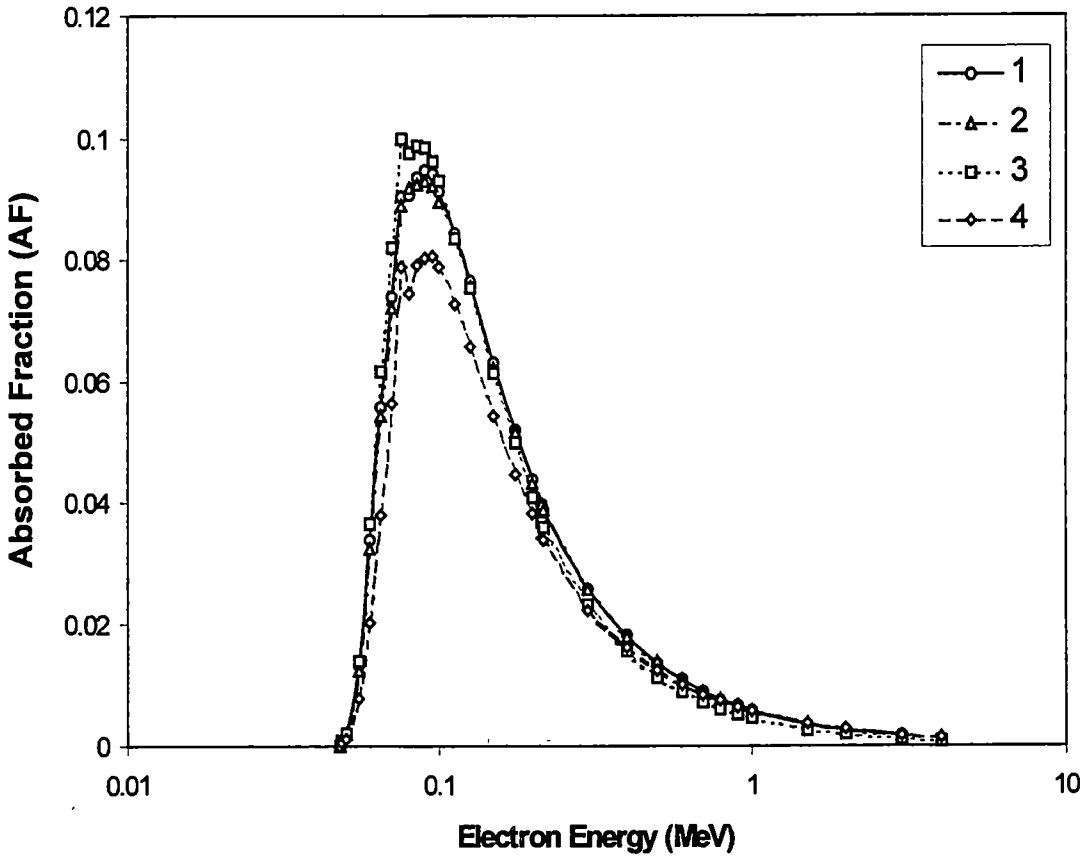


Figure 4.8 Electron absorbed fraction vs. Energy (MeV) for cylinders with radii of (1) 0.25 cm, (2) 0.3 cm, (3) 0.35 cm and (4) 0.76394 cm

Therefore, to calculate more accurately the dose to a person from this ethnic group, one should use the electron absorbed fractions estimated for radii that are different than the ones used for a Caucasian male (those published in ICRP 66, Table H.2).

4.9 The Effect of External Thickness on Electron Absorbed Fraction (Case 6).

To study the effect of the soft tissue thickness outside the target (basal cells), two input batches are created from the original input file. Each batch consists of 31 input files, where the surface area and the radius remain the same while the thickness beyond the target changes (originally it was 0.295 cm). The new values are 0.095 cm and 0.195 cm. The outputs of the MCNP4B runs are summarized in Tables 4.31-4.32 in Appendix B.

4.9.1 Discussion

A plot of the electron absorbed fractions versus the electron initial energy is presented in Figure 4.9. Plotted are the electron absorbed fraction data taken from Table 4.5 and the electron absorbed fraction data taken from Tables 4.31-4.32 in Appendix B. The percentage differences between the electron absorbed fraction obtained from Table 4.5 and Tables 4.31-4.32 are tabulated in Tables 4.33 and 4.34 in Appendix B. The maximum percentage differences are 4.53% and 1.71%. These maxima occur at 2 MeV and 3 MeV. From Tables 4.33 and 4.34 (for soft

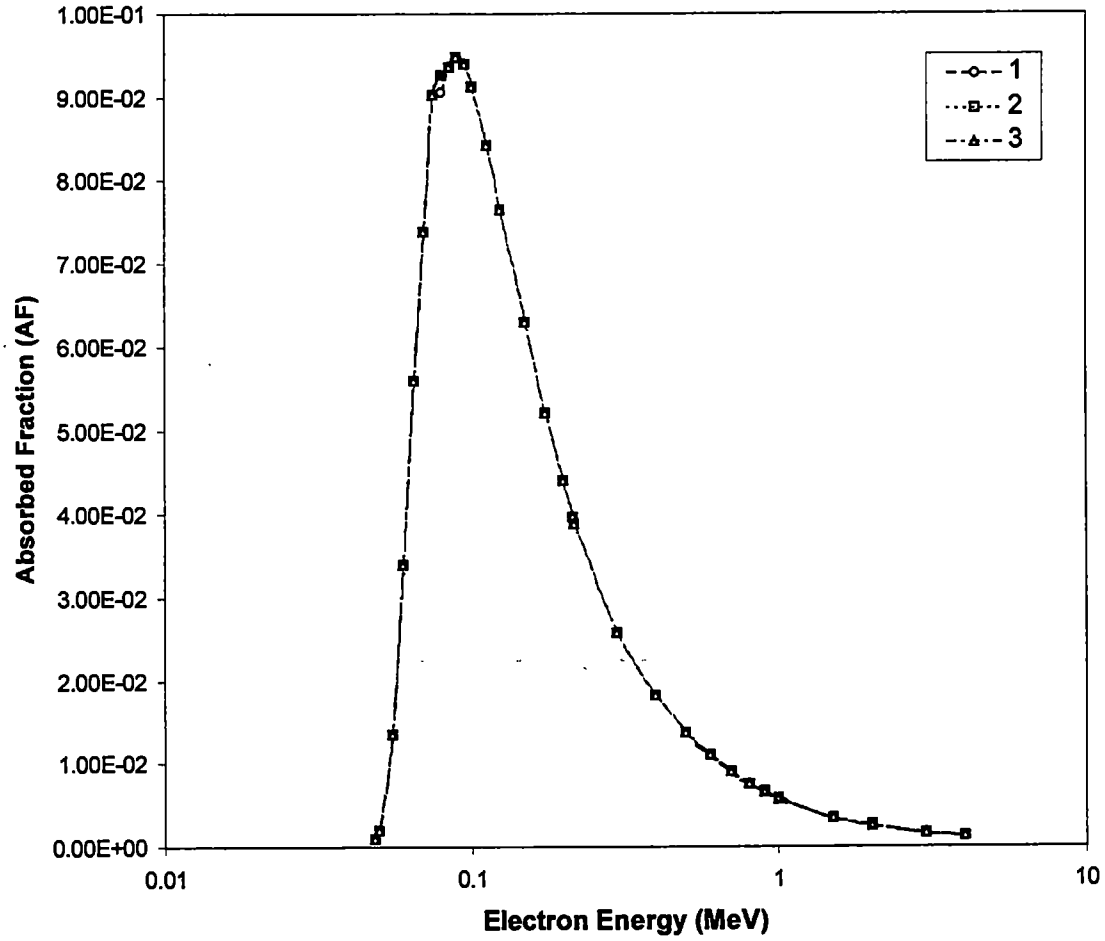


Figure 4.9 Electron absorbed fraction results using MCNP4B for three cylinders (the external thickness beyond the basal cells are (1) 0.295 cm, (2) 0.195 cm and (3) 0.095 cm respectively, the surface area is 20 cm^2 and the radius is 0.25 cm).

tissue of 0.095 cm and 0.195 cm beyond the basal cell layer) there are no differences noted from 0.0485 MeV up to 0.6 MeV and 0.8 MeV respectively, except at 0.08 MeV (difference of 2.09%). Given the above observation, and since the differences are small, we conclude that changing the soft tissue thickness beyond the receptor (basal cells) will not effect the values of the electron absorbed fractions for the cylinder model published in ICRP 66.

4.10 Electron Absorbed Fraction Using MCNP4B (Material Effect) (Case 7)

In this case study, the original input deck is used to create a new batch. This new batch consists of 31 input files. In this new batch, the material card in the input deck is modified so that the materials used are air and adult male soft tissue, while air and water are used in the original one. The elemental composition of the tissue (percentage by mass), mass density, ρ (kg m^{-3}), and electron density, η_0 (m^{-2} x 10^{26}) for an adult male is taken from Table 2.1 in chapter 2. The outputs of the MCNP4B runs are summarized in Table 4.35 in Appendix B.

4.10.1 Discussion

A plot of the electron absorbed fractions versus the electron initial energy is presented in Figure 4.10. Plotted are the electron absorbed fraction data taken from Table 4.5 and the electron absorbed fraction data taken from Table 4.35 in Appendix

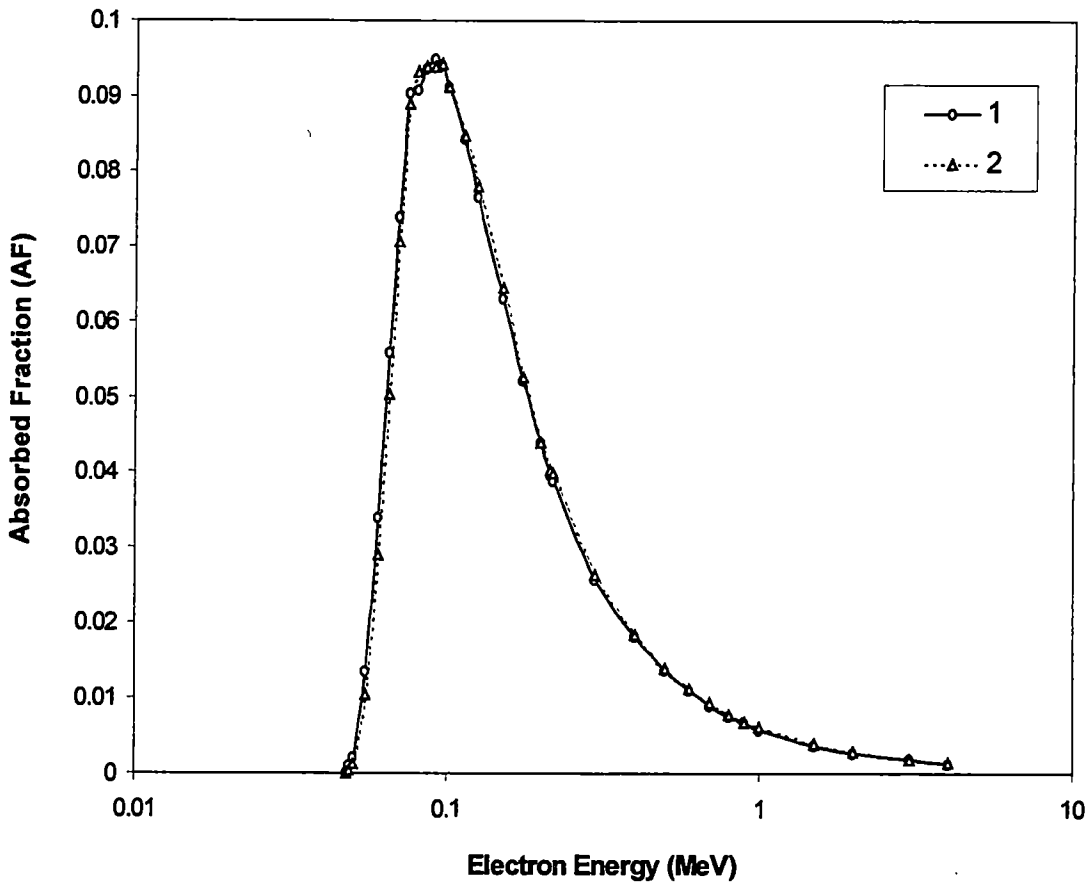


Figure 4.10 Electron absorbed fraction results using MCNP4B for two identical cylinders (the materials used are (1) air and water and (2) air and tissue).

B. The percentage differences between the electron absorbed fractions obtained from Table 4.5 and Tables 4.35 are tabulated in Table 4.36 in Appendix B. The maximum difference is 48.8%. This maximum occurs at 0.0485 MeV (first energy in Table 4.36). Note that in Table 4.36, the differences decrease as the energies increase from 0.0485 MeV to 2 MeV where it reaches a zero value at 2 MeV. Then it fluctuates to a maximum of 7.24% at an energy of 1.5 Mev. Except at low energies, we conclude that the electron absorbed fractions published in ICRP 66, which are obtained using air and water are unchanged when soft tissue is used instead of water.

4.11 Effect of Gender and Age on the Electron Absorbed Fraction (Case 8).

The differences between male, female and adolescent noses include:

- Soft tissue composition (see Tables 2.1 and 2.2 in chapter 2).

- Thickness of the external tissue beyond the target (basal cells). For males it is 0.295 cm and for females and adolescents we assume external thicknesses of 0.195 cm and 0.095 cm respectively.

- Nose size for each gender. We will assume the nose sizes for female and adolescents are reduced by 8% and 50% of the male nose size respectively.

Two new input decks are created to represent the female and adolescent models. In turn, each input is used to generate 31 copies where we modified the energy, the E-Step and substep in each copy to account for the various electron energies. The outputs are summarized in Tables 4.37 and 4.38.

4.11.1 Discussion

Plots of the electron absorbed fraction versus the electron initial energy are presented in Figure 4.11. Plotted are the electron absorbed fraction data taken from Table 4.35 and the electron absorbed fraction data taken from Tables 4.37 and 4.38. The percentage differences between the electron absorbed fractions obtained from Table 4.35 and Tables 4.37-4.38 are tabulated in Tables 4.39-4.40 in Appendix B. The maximum percentage differences from Tables 4.39-4.40 are 8.92% and 11.2%, which occur at energy of 0.0485 MeV. Except at low energies we conclude that the electron absorbed fractions published in ICRP 66 can be used for females and adolescents, as well as for males.

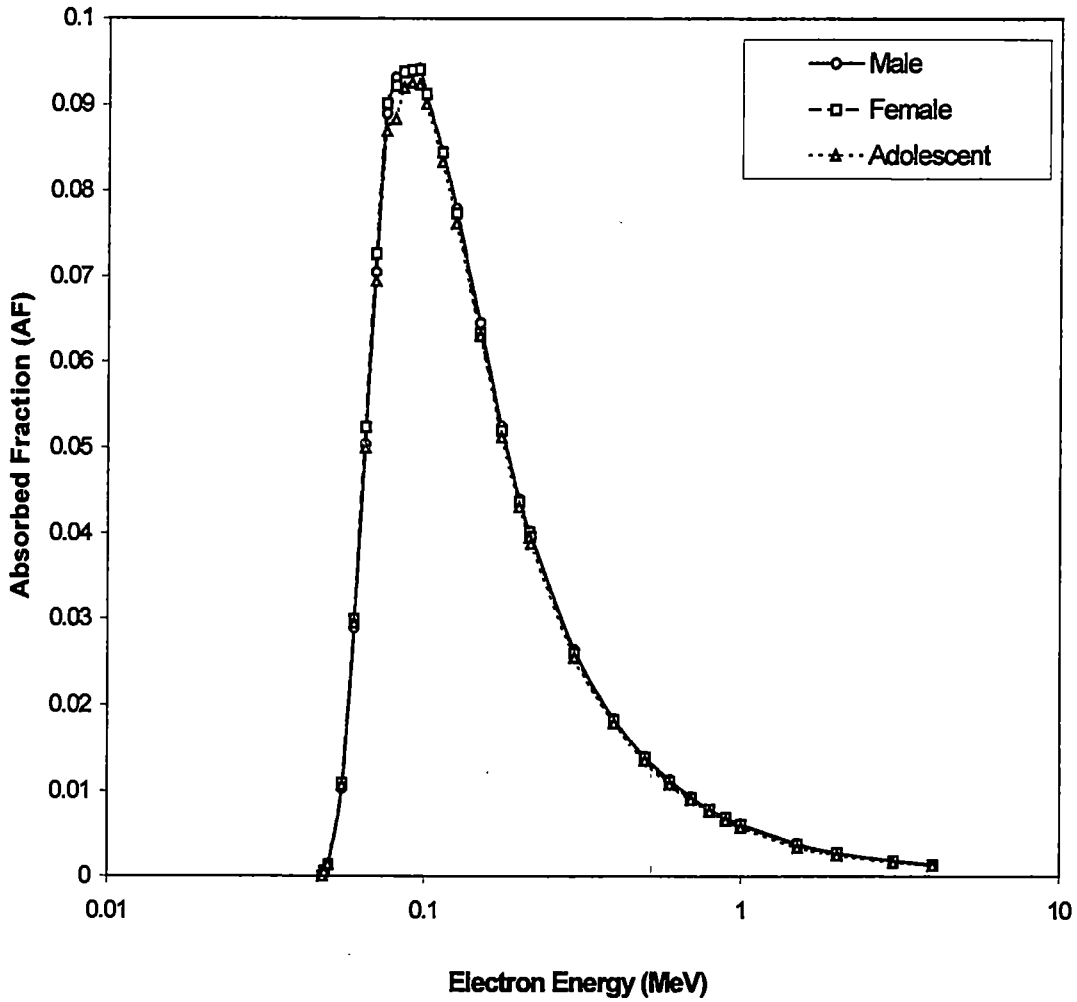


Figure 4.11 Electron absorbed fraction vs. energy (MeV) for male, female and adolescent cylindrical models (note the materials used are air and soft tissue).

4.12 MCNP4B vs. MCNP4C

The absorbed fraction data of Fig. 4.8 for the cylinder model exhibited a peak in the absorbed fraction at electron energy of 0.075 MeV. The absorbed fraction data in all geometric regions in the problem showed a similar structure or artifact (see Fig. 4.12), but it is more pronounced in the basal cell region. This artifact is also seen as a small shoulder in the cylinder model of Fig. 4.3. However, the structure is more pronounced in the truncated cone model in Chapter 5. The structure is not the consequence of any errors in the input decks and is present in different versions of the MCNP code (see Figure 4.13 and 4.14). The magnitude of the artifact appears to be related to the geometry model. In future work, efforts should be devoted to additional investigations to understand the origin of this artifact in the absorbed fraction data.

4.13 Absorbed Fraction as a Function of Basal Cell Depth

Since the electron absorbed fraction values obtained herein and in the ICRP Publication 66 based on the assumption that the basal cells (cells at risk) is located under the epithelium layer with average depth of 40 μm and this assumption represent the best judgment, we use MCNP4B to calculate the energy deposition in

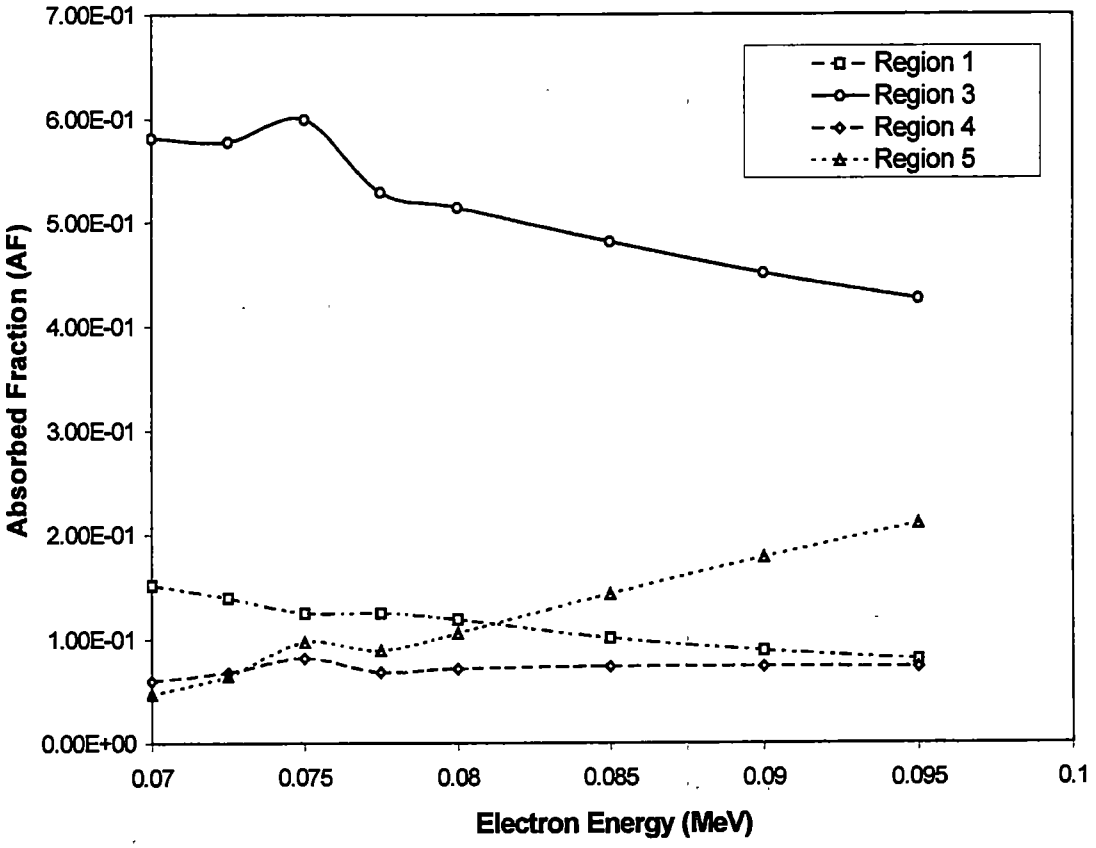


Figure 4.12 Electron absorbed fractions in all ET_1 regions using a cylinder model and the MCNP4B code.

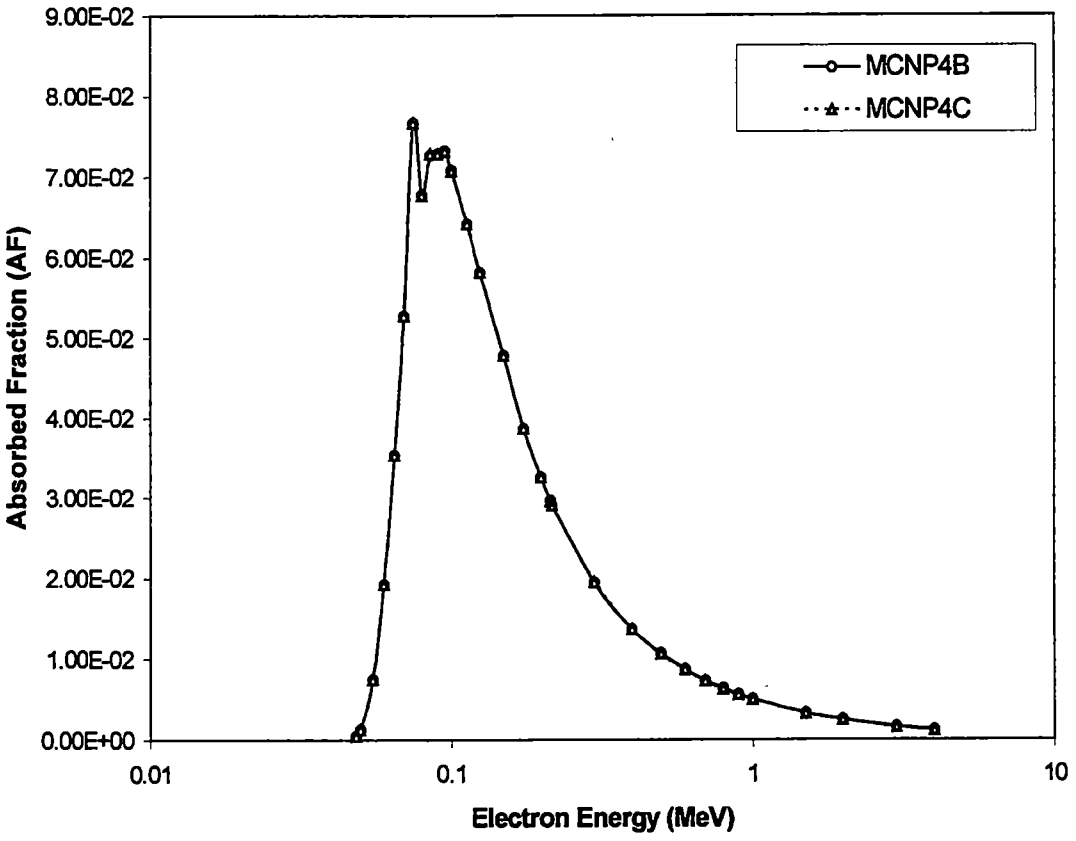


Figure 4.13 Electron absorbed fraction in the basal cells region using MCNP4 (B&C) and a cylinder model (10 cm^2 inner surface area and 0.76394 cm radius).

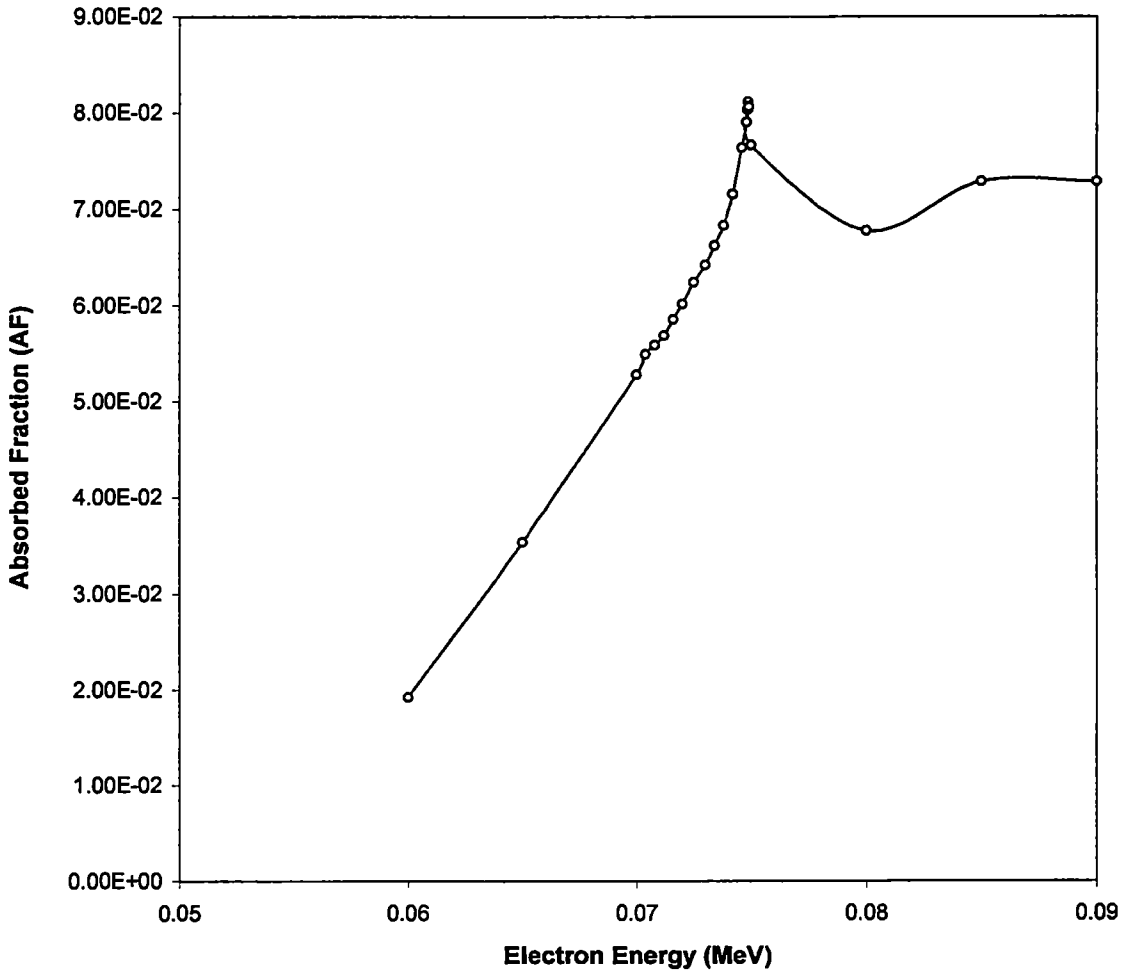


Figure 4.14 Electron absorbed fraction in the basal cells region using MCNP4C and a cylinder model (10 cm^2 inner surface area and 0.76394 cm radius) for energies from 0.06 MeV to 0.09 MeV.

the region of interest (a 10 μm soft tissue target) under epithelium layer with thicknesses vary from 0 to 150 μm, the incident electron energy is 100 Kev. The results are summarized in Table 4.43 in Appendix B. Plot of the results (energy deposited and electron absorbed fraction vs. energy in MeV illustrated in Figure 4.15.

4.14 Discussion and Conclusion

A major feature of the HRTM is its capability to provide estimates of the dose to the extrathoracic airways. However application of the model, as presented in Publication 66, yields dose estimates for the ET_1 region that appear to significantly overestimate doses for beta emitting radionuclides. The possible overestimates may be a consequence of difficulties in the models describing the deposition and clearance of particulate matter from the ET_1 region, or problems in the dosimetric model.

Etherington *et al.* (1998) carried out an experimental study to examine the deposition and clearance of inhaled particles in the nasal airways. Their analysis concluded that the dose to the ET_1 region might be slightly higher than estimated.

In this chapter, the calculated electron absorbed fractions have been presented for monoenergetic electrons using MCNP4B and the cylindrical geometry model for the ET_1 region specified in ICRP Publication 66. At energies above 80 keV, differences between the results obtained in this work (using MCNP4B) and

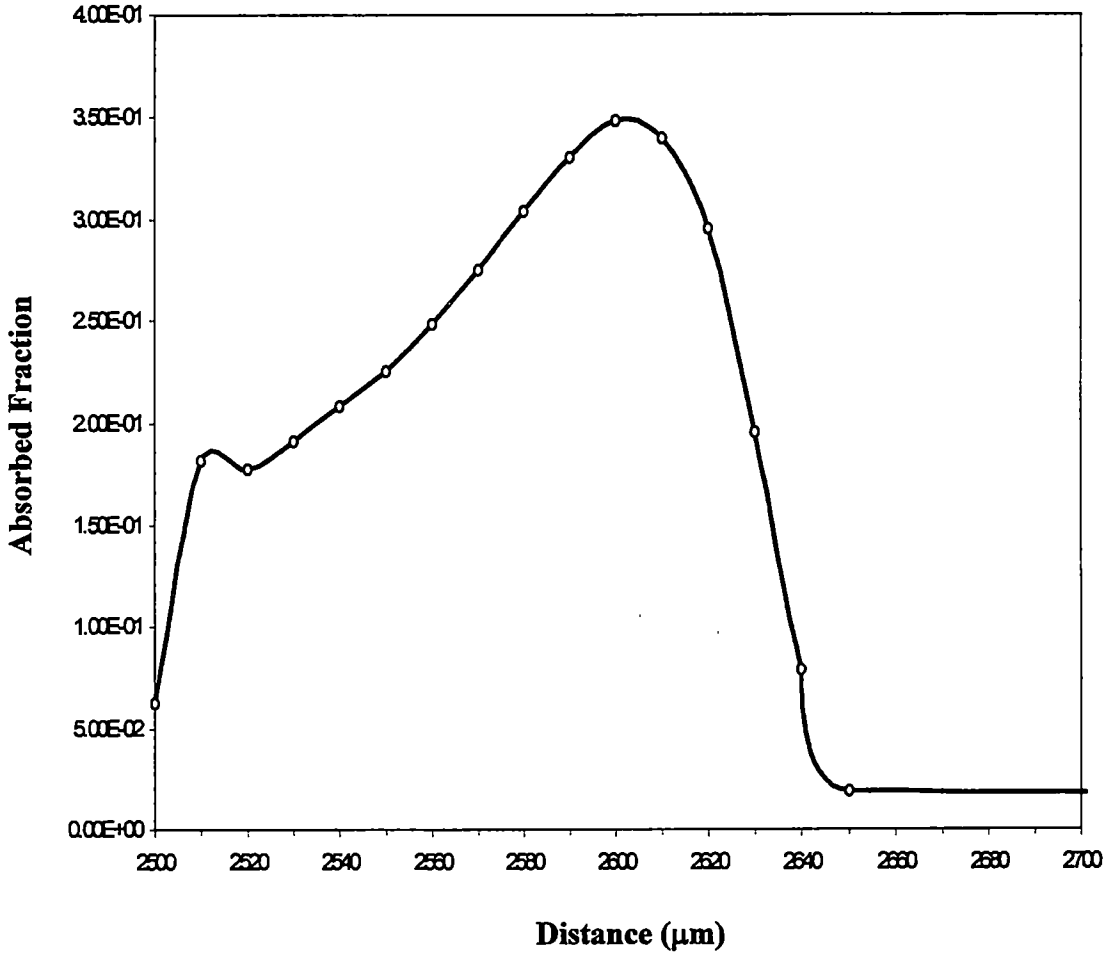


Figure 4.15 Electron absorbed fraction vs. distance (μm) from the surface source for 100 Kev incident electron.

ICRP 66 (using EGS4) are about 20%. Thus it is clear that the electron absorbed fractions tabulated in ICRP Publication 66 are reasonable, and the use of a particular computer code is not responsible for the overestimates of the ET_1 doses.

Our studies show that when the cylinder model is used, the electron absorbed fraction is independent of the source location (the electron absorbed fractions are almost the same in case studies 1 and 2 and in the original case). This implies that if the radioactive material is deposited in the upper half or lower half of the nasal vestibule, the electron absorbed fraction is the same as if the radioactive material is deposited on the entire inner surface (upper and lower halves).

Furthermore, there is no significant difference in the electron absorbed fraction if the cylinder inner surface area is increased by 10%, 25%, 50%, and 75% or decreased by 10% and 25%. However, when the decrease in the surface area of the cylinder is more than 25%, the maximum percentage differences start to increase (4% to 10.3%). Therefore, since the calculated electron absorbed fractions will be affected by these decreases, a new electron absorbed fraction should be obtained for nose sizes smaller than the original nose model ($\leq$ %75) used to obtain the electron absorbed fractions tabulated in Table 4.5. This finding applies to children and people from the Far East.

The difference in the electron absorbed fraction is small when the cylinder radius is increased to 0.3 cm. The largest difference is 6.67% corresponding to an energy of 0.055MeV. The smallest difference (0%) corresponds to an energy of 0.3 MeV. However, when we increase the cylinder radius to 0.35 cm and to 0.76394 cm, the differences in the electron absorbed fraction increase. The largest differences are 32.4% and 31.8% corresponding to energies of 4.0 MeV and 0.06 MeV. Although the percentage differences in the electron absorbed fraction are larger at higher energies for cylinders with larger radii, it has been assumed in ICRP Publication 66, for dosimetry purposes, that all electron absorbed fractions are independent of age and body size. Therefore, the values of the electron absorbed fraction for electrons given in Table H.2. in Annex H should be usable for any body size, age and gender. However, our results indicate that one should either adjust the electron absorbed fractions in Table H.2 in Annex H of ICRP 66 to take into account the nostril radius, if it is more than 0.3 cm, or one should use new electron absorbed fractions obtained for the larger radius.

In ICRP 66, the outer tissue layer (the layer beyond the basal cell) is defined as a low density absorber. There is no indication that this region was considered when estimating the electron absorbed fractions (electrons scatter into this region and also scatter back to the target). However, our study shows that the largest differences between the original case (cylinder with an outer tissue layer thickness of 0.295 cm) and identical cylinders with an outer tissue layer of 0.095cm and 0.195 cm are only 4.53% and 1.71%. Given the above observation, and since the differences

are small and occur only at high energies, we conclude that changing the soft tissue thickness beyond the receptor (basal cells) does not effect the values of the electron absorbed fractions.

When we use soft tissue instead of water, the largest difference (48.8%) corresponds to an energy of 0.0485 MeV, and decreases as the energy increases. Except at low energies, we conclude that the electron absorbed fractions published in ICRP 66 using water are unaffected by using the actual soft tissue composition.

When we compare female and adolescent nose models to the male model (variations due to nose size, material composition, and external nose thickness beyond the target (basal cells)), we find that the maximum differences are 8.92% and 11.2% for the female and adolescent models respectively. These maximum differences occur at an energy of 0.0485 MeV. From this result, we conclude that the electron absorbed fractions published in ICRP 66 could be used not only for the Caucasian male but also for the Caucasian female and adolescent.

CHAPTER 5

A New Nose Model (Truncated Cone Model)

5.1 Introduction

In ICRP 66, all electron absorbed fractions are assumed to be independent of age and body size (ICRP 1994, p. 87). Therefore the values of the electron absorbed fraction for electrons given in Table H.2 in Annex H of Publication 66 should be usable for any body size, age and gender. Scaling of the airway dimension for age and genders are considered only when calculating the tissue mass of ET_1 for males, females and adolescents (ICRP 1994, p. 19). The ET_1 dimensions are assumed to scale in proportional to the diameter of the trachea in each subject (Yu and Xu, 1987; Swift, 1989). In turn, the dimensions of the trachea were found to be related to the body height (Phalen *et al.* 1985). The scaling factor SF, is the ratio of the trachea diameter or length in the subject compared to that in the reference man which is expressed in the following equation:

$$SF = a(H_S - 1.76) + 1 \qquad 5.1$$

where a is constant (a values are tabulated in ICRP 66 page 19), and H_S is the height of the subject (male, female, and adolescent other than reference man). However, the

results of the investigation of the ICRP 66 nose model (cylindrical model) presented in Chapter 4, indicate that the electron absorbed fractions will not change significantly with variations in the nose size (cylinder height, surface area, and radius), except for high energies and large radii. To account for results at these high energies and large radii, we propose a new model for the anterior nose based on a truncated cone geometry.

In this chapter we use the MCNP4B code to obtain the electron absorbed fractions in ET_1 using the newly proposed model (truncated cone). We do this for two reasons: (1) to investigate the effect of changing the geometry on the electron absorbed fractions by comparing the electron absorbed fractions obtained using the truncated cone to that obtained using the cylinder model, and (2) to study the effect of changing the source location, and the truncated cone size (surface area and radius) on the electron absorbed fractions. The following cases are discussed in more detail to satisfy the second reason.

1. In cases 1 and 2 we change the source location on the truncated cone inner surface (on upper and lower half of the truncated cone inner surface) to determine if the change in the source location affects the value of the electron absorbed fraction.

2. In cases 3 and 4 we change (increase and decrease) the inner truncated cone surface area to study how the electron absorbed fraction values are effected with the above changes.

3. In cases 5 and 6 we change (increase and decrease) the bottom radius of the truncated cone model to study its effect on the electron absorbed fractions.

5.2 Proposed Model for the Interior Nose

The human external nose (ET_1) is pyramidal in shape, and consists of two nasal vestibules (ICRP 1994, p. 123). In this dissertation we propose a new, truncated cone model (frustum of a cone) to represent each nasal vestibule for the following reasons:

- The nose has pyramidal shape, while the nasal vestibule is elliptical in shape.

- Some people have circular nostrils. Therefore, their nasal vestibules are real truncated cones.

5.3 Measurement and Calculation

Based on my nose measurements, the circumference of the bottom circle (the nostril) is 4.8 cm, the circumference of the top circle (the top of the nasal vestibule) is 2.5 cm, and the height is 2.55 cm. Let us assume that the surface area for both nasal vestibules is 20 cm^2 and both nasal vestibules have equal surface areas. Then, each nasal vestibule has a 10 cm^2 surface area and we obtain:

$$\pi r_{01} S - \pi r_{02} L + \pi r_{02}^2 = 10 \ \text{cm}^2 \qquad 5.2$$

where $r_{01} = 0.76394$ cm, is the radius of the nostril (bottom circle) and $r_{02} = 0.3789$ cm , the radius of the top circle. From Figure 5.1:

$$\frac{r_{01}}{S} = \frac{r_{02}}{L} \Rightarrow S = \frac{(r_{01} L)}{r_{02}} = 1.92L .$$

Replacing S with L in equation 5.2, and solving for L, we have L=2.82985 cm, and therefore S = 5.43331 cm. Also from Figure 5.1:

$$\sin\theta = \frac{r_{01}}{S} = 0.14060 \Rightarrow \cos\theta = 0.99006 = \frac{h}{S} \Rightarrow h = 5.37934 \quad cm;$$

$$\cos\theta = \frac{m}{L} \Rightarrow m \Rightarrow L = 2.80174 \quad cm; \ \tan\theta = 0.14201 \Rightarrow \tan^2\theta = 0.02017;$$

h-m = 2.57760 cm. Then the data to be entered into MCNP for this surface are:

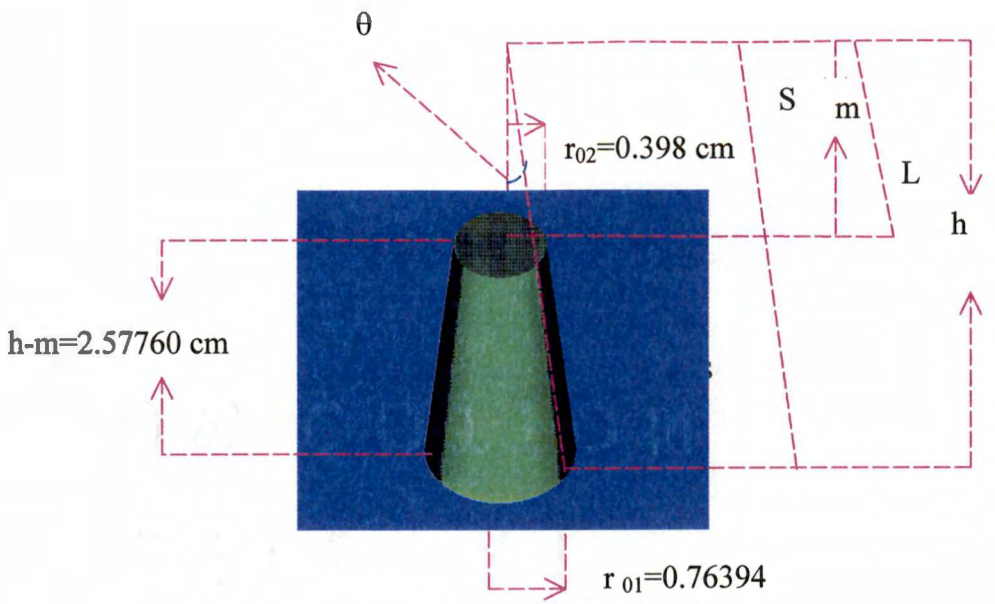


Figure 5.1 The shape of Mr. Moussa's right nasal vestibule

PZ = 0, PZ = 2.57760, KZ = 5.37934, $\tan^2\theta$ = 0.02017 and –1 for using the half cone with the top up.

Figure 5.2 shows the various layers of the above model. The cells, from inside out, are as follows:

1. The vestibule cavity: filled in air. The bottom and top radii are 0.76394 cm and 0.39789 cm respectively.

2. The source surface area: cover the inner side of the vestibule, with a 1μm thickness of air.

3. An epithelium tissue layer with 40 μm thickness.

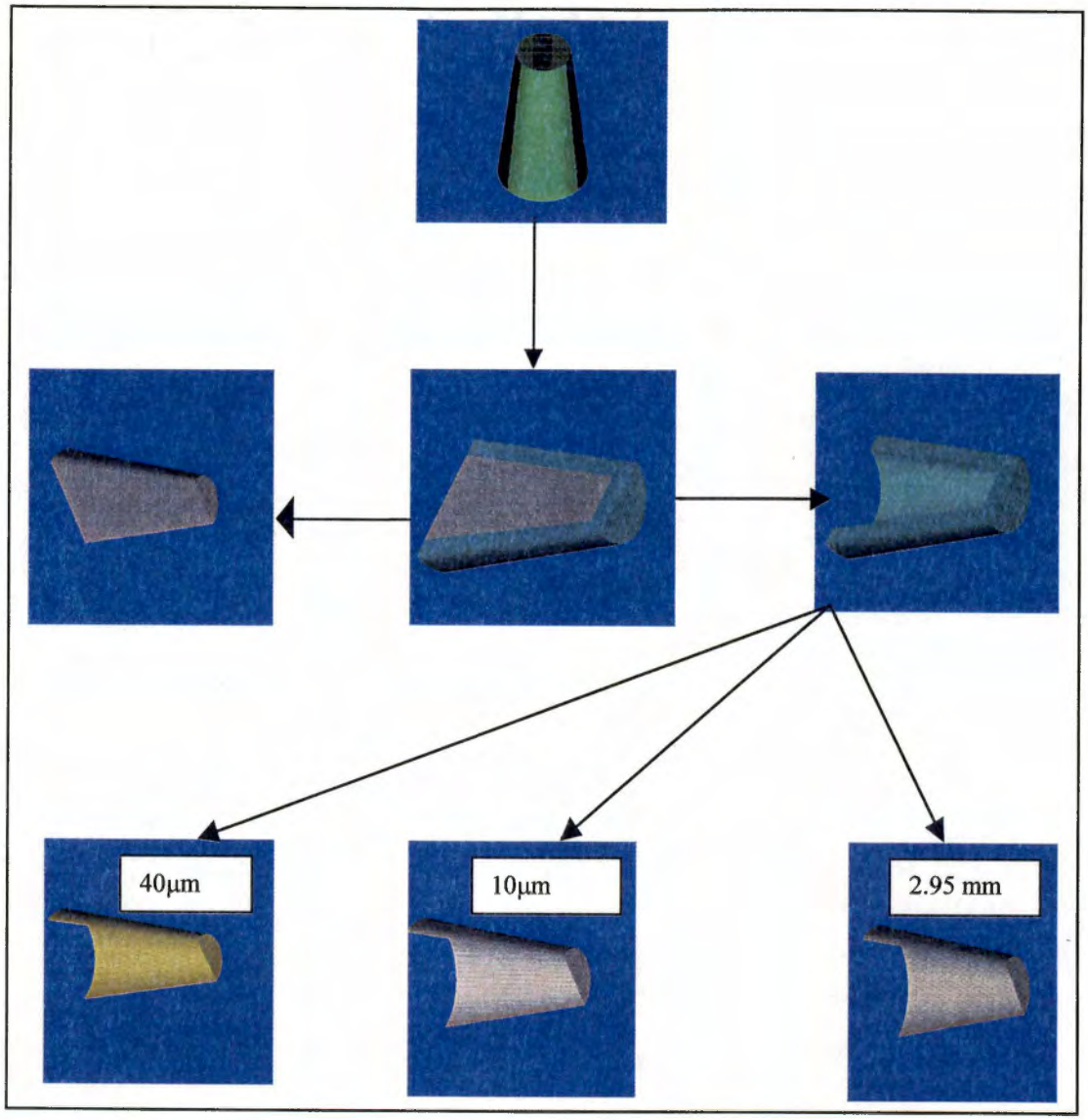


Figure 5.2 The proposed model for one vestibule and all covered layers.

4. The receptor layer (basal cells) with 10 μm thickness.

5. The skin layer (covers the basal cells) with 0.295 cm thickness.

A Matlab® program is developed to generate output data for different truncated cone sizes. These data are used to create an input file for MCNP4B. The detailed program is listed in Appendix C. The following is an example of the output from the Matlab program:

- Data used to describe the surface source cell are:
  PZ = 0, PZ = 2.5775, KZ = 5.37863, $\tan^2\theta$ = 0.02017, and –1 for using the half cone with the top up.

- Data used to describe the 1st layer after the source (40 μm = 0.004 cm):
  PZ = 0, PZ = 2.5816, KZ = 5.40778, $\tan^2\theta$ = 0.02017 and –1 for using the half cone with the top up.

- Data used to describe the 2nd layer after the source (10 μm thick = 0.001 cm): PZ = 0, PZ = 2.58260, KZ = 5.41490, $\tan^2\theta$ = 0.02017 and –1 for using the half cone with the top up.

- Data used to describe the 3rd layer after the source (0.295cm):
  PZ = 0, PZ = 2.8776, KZ = 7.5130, $\tan^2\theta$ = 0.02017 and –1 for using the half cone with the top up.

5.4 MCNP4B Input

An input file is created for use in the MCNP4B code in which the nasal vestibule is modeled by four, concentric, bottom open truncated cones (Figure 5.2). The dimensions are specified in the previous section. The parameters considered in this input file are as follow:

- 31 copies are generated from the original input file to be used for 31 different energies.

- Monoenergetic electrons of energy ranging from 0.0485 MeV to 4 MeV using the energy values specified in Table H.2 of ICRP Publication 66 are used.

- At each energy, the calculations involve tracking 100,000 electrons emitted uniformly from the surface of the inner surface of the second truncated cone.

- The Esteps and substeps used in this model are the same as the Esteps and substeps used for the cylinder model in Chapter 4.

- The physics parameters used in this model are the same as the physics parameters used for the cylinder model in Chapter 4.

5.4.1 Surface and cell card for truncated cone model (original case)

A cone parallel to the z-axis can be expressed by the following equation:

$$\sqrt{x^2 + y^2} - t(Z - \bar{Z}) = 0 \qquad 5.3$$

The card entry contains KZ, $\bar{Z}$, t^2, and ± 1; where KZ represent a cone on z-axis, $\bar{Z}$ is the cone vertex, t is the tangent of the opening angle of the cone (note that t^2 is entered), and +1 considers only the positive (right hand) sheet of the cone (the cone stands on its head) while –1 consider the left hand sheet of the cone (the cone stands on its base) (Bielajew *et al.* 1991). In our model, the left-hand sheet of the cone is used (the entry on the surface card is -1) and the calculated data in paragraph 5.3 are introduced in the input as a surface card that is used to build all cell cards. A copy of MCNP4B input deck (for an electron energy of 0.0485 MeV) is presented in Appendix C.

5.5 Electron Absorbed Fraction for Cylinder vs. Truncated Cone Model Using MCNP4B (Geometrical Differences)

To investigate changes in the electron absorbed fraction due to a change in the model geometry only, we run the MCNP4B code on the 31 input decks for the new model (truncated cone) and a cylinder model (the radius of the cylinder is 0.25 cm and its inner surface area is 10 cm^2). The results (energy depositions) are divided

by the initial energy to obtain the electron absorbed fractions (*AF*), which are tabulated in Table 5.1 and Table 5.2 in Appendix C.

5.5.1 Discussion

A plot of the electron absorbed fraction versus the electron initial energy is presented in Figure 5.3. Plotted are the electron absorbed fraction data taken from Tables 4.35, 5.1 and 5.2. The first two plots are almost identical (represent cylinders with inner surface areas of 20 and 10 cm^2 and 0.25 cm radius). The third plot represents the electron absorbed fraction for the truncated cone model (data taken from Table 5.1). The percentage differences between the electron absorbed fraction obtained from Table 5.1 and Table 5.2 are tabulated in Table 5.3 in Appendix C. The maximum difference is 21.4%, which occurs at an energy of 0.06 MeV. Also the percentage differences are between 9% and 15% when the electron energy is between 0.055 MeV and 0.7 MeV. Therefore, we conclude that changing the model has some effect on the electron absorbed fraction values. Note that the comparison here is between a cylinder and a truncated cone, both having a 10 cm^2 inner surface area. In addition, from Figure 5.3 it is noted that the electron absorbed fraction is almost identical for a cylinder model with 20 cm^2 and 10 cm^2 surface areas.

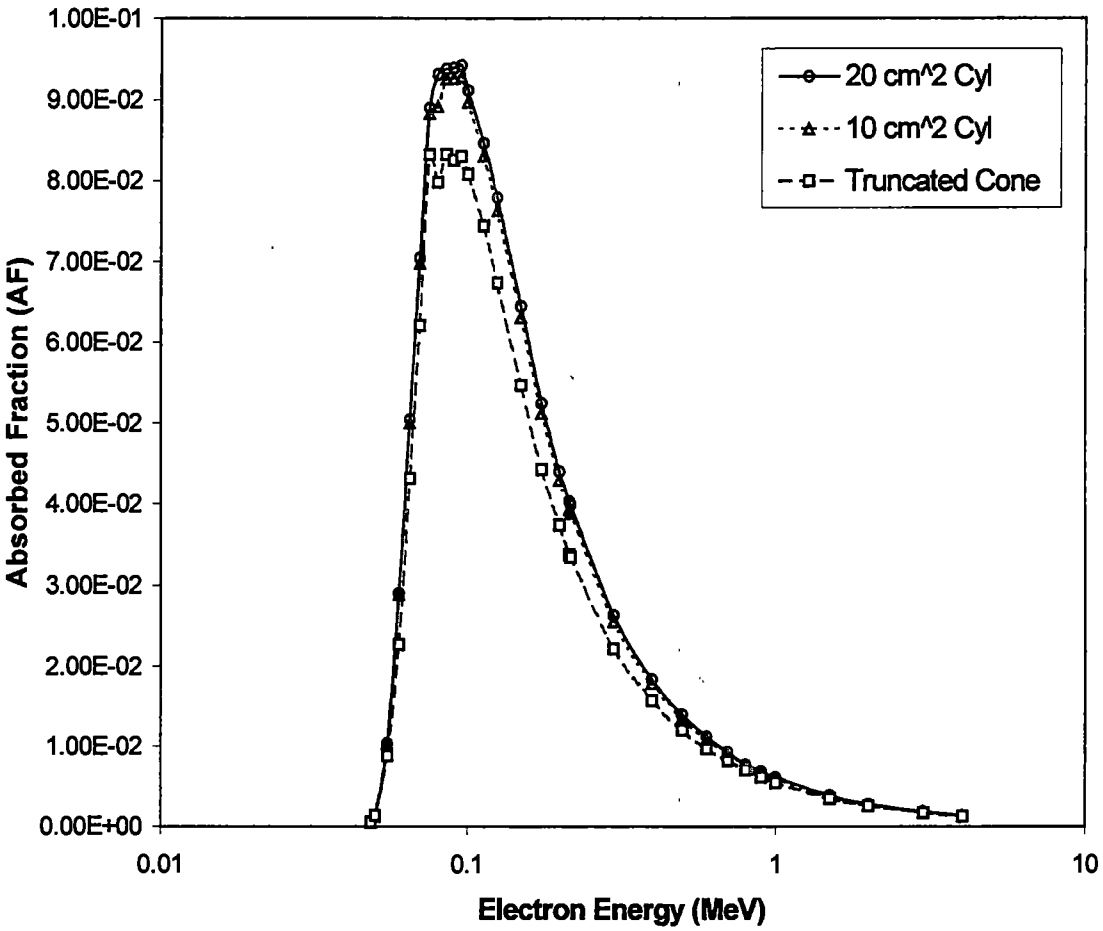


Figure 5.3 Electron absorbed fractions for cylinder models (0.25 cm radius, 20 cm^2 and 10 cm^2 surface areas) and a truncated cone model (10 cm^2 surface area and 0.76394 cm and 0.39788 cm bottom and top radius).

5.6 Model Validation

The nasal cavity of the human nose is divided into symmetrical halves by the partly cartilaginous and partly bony nasal septum. The stratified squamous epithelium of the facial skin continues through the nostrils into the vestibule. Adult nostrils, as described in ICRP Publication 66, are elliptical in shape and measure 1.5 cm to 2 cm anteroposteriorly and 0.5 to 1 cm transversely (ICRP 1994, p. 123). Taking the upper bound of these two measurements and assuming that elliptical nostrils measure 2 cm anteroposteriorly and 1 cm transversely, we create two truncated cones with bottom radii of 1 cm and 0.5 cm and top radii of 0.5 cm and 0.25 cm. Also, we close these two truncated cones so that they bound the truncated elliptical nasal vestibule, which has an elliptical nostril that measures 2 cm anteroposteriorly and 1 cm transversely, and a top elliptic that measures 1 cm anteroposteriorly and 0.5 cm transversely, as shown in Figure 5.4. Both truncated cones and the elliptical nasal passage have the same assumed height (2.57 cm). Two MCNP4B input decks are created to estimate the electron absorbed fractions for both truncated cones with their vestibule cavities filled with air. The source covers the inner surface of both truncated cones to a 1 μm thickness. There is an epithelium tissue layer with 40 μm thickness, a receptor layer (basal cells) with 10 μm thickness, and the skin layer (covers the basal cells) with 0.295 cm thickness. The results are summarized in Table 5.4 in Appendix C. These are compared with the original results obtained from Table 5.1 using the fact that the elliptical nostril circumference,

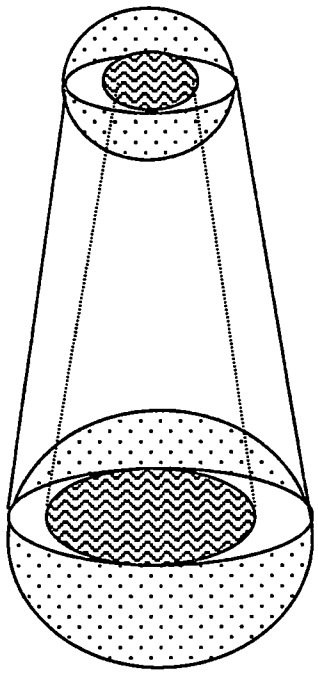


Figure 5.4 Two truncated cones bounding the elliptical nasal vestibule, all three regions have the same height (2.57 cm).

which measures 2 cm anteroposteriorly and 1 cm transversely, is 4.8 cm as obtained using the equation:

$$L = 4a \int_0^{\pi/2} \sqrt{1 - e^2 \sin^2 u}\, du \qquad 5.4$$

where $e = \sqrt{a^2 - b^2}\,/\,a$ 5.5

and a = 2 cm, b = 1 cm.

5.6.1 Discussion

A plot of the electron absorbed fraction versus the electron initial energy is presented in Figure 5.5. Plotted are the electron absorbed fraction data for the truncated cone model with 13.159 cm^2, 6.298 cm^2, and 10 cm^2 inner surface areas from Table 5.4 (the inner surface areas for the inner, outer, and original truncated cones). All electron absorbed fraction values for the truncated cone model with 10 cm^2 (except the values corresponding to 0.055 MeV and 0.06 MeV) lie between the values of the inner and outer truncated cones (with surface areas of 6.298 cm^2 and 13.1586 cm^2). This implies that the electron absorbed fractions for the truncated cone with 10 cm^2 surface area can be used in a reliable manner to evaluate the dose to an elliptical nasal vestibule, which is bounded by these outer and inner truncated cones.

5.7 Convergnce of Cone Electron Absorbed Fraction to Cylinder Absorbed Value.

To verify the reliability and consistency of the MCNP4B output for the truncated cone geometry, four new batches are created, each consisting of 31 input files. The first batch is for a cylinder model with the cell and surface cards modified so that the cylinder has an inner surface area of 10 cm^2 and a radius of 0.7639 cm. The second batch is for a truncated cone with 10 cm^2 inner surface area and top and bottom radii of 0.3979 cm and 0.7639 cm respectively.

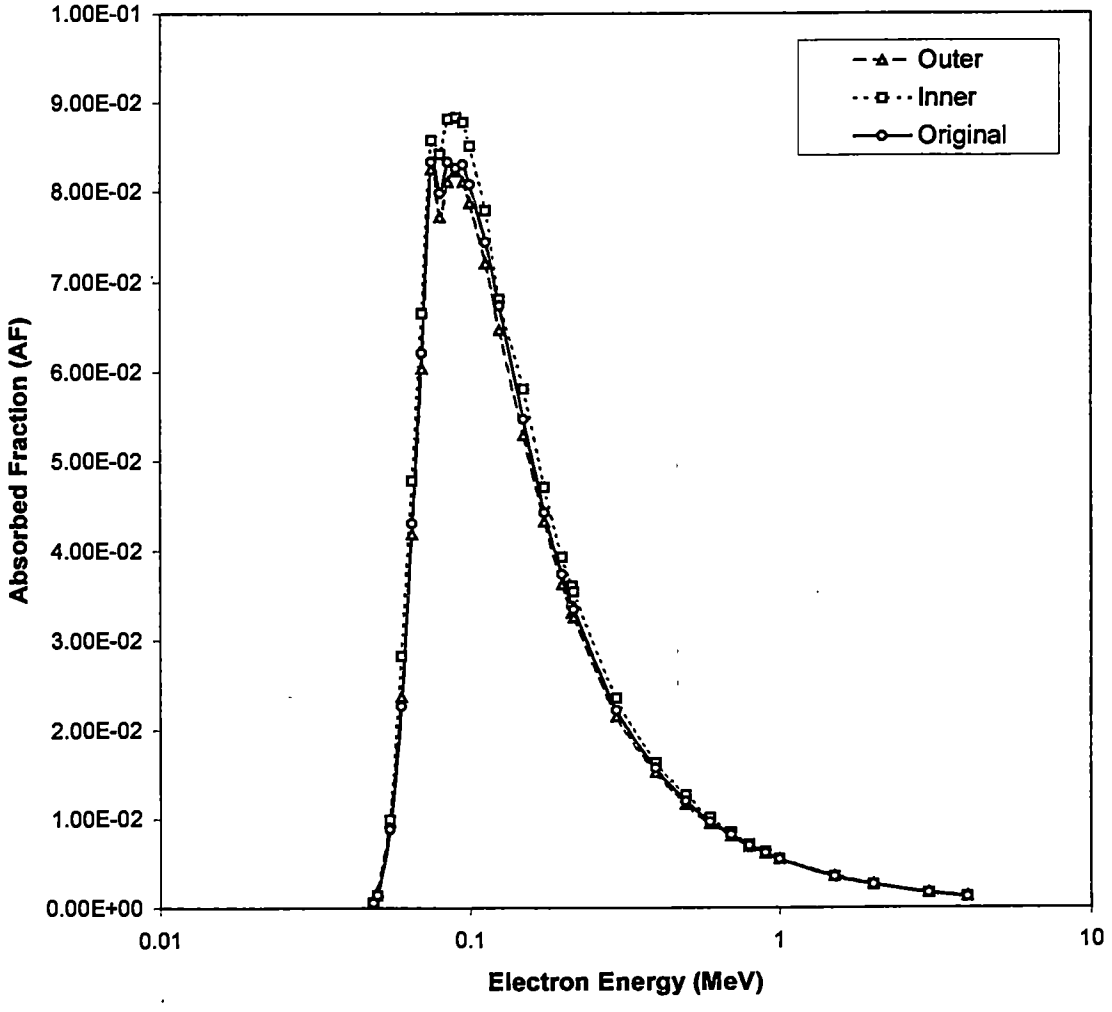


Figure 5.5 Electron absorbed fraction for the original, outer and inner truncated cones.

The fourth batch is for a truncated cone with 10 cm^2 inner surface area and top and bottom radii of 0.6419 cm and 0.7639 cm respectively, (Note: the top and bottom circles are open for the cylinder and truncated cone models). The materials used are air and soft tissue. The outputs of the MCNP4B runs (energy deposited in the basal cell region) are summarized in Tables 5.5 –5.8 in Appendix C.

5.7.1 Discussion

Plots of the electron absorbed fractions versus the electron initial energy are presented in Figure 5.6 for the cylinder and three truncated cones. It is shown in Figure 5.6 that, as the top radius of the truncated cone increases, the electron absorbed fraction values for the truncated cone approach that of the cylinder. This indicates that the MCNP4B is working well and the input files are correct.

5.8 Dimension of the Upper, Lower Half of the Truncated Cone

Since a new model (a truncated cone model) has been introduced, one should investigate if the source location on the inner surface of the new model will change the electron absorbed fraction values. For this reason, we use the upper and a lower half of the truncated cone as a source region. Since we require the upper halves to be equal in the surface area, we need to determine the dimensions of both halves (see Figure 5.1 for variable definition used in this analysis).

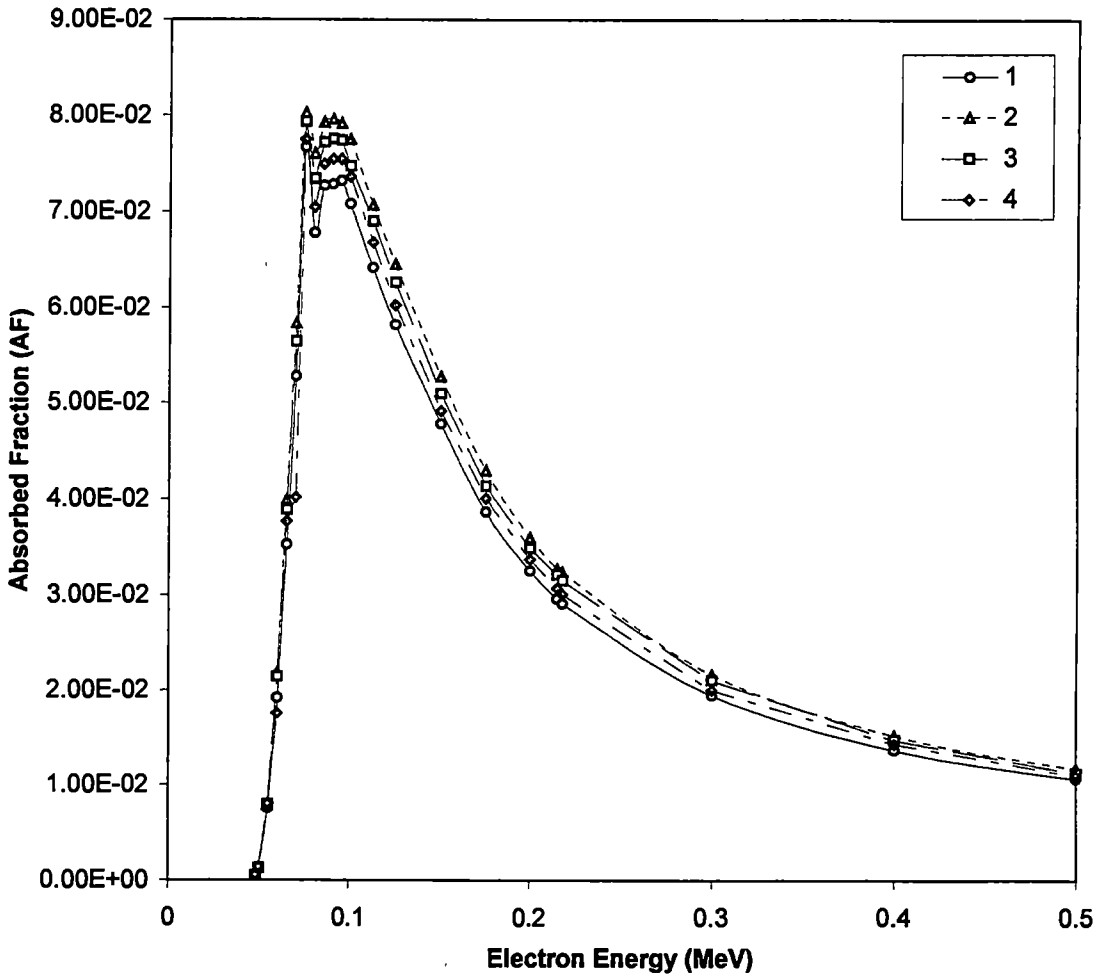


Figure 5.6 Electron absorbed fraction vs. energy (MeV) using cylinder (1) and truncated cone models (top radii of 0.3979 cm (2), 0.5199 cm (3), and 0.6419 cm (4)).

5.8.1 Upper half dimensions

Given the top radius is the same as the original truncated cone top (0.39789 cm), L = 2.82985, sinθ = 0.14060, the surface area = 5 cm^2, the unknowns are r_{0x}, and S_1. Recall from Figure 5.1 and using equation 5.2:

$$\pi r_{01} S_1 - \pi r_{02} L + \pi r_{02}^2 = 5\ cm^2 \qquad 5.6$$

Solving for S_1, then using S_1 to solve for h ($h = \cos\theta * S_1$), and m = ($\cos\theta * L$), the truncated cone height (h-m) = 1.42226 cm, and the radius r_{0x} = 0.59985315 cm.

5.8.2 Lower half dimensions

The lower half height equal is to 1.155 cm (original height minus the upper half height), the top radius is 0.5998 cm (is the same as the bottom radius of the upper half), the bottom radius is 0.76394 cm (the same as the bottom radius of the original truncated cone), and the surface area is 5 cm^2. Note, the top and bottom of the lower half cone are open. The unknowns are S and L. Using equation 5.2 excluding the contribution from the area of the top circle:

$$\pi r_{01} S - \pi r_{02} L = 5\ cm^2 \qquad 5.7$$

where L = S_1= 4.24438 cm, then S = 5.43331 cm.

5.8.3 Source located on the upper half cone (Case Study 1)

In this case, the source expression in the source card (in MCNP input deck) is modified, so that the source is considered as a surface source distributed uniformly only on the inner surface of the upper half of the truncated cone model where the upper half height is 1.42226 cm (the MCNP4B code randomly selects only particles from the upper half of the truncated cone). The output of the MCNP4B runs are summarized in Table 5.9. Table 5.10 is constructed from Table 5.9 and Table 5.1 for comparison. These Tables are found in Appendix C.

5.8.4 Source located in the lower half cone (Case Study 2)

In this case, the source expression in the source card (in MCNP input deck) is modified so that the source is considered as a surface source distributed uniformly only on the inner surface of the lower half of the truncated cone model where the lower half height is 1.155 cm (the MCNP4B code randomly selects only particles from the lower half of the truncated cone). The output of the MCNP4B runs are summarized in Table 5.11. Table 5.12 is constructed from Table 5.11 and Table 5.1 for comparison. These Tables are found in Appendix C.

5.8.5 Comparisons between cases 1 and 2 and the original case

Plots of the electron absorbed fractions versus the electron initial energy are presented in Figure 5.7. Plotted are the electron absorbed fraction data for the original truncated cone model (source distributed on 10 cm^2 inner surface area) the electron absorbed fraction for the original truncated cone model (source distributed on 5 cm^2 inner upper half surface area), and the electron absorbed fraction for the original truncated cone model (source distributed on 5 cm^2 inner lower half surface area). The percentage difference between case 1 and the original case reaches a maximum of 9.77 % at an energy of 0.08 MeV. The percentage difference between case 2 and the original case reaches a maximum of 11 % at an energy of 0.06 MeV.

5.8.6 Discussion

From the above, we conclude that the differences between case 1, case 2, and the original case are due to the source location in the truncated cone model. This is not the case in the cylinder model in Chapter 4, where the electron absorbed fraction for the upper and lower halves of the cylinder model were nearly the same (see Figures 4.4 and 4.5).

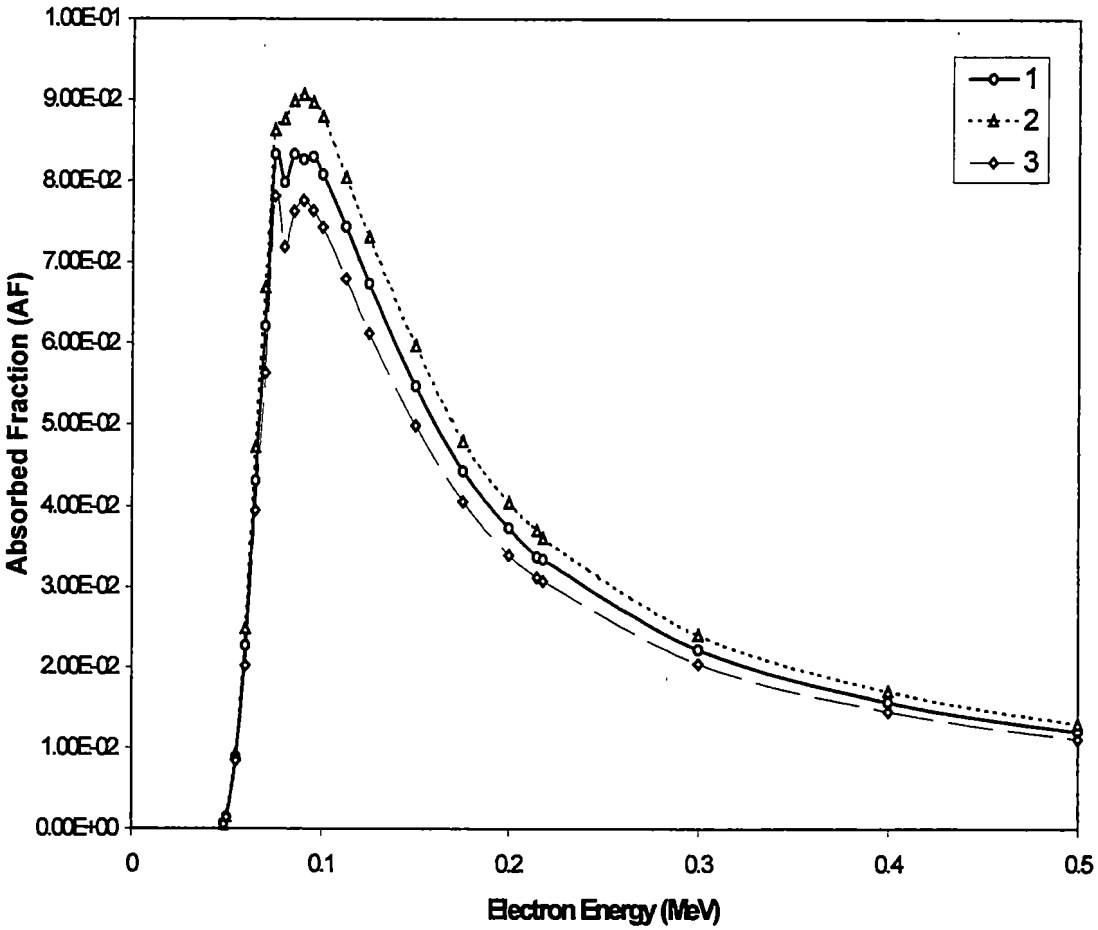


Figure 5.7 Electron absorbed fractions for a truncated cone models (original truncated cone (1), source on the upper half of the inner surface (2), and source on the lower half of the inner surface (3)) vs. energy (MeV).

5.9. The Effect of Surface Area on the Electron Absorbed Fraction

Again, since a new model (a truncated cone model) has been introduced, one should investigate if change in the inner surface of the new model will change the electron absorbed fraction values. For this reason, we change the original inner surface area (10 cm^2) by 8% and 45%.

5.9.1 8% and 45% increases in the surface area (Case 3)

The original input deck (from section 5.5) is used to create two new batches, each consisting of 31 input files. In each file, the cell and surface cards are modified so that the heights of the new truncated cones yield inner surface areas of 10.8 cm^2 and 14.5cm^2. The top and bottom radii are the same as in the original truncated cone (0.3979 cm and 0.7639 cm respectively). The materials used are air and adult male soft tissue. Outputs of the MCNP4B runs are summarized in Tables 5.13 and 5.14. Tables 5.15 and 5.16 are constructed from Tables 5.13, 5.14 and Table 5.1 for comparison. These Tables are found in Appendix C.

5.9.2 Comparison of case study 3 to the original case

Plots of the electron absorbed fractions versus the electron initial energy are presented in Figure 5.8. Plotted are the electron absorbed fraction data taken from Table 5.1, Table 5.13 and Table 5.14. The maximum percentage differences are

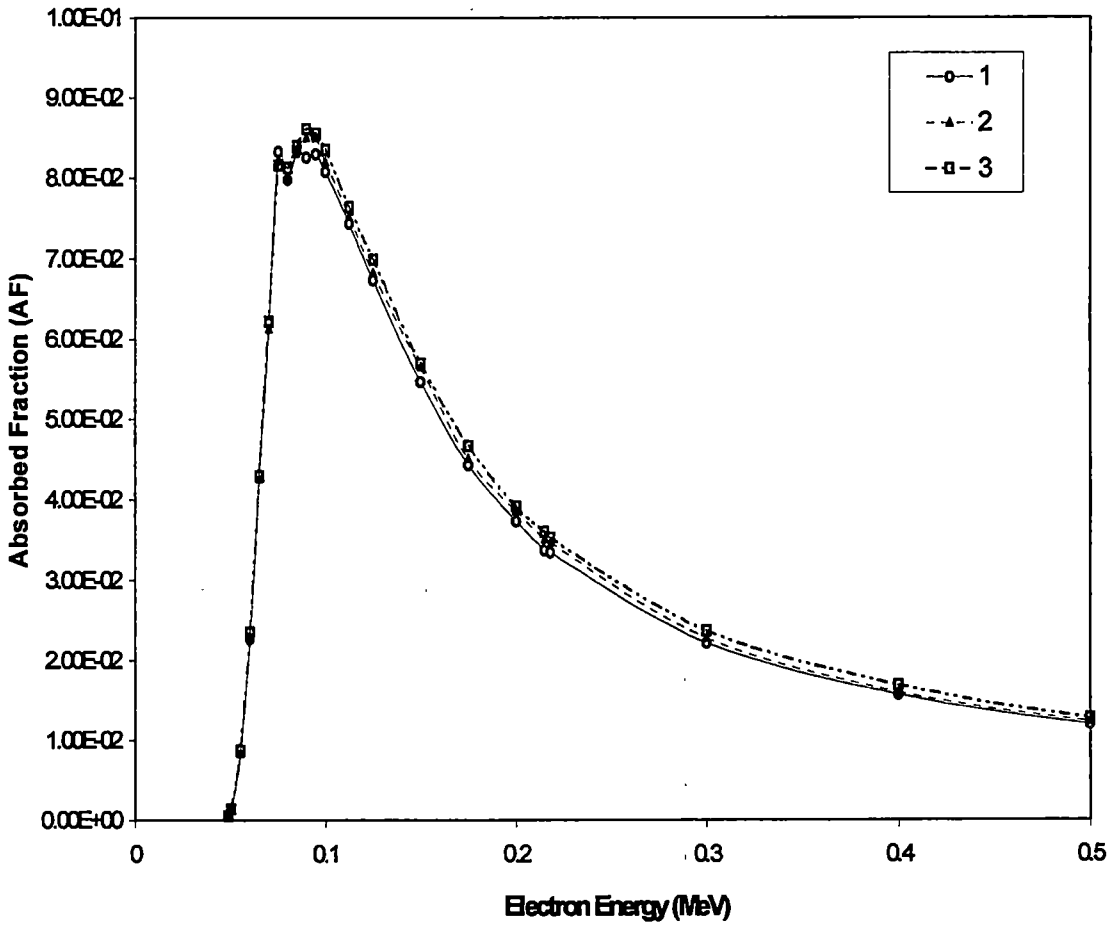


Figure 5.8 Electron absorbed fractions vs. Energy (MeV) for a truncated cone model with inner surface areas of 10 cm^2 (1), 10.8 cm^2 (2), and 14.5 cm^2 (3).

14.3% and 7.69%. These maxima occur at 0.0485 MeV and 3 MeV. Since the maximum differences are relatively small, except for the first two energies in Table 5.15, the electron absorbed fractions are the same for case study 3 as the original case. Therefore, increasing the surface area (up to 45% more than the original surface area) does not effect the values of the electron absorbed fractions.

5.9.3 8% and 45% decreases in the surface area (Case 4)

The original input deck is used to create two new batches, each consisting of 31 input files. In each file, the cell and surface cards are modified so that the heights of the new truncated cones correspond to inner surface areas of 9.2 cm^2 and 5.5 cm^2, given that the top and bottom radii are the same as the original truncated cone (0.3979 cm and 0.7639 cm respectively). The materials used are air and adult male soft tissue. The outputs of the MCNP4B runs are summarized in Tables 5.17 and 5.18. Tables 5.19 and 5.20 are constructed from Tables 5.17, 5.18 and 5.1 for comparison. These Tables are found in Appendix C.

5.9.4 Comparison of case study 4 to the original case

Plots of the electron absorbed fractions versus the electron initial energy are presented in Figure 5.9. Plotted are the electron absorbed fraction data taken from Table 5.1, Table 5.17, and Table 5.18. The maximum percentage differences are

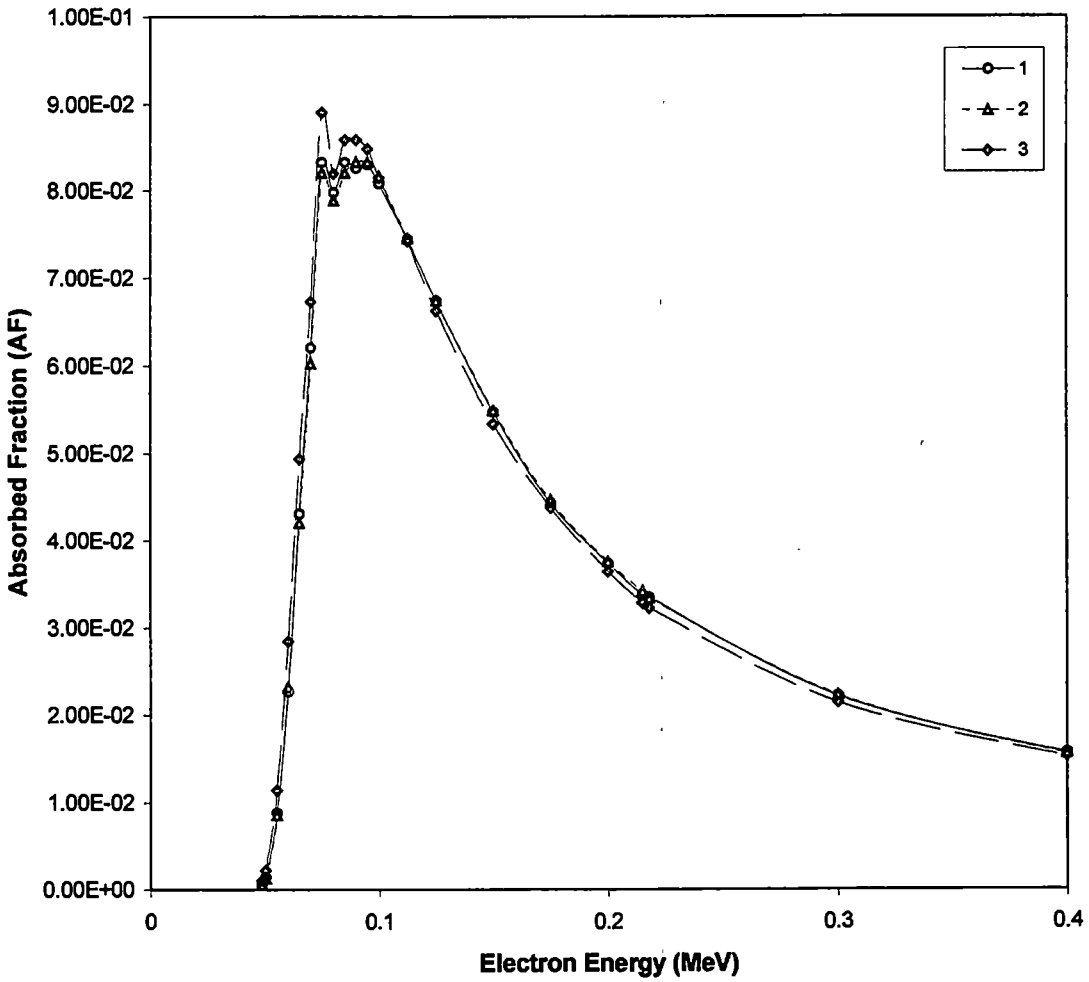


Figure 5.9 Electron absorbed fraction vs. energy (MeV) for a truncated cone model with inner surface areas of 10 cm^2 (1), 9.2 cm^2 (2), and 5.5 cm^2 (3).

7.86% and 81%. These maxima occur at 0.05 MeV and 0.0485 MeV respectively. For the truncated cone with 5.5 cm^2 inner surface area, the percentage difference is very large at 0.0485 MeV then it decreases to 2.17% at 0.09 MeV. We conclude from these results that the electron absorbed fractions for the 10 cm^2 truncated cone inner surface area can still be used if the decrease in the surface area is less than 45%. If the decrease is more than 45% (such as a 50% reduction for children), then we must adjust the electron absorbed fractions to account for the decreases in the surface area.

5.10 The Effect of Bottom Radius on the Electron Absorbed Fraction.

To study changes in the electron absorbed fraction values due to the changes in the bottom radius of the original truncated cone model, we change the original bottom radius by 8% and 45%.

5.10.1 8% and 45% increases in the bottom radius (case 5)

The original input deck is used to create two new batches, each consisting of 31 input files. In each file, the cell and surface cards are modified so that the height of the new truncated cone corresponds to an inner surface area of 10 cm^2 given that the top radius is the same as the original truncated cone (0.3979 cm). The truncated cones have bottom radii that are 0.825 cm and 1.1078 cm respectively.

The materials used are air and adult male soft tissue. The outputs of the MCNP4B runs are summarized in Tables 5.21 and 5.22. Tables 5.23 and 5.24 are constructed from Tables 5.21, 5.22, and Table 5.1 for comparison. These Tables are in Appendix C.

5.10.2 Comparison between case 5 and the original case

Plots of the electron absorbed fractions versus the electron initial energy are presented in Figure 5.10 and Figure 5.11. The electron absorbed fraction data are taken from Table 5.1, Table 5.21 and Table 5.22. From Table 5.23, the maximum percentage difference is 17.8%, which occurs at 0.0485 MeV. From Table 5.24, the maximum percentage difference is 178%, which occurs at 0.0485 MeV. Also, between energies of 0.08 MeV and 3 MeV, the percentage differences are between 10% and 16%. Another comparison is made for the electron absorbed fractions obtained from Table 5.2, Table 5.21 and Table 5.22 to investigate the effect of changing both the model and the bottom radius size on electron absorbed fraction. These comparisons are presented in Tables 5.25 and Table 5.26. From Table 5.25, the differences due to changing the model and the radius size reach a maximum of 20.8% at 0.06 MeV. Also its is important to note that most of the differences in Table 5.25 are between 10% and 20% for all energies except the first two energies (0.0485 MeV and 0.05 Mev) and the last eight energies (from 0.7 MeV to 4 MeV) where the difference decreases to 2.26%.

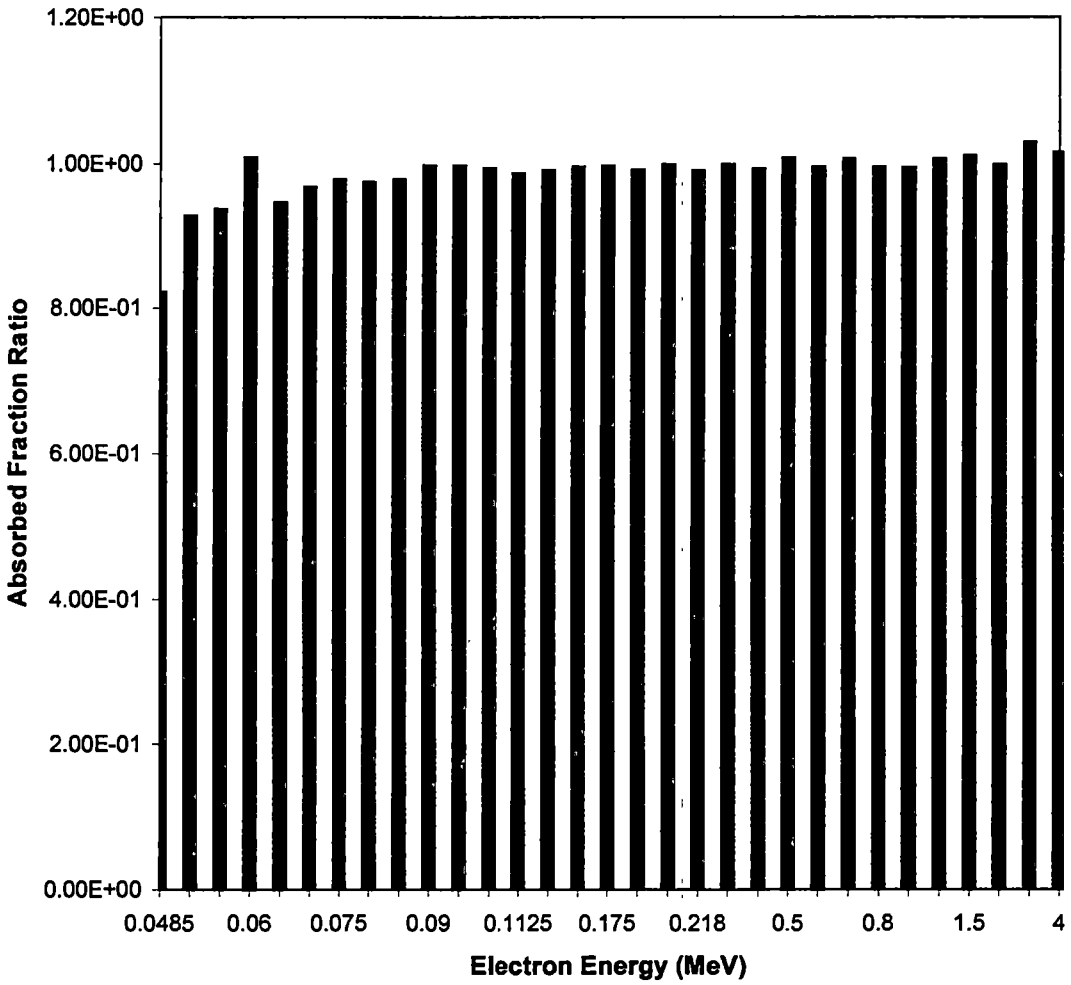


Figure 5.10 Electron absorbed fraction ratio for the truncated cone with bottom radius of 0.825 cm to the original truncated cone (bottom radius of 0.76394 cm).

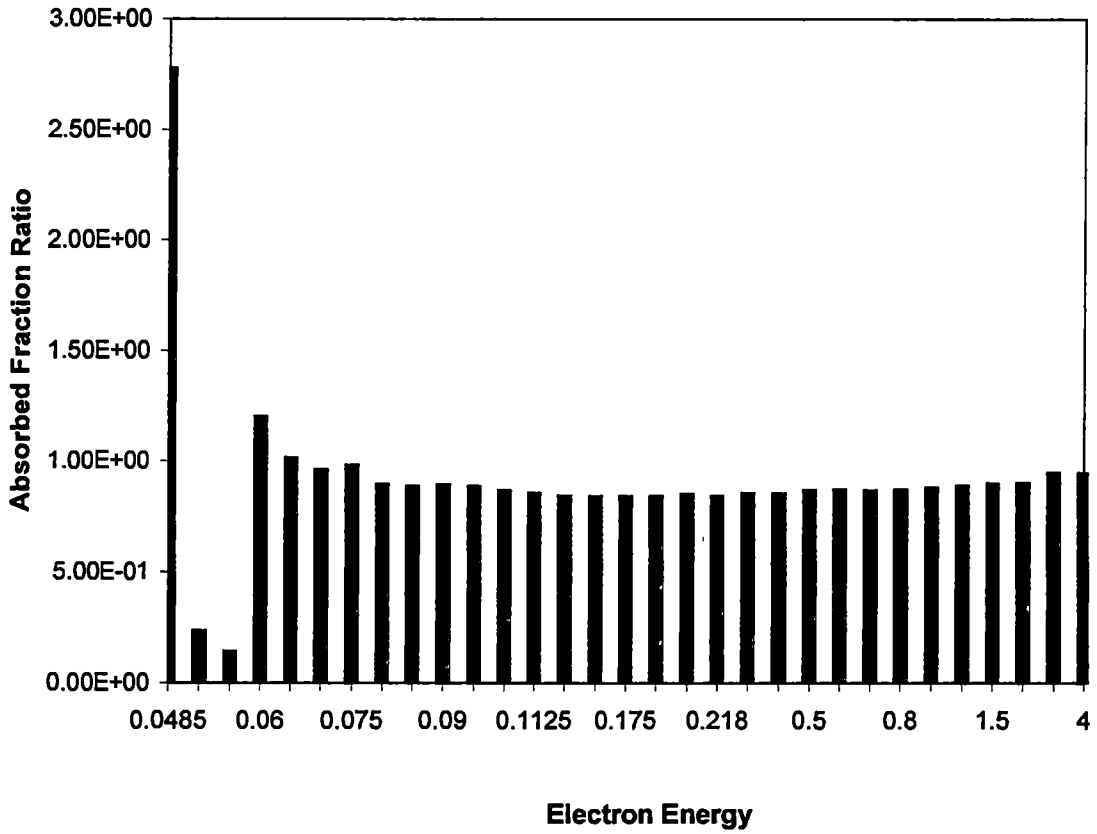


Figure 5.11 Electron absorbed fraction ratio for the truncated cone with bottom radius of 1.1077 cm to the original truncated cone (bottom radius of 0.76394 cm).

In Table 5.26, the differences due to changing the model and the radius size reach a maximum of 234% at 0.0485 MeV. Also, it is important to note that most of the differences is between 20% and 30% for energies between 0.08 MeV and 0.8 MeV. These differences decrease to 9.92% when the energy increases from 0.9 MeV to 4 MeV. Figure 5.12 illustrates the percentage differences taken from Tables 5.25 and 5.26.

5.10.3 Conclusion

The electron absorbed fractions for a 10 cm^2 inner surface truncated cone can still be used if the increase in the bottom radius is less then 45%. If the increase is more then 45% (large noses), we must modify the electron absorbed fractions to account for the increased nostril size.

5.10.4 8% and 45% decreases in the bottom radius (case 6)

The original input deck is used to create two new batches, each consisting of 31 input files. In each file, the cell and surface cards are modified so that the height of the new truncated cone corresponds to an inner surface area of 10 cm^2 given that the top radius is the same as the original truncated cone (0.3979 cm). The truncated cones have bottom radii of 0.7028 cm and 0.4202 cm respectively. The materials used are air and adult male soft tissue. The outputs of the MCNP4B runs are

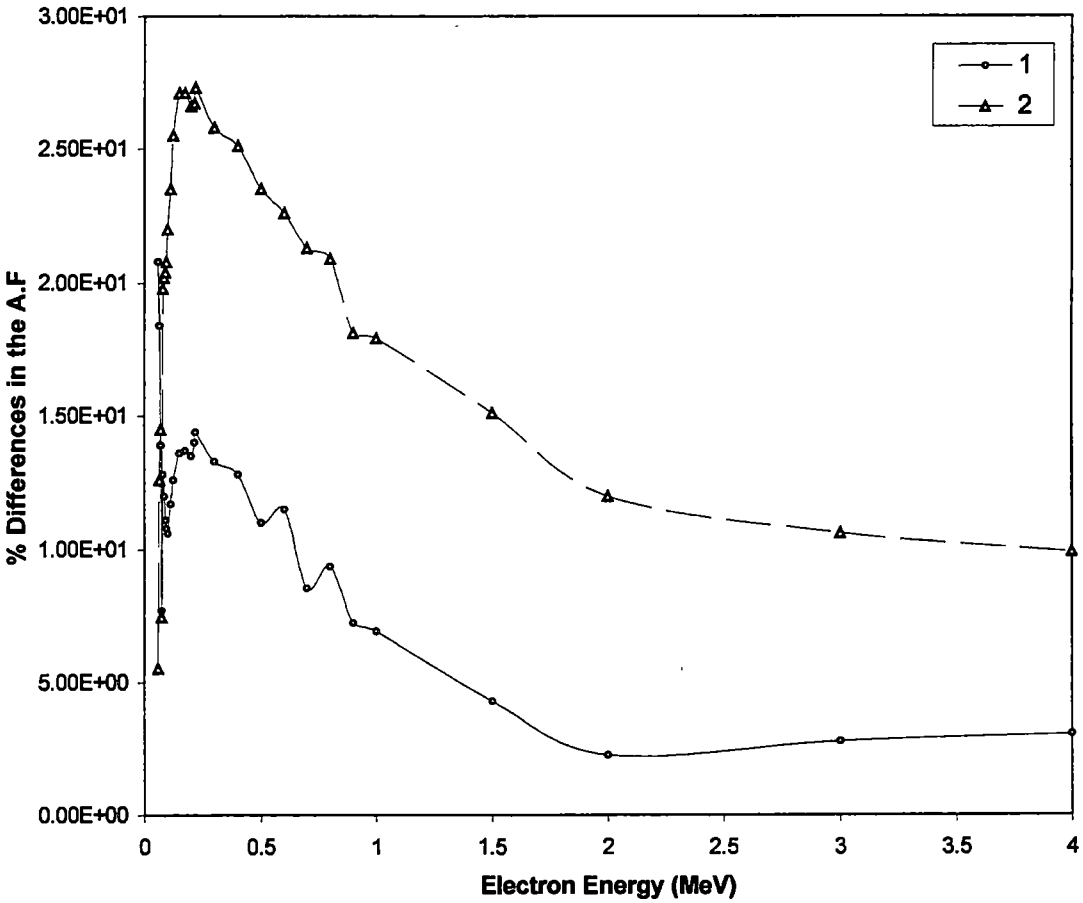


Figure 5.12 Percentage differences in the electron absorbed fractions listed in Tables 5.25 (1) and 5.26 (2).

summarized in Tables 5.27 and 5.28. Tables 5.29 and 5.30 are constructed from Tables 5.27, 5.28, and 5.1 for comparison. These Tables are found in Appendix C.

5.10.5 Comparison between case 6 and the original case

Plots of the electron absorbed fractions versus the electron initial energy are presented in Figure 5.13 and Figure 5.14. The electron absorbed fraction data are taken from Table 5.1, Table 5.27, and Table 5.28. From Table 5.29, the maximum percentage difference is 13.1%, which occurs at 0.0485 MeV. From Table 5.30, the maximum percentage difference is 17.6%, which occurs at 0.06 MeV. Also, as shown in Table 5.30, the percentage differences corresponding to energies of 0.08 MeV to 0.8 MeV are between 10% and 14%. However, in Table 5.29, the percentage differences corresponding to energies of 0.08 MeV to 0.8 MeV are between 1% and 5%. Another comparison is made for the electron absorbed fractions obtained from Tables 5.27 and 5.28 and from Table 5.2 to investigate the effect on electron absorbed fraction as a result of changing both, the model and the bottom radius size. These comparisons are given in Tables 5.31 and Table 5.32. From Table 5.31, the differences due to changing the model and the radius size reach a maximum of 19% at 0.06 MeV. Also, note that most of the differences in Table 5.31 are between 4% and 10% for nearly all energies. From Table 5.32, the differences due to changing the model and the radius size reach a maximum of 11.2% at 0.055 MeV. Also it is

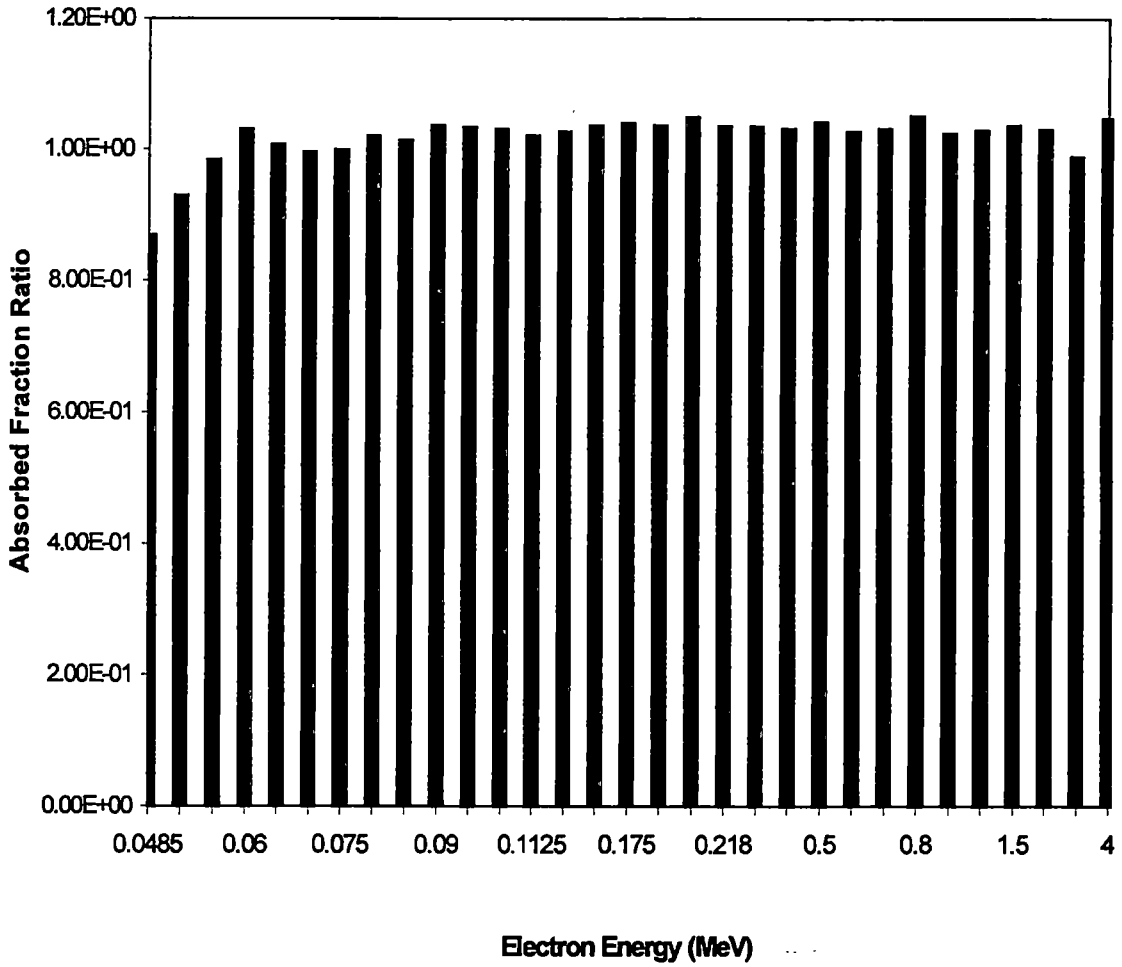


Figure 5.13 Electron absorbed fraction ratio for a truncated cone with bottom radius of 0.7028 cm to the original truncated cone (bottom radius of 0.76394 cm).

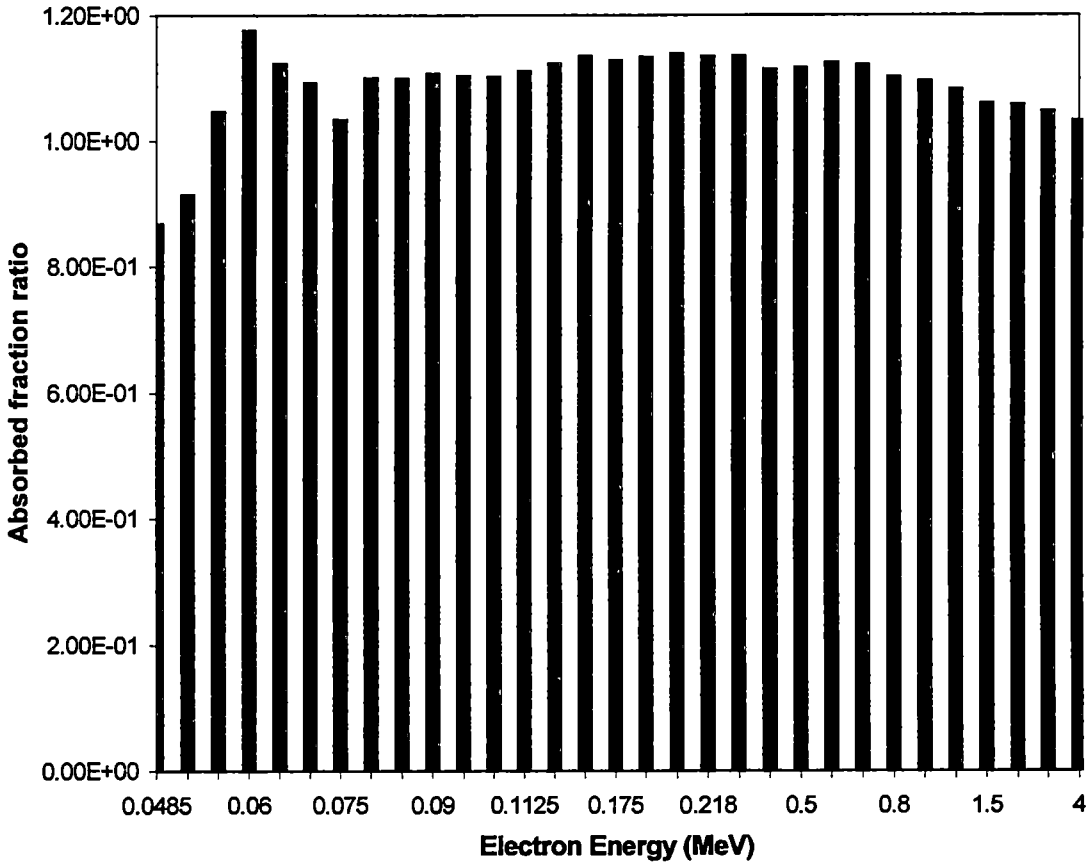


Figure 5.14 Electron absorbed fraction ratio for a truncated cone with bottom radius of 0.4202 cm to the original truncated cone (bottom radius of 0.76394 cm).

important to note that all differences are less than 7%. Figure 5.15 illustrates the percentage differences taken from Tables 5.31 and 5.32.

5.10.6 Conclusion

The electron absorbed fractions for the 10 cm^2 truncated cone inner surface area can be used if the decrease in the bottom radius is less than 8 %. If the decrease is more than 45 % (small nostril size), the nasal vestibule can be approximated by the cylinder model, which can be used if the top and bottom radii of the truncated cone are almost equal and the inner surface area is more than 10 cm^2.

5.11 Discussion and Conclusions

In this chapter we introduced a new model for the external human nose (ET_1). This new model is developed based on the fact that the real shape of the external nose is not cylindrical, but rather it is pyramidal and consists of two nasal vestibules. We demonstrated that a truncated cone is a suitable geometry for use in evaluating the dose (the electron absorbed fraction) to the basal cell region in the nasal vestibule. This was done by bounding the nasal vestibule (elliptical shape or truncated cone shape) by inner and outer truncated cones and calculating the energy deposition (the electron absorbed fraction) in the basal cell region for both bounded truncated cones. The results indicate that the electron absorbed fractions for the

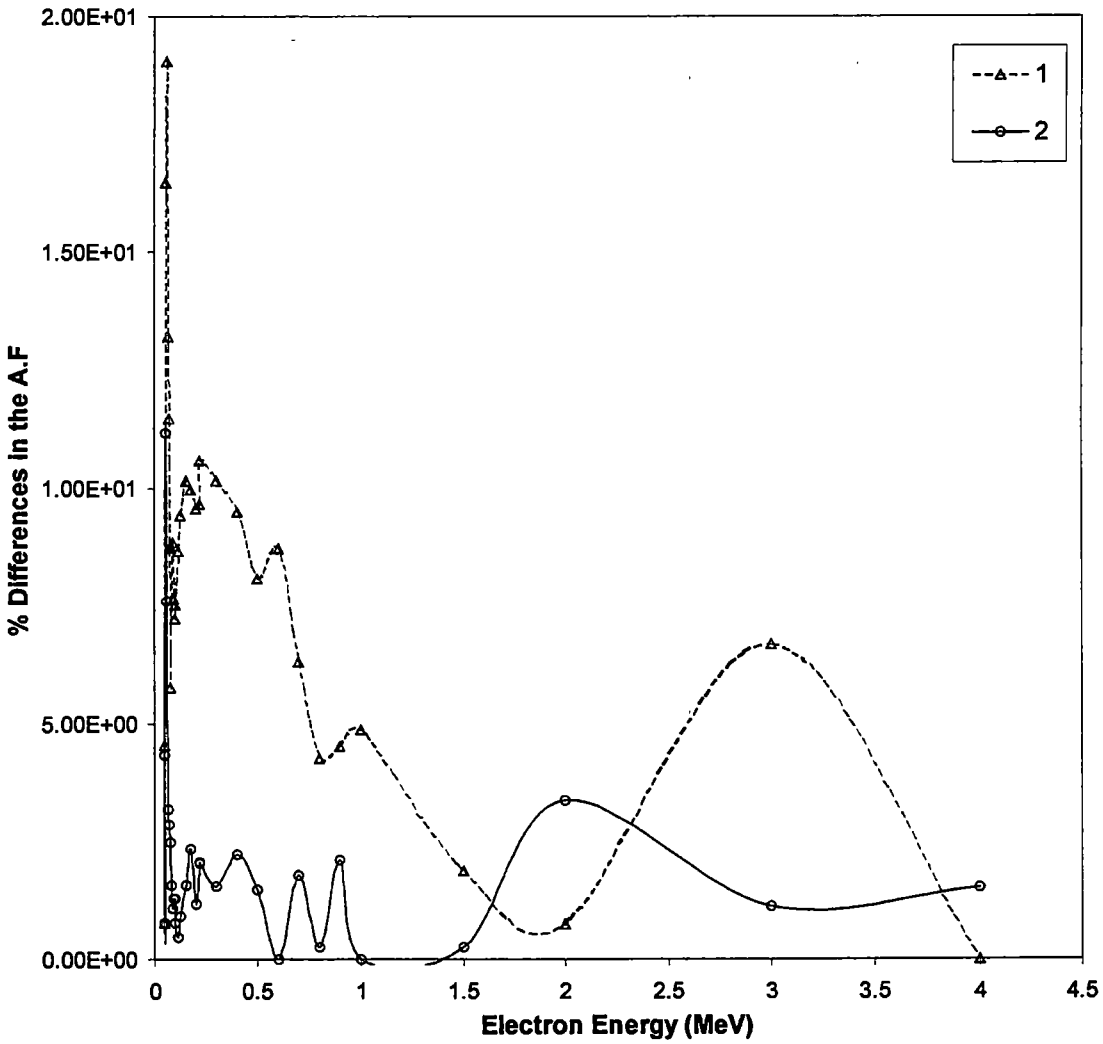


Figure 5.15 Percentage differences in the electron absorbed fractions obtained from Table 5.31 (1) and Table 5.32 (2).

assumed truncated cone model are bounded by the electron absorbed fractions in the basal cell region for both the inner and outer bounded truncated cones. Also a convergence experiment is done to ensure that our input decks are correct and that MCNP4B is reliable. This is done by creating four input decks, three of them for truncated cones and one for a cylinder. The bottom radii for the truncated cones are equal to the cylinder radius while the top truncated cone radii vary from 0.3979 cm to 0.6419 cm. The MCNP4B results showed that as the truncated cone's top radius increases, the electron absorbed fraction converges to the cylinder electron absorbed fraction. When comparison between the electron absorbed fractions obtained for truncated cone and cylinder is carried out, the maximum percentage difference is 21.4%. This occurs at energies between 0.06 MeV and 2.0 MeV. The percentage differences are between 9% and 15% when the electron energy is changed between 0.055 MeV and 0.7 MeV. Therefore, we conclude that changing the model will have some effect on the electron absorbed fraction values. Contrary to the cylinder results in Chapter 4, the electron absorbed fractions resulting from a source located on the upper and lower halves of the inner surface of the truncated cone model are not equal. The maximum percentage differences are 9.77% using the upper half source and 11% using the lower half. Therefore, we conclude that the electron absorbed fractions using a truncated cone model are dependent on the source location. Changing (increasing or decreasing) the surface area of the truncated cone model up to 45% dose not effect the values of the electron absorbed fractions. If the change is more

than 45%, the electron absorbed fraction values must be adjusted to account for the change in the surface area. Changing (increasing or decreasing) the bottom radius of the truncated cone by 45% does not effect the electron absorbed fractions values. However if the increases are more than 45% (large noses), then we must adjust the electron absorbed fraction to account for the increases in nostril size. Also if the decrease is more than 45% (small nostril size), we should use the cylinder model, if the top and bottom radii of the truncated cone are almost equal, and the inner surface area is more then 10 cm^2.

CHAPTER 6

The Effect of Dust Particle Size on Electron Absorbed Fraction

6.1 Introduction

Particle deposition in the respiratory tract, has been, and continues to be an intensive area of radiation research. Experimental data are available for Caucasian adult males, and for a specific range of particle sizes (from about 1 μm to 10 μm aerodynamic diameter) (ICRP 66, 1994). The aerodynamic diameter d_{ae} is the diameter (μm) of a unit density (1 g cm^{-3}) sphere that has the same terminal settling velocity in air or the particle interest. The radionuclides are carried in the air on dust particles and deposited on the inner surface of the nose. Therefore, when these radionuclides decay (electron or alpha decay), they lose some of their energy to the carrier (absorption in the dust particle) before entering the nose tissue. As a result, the electrons or alpha particles enter the nose tissue with less energy and consequently deposit less energy in the target (basal cells). Absorption in dust particles was not considered at all in ICRP Publication 66. In this chapter we describe a Matlab® program developed to calculate the energy deposition from electrons inside spherical dust particles. In the program, the dust particle radii range

from 0.5 μm to 50 μm. The electrons are uniformly generated anywhere within the volume of the dust particle. Therefore the distance traveled by the electron can range from zero up to the diameter of the dust particle. The number of source electrons followed is 100,000. The electron absorbed fraction is estimated based on the energy spectrum. For comparison, the electron absorbed fraction in ET_1 obtained using a 5 μm dust particle radius with the electron generated in the center, and the output from the Matlab® program is made. The electron is assumed to travel in a straight line to the surface.

6.2 Dust Particle Composition

In this program the soil composition, taken from the Federal guidance report, is used for the environmental dust particle composition (FGR No 12, 1993). The density is $3 g/cm^3$, and the element mass fraction is shown in Table 6.1.

Table 6.1 The element mass fraction for the soil composition used for the environmental dust particle.

H	C	O	Al	Si	K	Ca	Fe
0.021	0.016	0.577	0.050	0.271	0.013	0.041	0.011

6.3 Dust Particle Range and Stopping Power

Ranges and stopping powers for the elements in Table 6.1 (H, C, O, Al, Si, K, Ca, and Fe) are obtained from the Internet (http://physics.nist.gov/cgi-bin/Star/e_table.pl). A program using Matlab® software is created to calculate the range and the stopping power for electrons with energies between 0.04745 MeV and 4 MeV, traveling in the dust particle. The element mass fraction from Table 6.1 and the stopping power and ranges for each element are used. The range calculation is carried out using

$$R_i = \frac{1}{\rho}\sum_j R_j f_j \qquad 6.1$$

where f_j is the mass fraction of the j^{th} element and R_j is the continuous slowing down approximation range (CSDA) for the j^{th} element and ρ is the density ($3 gcm^{-3}$). Similarly, the stopping power is calculated using

$$\left(\frac{dE}{dx}\right)_i = \frac{1}{\rho}\sum_{j=1}^{n}\left(\frac{dE}{dx}\right)_j f_j \qquad 6.2$$

where $\left(\frac{dE}{dx}\right)_i$ is the stopping power of electron with energy i in the dust particle in MeV/cm. $\left(\frac{dE}{dx}\right)_j$ is the stopping power for j^{th} element. Appendix D displays a listing of the program and its output (Table 6.2).

6.4 Distance the Electron Will Travel Inside The Dust Particle

The average distance the electron travels inside a spherical dust particle to reach the surface (boundary) can be calculated using the following probability density function (Eckerman, 1986)

$$f(x) = \frac{3}{2d}\left[1 - \left(\frac{x}{d}\right)^2\right] \qquad 6.3$$

where d is the dust particle diameter, x is the distance the electron travels inside the dust particle from its origin to the surface (dust particle boundary). The average distance is expressed by

$$\bar{x} = \frac{\int_0^d f(x)x\,dx}{\int_0^d f(x)\,dx} = \frac{3}{8}d \qquad 6.4$$

Also, one can use the Monte Carlo method to calculate the distance the electron travels inside the dust particle by using the following arguments:

- Given an electron source distributed uniformly in a spherical volume, the radius r from which the electron (history) starts can be described using a spatial probability density function (Lewis, 1993)

$$f(r)dr = \frac{dv}{dr} \qquad 6.5$$

where v is the volume of the sphere $v = \frac{4}{3}\pi R^3$ and R is the sphere radius. Then

$$dv = d\left(\frac{4}{3}\pi r^3\right)dr = 4\pi r^2 dr \Rightarrow f(r)dr = \frac{4\pi r^2 dr}{\frac{4}{3}\pi R^3} = \frac{3r^2}{R^3}dr = dF(r) \Rightarrow$$

$$F(r) = \left(\frac{r^3}{R^3}\right) = \left(\frac{r}{R}\right)^3 \qquad 6.6$$

where F(r) is the cumulative probability density.

- Given the sphere radius, we can determine the distance between the sphere center and the point where the electron in generated (born) using

$$\xi = F(r) = \left(\frac{r}{R}\right)^3 \Rightarrow and \quad r = R\xi^{\frac{1}{3}} \qquad 6.7$$

where ξ is a random number between 0 and 1 ($0<\xi<1$).

- In a spherical geometry, the distance an electron travels from its origin is a function of the following:

1. R, the distance from the point where the electron is born to the center of the sphere.
2. μ, which is the direction cosine of $\overline{\Omega}$ with respect to the radial direction of r.

Assume that the electron moves a distance S in a straight line from its origin to the sphere in a (see Figure 6.1).

From the Figure, the sphere radius (R) and the distance S can be expressed as:

$$R^2 = (r + S\cos x)^2 + (S\sin x)^2 \Rightarrow S^2 + 2rS\cos x + r^2 - R^2 = 0 \qquad 6.8$$

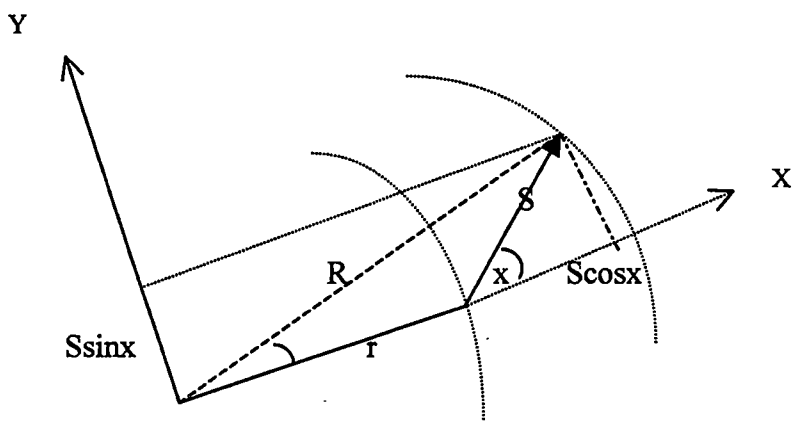


Figure 6.1 The birth of an electron in spherical volume and the distance it will travel to the surface.

The solution for equation 6.8 (detailed solution in Appendix D) is

$$S = R\left[\left(1+4\xi^{\frac{2}{3}}g^2-4\xi^{\frac{2}{3}}g\right)^{\frac{1}{2}}-2g\xi^{\frac{1}{3}}-\xi^{\frac{1}{3}}\right] \qquad 6.9$$

where:

ξ is a random number that can take any value between zero and one, (this random number represents for radial distance); g is another random number for the direction cosine , it also can take any value between zero and one ($g=\frac{\mu+1}{2}$); and μ=cosx.

S is the distance the generated particle will travel (in a straight line) from its origin to the boundary (dust particle surface)

6.5 Number of Histories Experiment

The number of histories used to obtain the electron spectrum emerging from dust particles with different sizes has to satisfy two conditions:

1. The random number must take values between zero and one. Since we want to optimize the time required to run this program, we should not use more histories than needed.

2. The average distance the electron travels obtained from equation 6.9 must approach the average distance the electron travels by using equation 6.4, the analytical solution.

To satisfy the first condition, a small program is written using Matlab® software to generate a random number between zero and one, with 100, 1000, 10000 and 100,000 histories. The results are plotted in Figures 6.2-6.5. By comparing these four Figures, we conclude that 100,000 histories is a suitable number to be used for this problem.

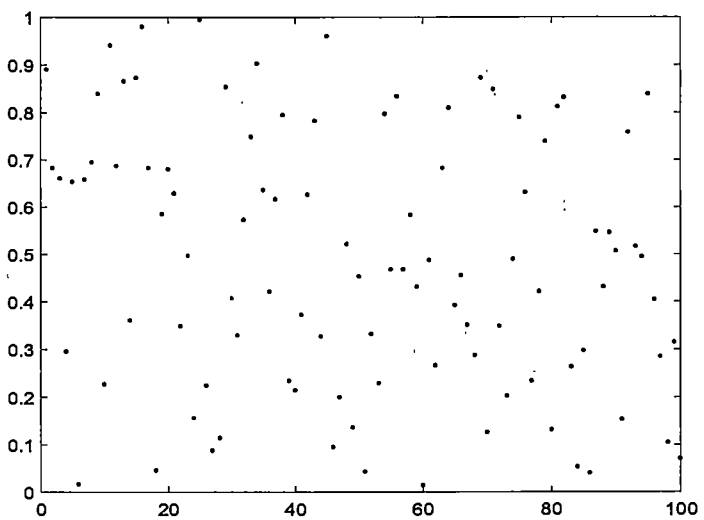


Figure 6.2 100 random numbers generated.

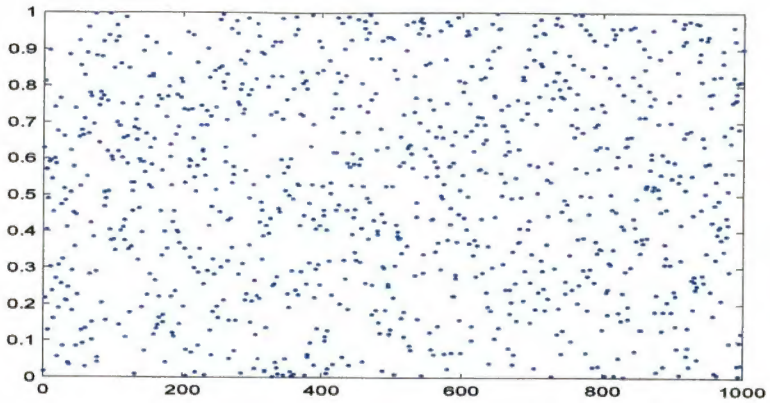


Figure 6.3 1000 random numbers generated.

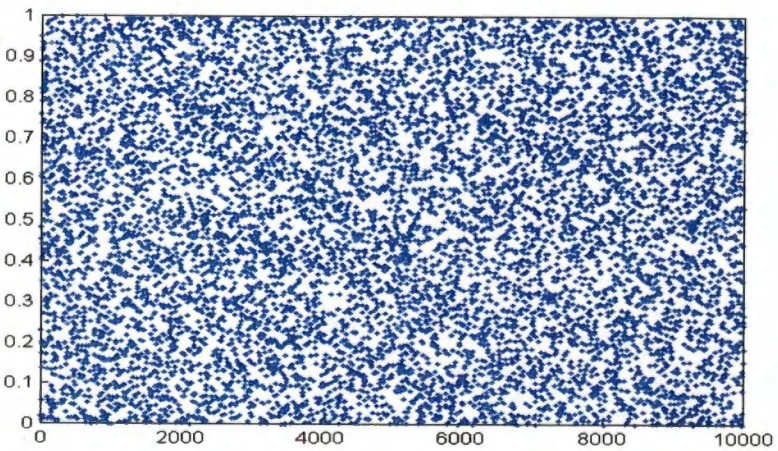


Figure 6.4 10,000 random numbers generated.

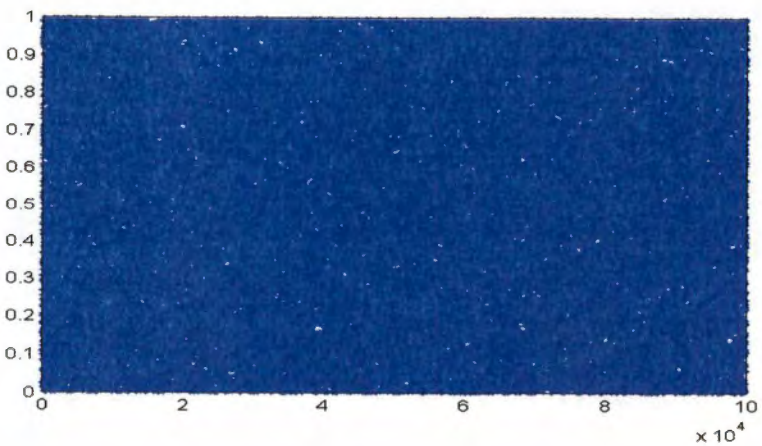


Figure 6.5 100,000 random numbers generated.

6.6 Comparing the Average Distance Obtained From Equation 6.4 to 6.9.

To satisfy the second condition, a program is written using Matlab® software to calculate the average distance the electron travels inside the dust particle, using equations 6.4 and 6.9, with 100, 1000, 10000 and 100,000 histories. The results are tabulated in Tables 6.3-6.6 in Appendix D, and plotted in Figures 6.6-6.9.

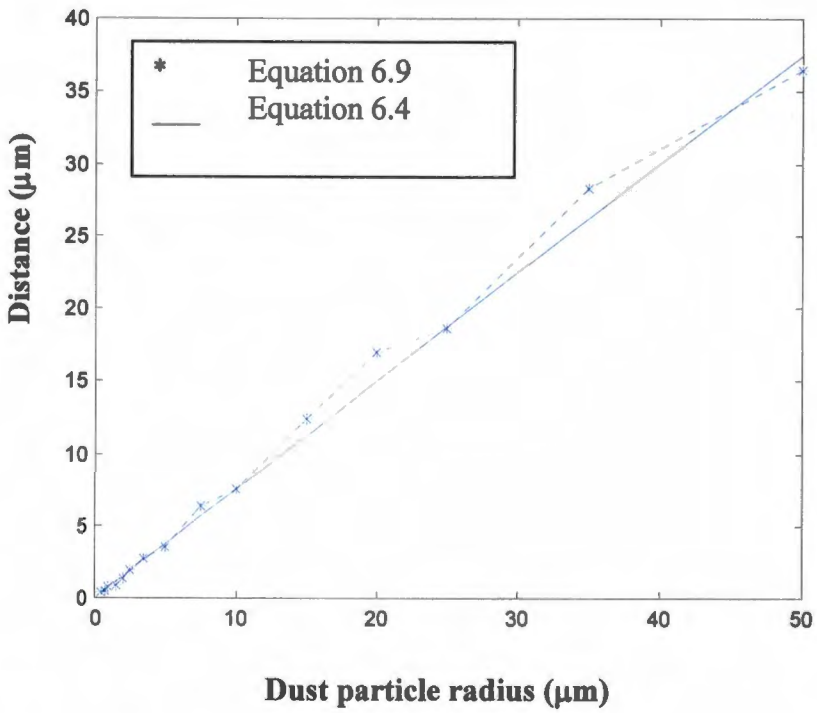


Figure 6.6 Average distance traveled by an electron using equations 6.4 and 6.9 (100 histories are used)

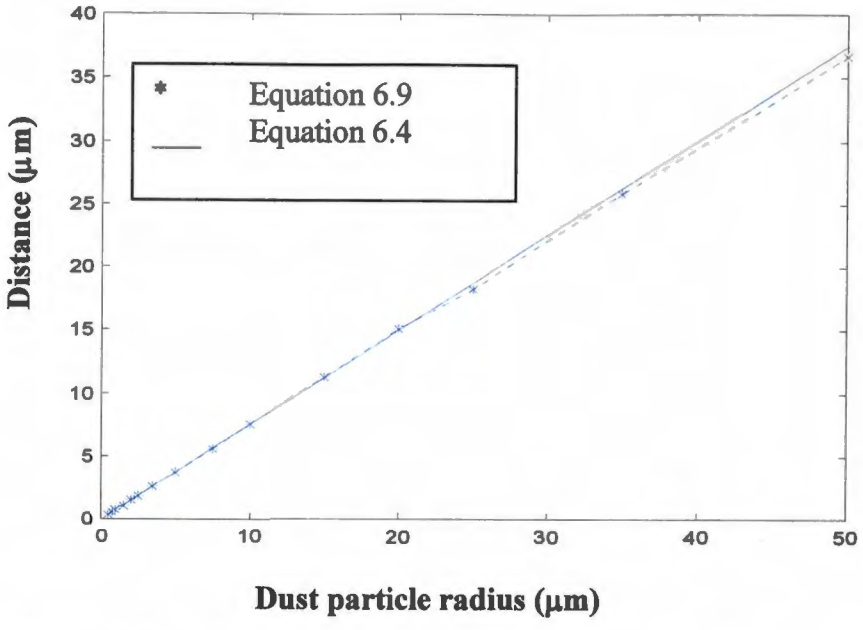


Figure 6.7 Average distance traveled by an electron using equations 6.4 and 6.9 (1000 histories are used)

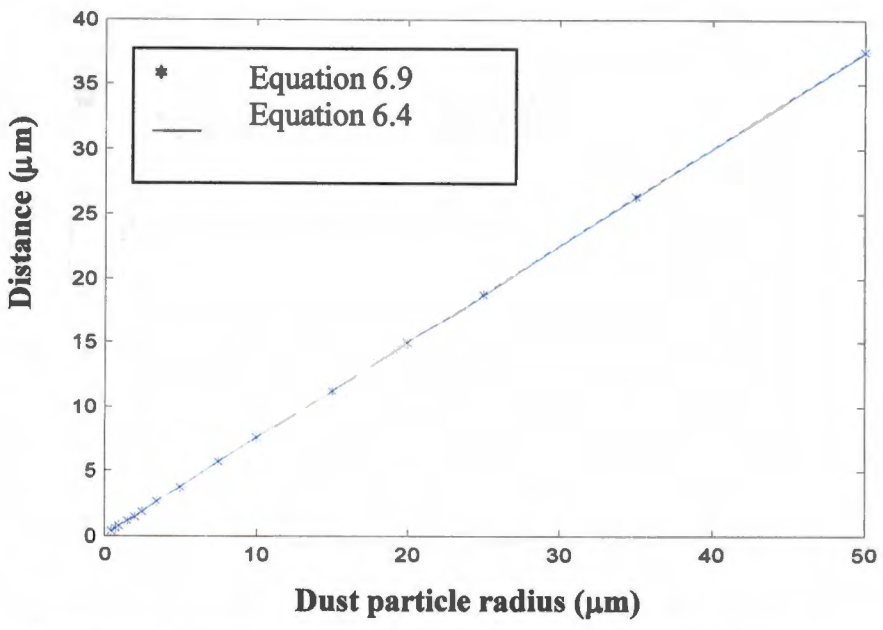


Figure 6.8 Average distance traveled by an electron using equations 6.4 and 6.9 (10,000 histories are used)

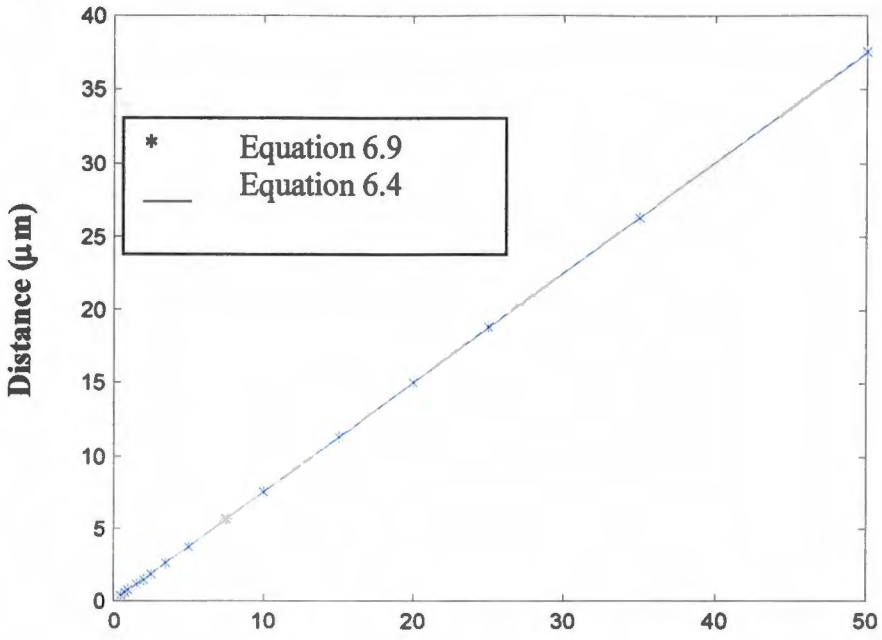


Figure 6.9 Average distance traveled by an electron using equations 6.4 and 6.9 (100,000 histories are used)

6.7 Program Details.

Two random numbers are chosen (between 0 and 1) and used to solve equation 6.9 for S. The distance (S) and the particle energy (E) are used to obtain the energy lost by the electron in the dust particle by interpolation of the energy and the stopping power. The energy lost is subtracted from the initial energy and the remaining energy (the particle energy when it emerges from the dust particle) is put in energy bins. If the particle energy less than 0.5 MeV, the energy bins (10 bins) are chosen to cover the range from 0.0478 MeV to (E-0.0478). If the particle energy (E) is greater than or equal to 0.5 MeV, the energy bins (10 bins) are chosen to cover the range from 0.0478 MeV to E. The electron absorbed fraction is calculated for each

particle using the particle energy when it emerges from the dust particle (see Appendix D). This is done by linear interpolation using the electron absorbed fraction data given in the program input (from the ICRP 66 for cylinder model). The average electron absorbed fraction is estimated by summing all the electron absorbed fractions divided by the number of histories used (100,000 histories) according to

$$\overline{AF} = \frac{\sum_{i=1}^{n} y_i E_i AF_i}{\sum_{i=1}^{n} y_i E_i} \qquad 6.10$$

where y_i is a fraction represent the number of electron emerging from the dust particle with energy E_i normalized to the number of history used (i.e., 100,000). AF_i is the absorbed fraction corresponding to energy E_i.

6.8 Calculations and Results

Fifteen spherical dust particles are used with diameters of 1, 1.5, 2, 3, 4, 5, 7, 10, 15, 20, 30, 40, 50, 70, and 100 microns. Twenty one energies are used (0.0485, 0.05, 0.06, 0.07, 0.08, 0.09, 0.1, 0.15, 0.20, 0.30, 0.40, 0.50, 0.60, 0.70, 0.80, 0.90, 1.0, 1.5, 2.0, 3.0, and 4.0 MeV). 100,000 particle histories for each energy are created inside each spherical dust particle. The computer program and its output (Tables 6.6-6.35) are found in Appendix D. Sample outputs of the program runs are plotted in Figure 6.10 for five dust particle sizes (radii of 1 μm, 2.5 μm, 7.5 μm, 20 μm and 50 μm) along with the original electron absorbed fractions taken from ICRP 66.

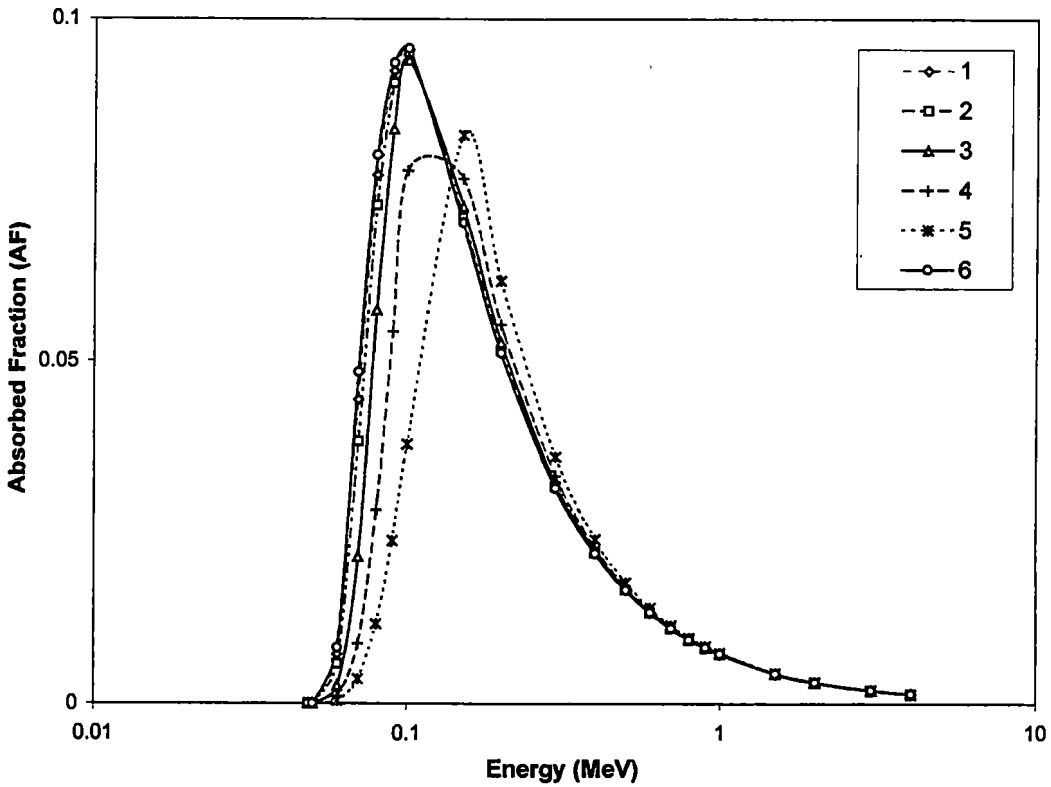


Figure 6.10 Electron absorbed fraction vs. energy (MeV) for dust particle radii of (1) 1 μm, (2)2.5 μm, (3) 7.5 μm, (4) 20 μm, (5) 50 μm , and (6) for absorbed fractions obtained from ICRP 66 (no self-absorption).

6.8.1 Discussion

To investigate the effect of particle sizes on the electron absorbed fractions we plotted histograms of electron absorbed fractions results. Figures 6.11-6.13 display electron absorbed fractions obtained using small particle sizes (radii of 1.5, 2 and 2.5 μm). Figures 6.14-6.16 display electron absorbed fractions obtained using intermediate particle sizes (radii of 10,15 and 20 μm). Figures 6.17-6.19 display electron absorbed fractions obtained using large particle sizes (radii of 25, 35 and 50 μm).

Histograms in all Figures indicate that effects on the electron absorbed fractions vary with electron energies and the particle radii. For most energies, the electron absorbed fractions are decreased due to self-absorption in the dust particle. Sometimes, however, the electron absorbed fractions are increased due to the presence of the dust particle. For small particle size, the effect is obvious for energy ranges from 0.07 to 0.1 MeV. Increasing the particle size in this group (small particle size), increases the effect in this energy range (the electron absorbed fraction decreases). The opposite effect can be observed above 0.1 MeV. In general, the electron absorbed fraction *(AF)* decreases for lower energies (below 0.1 MeV) and increases slightly above this energy.

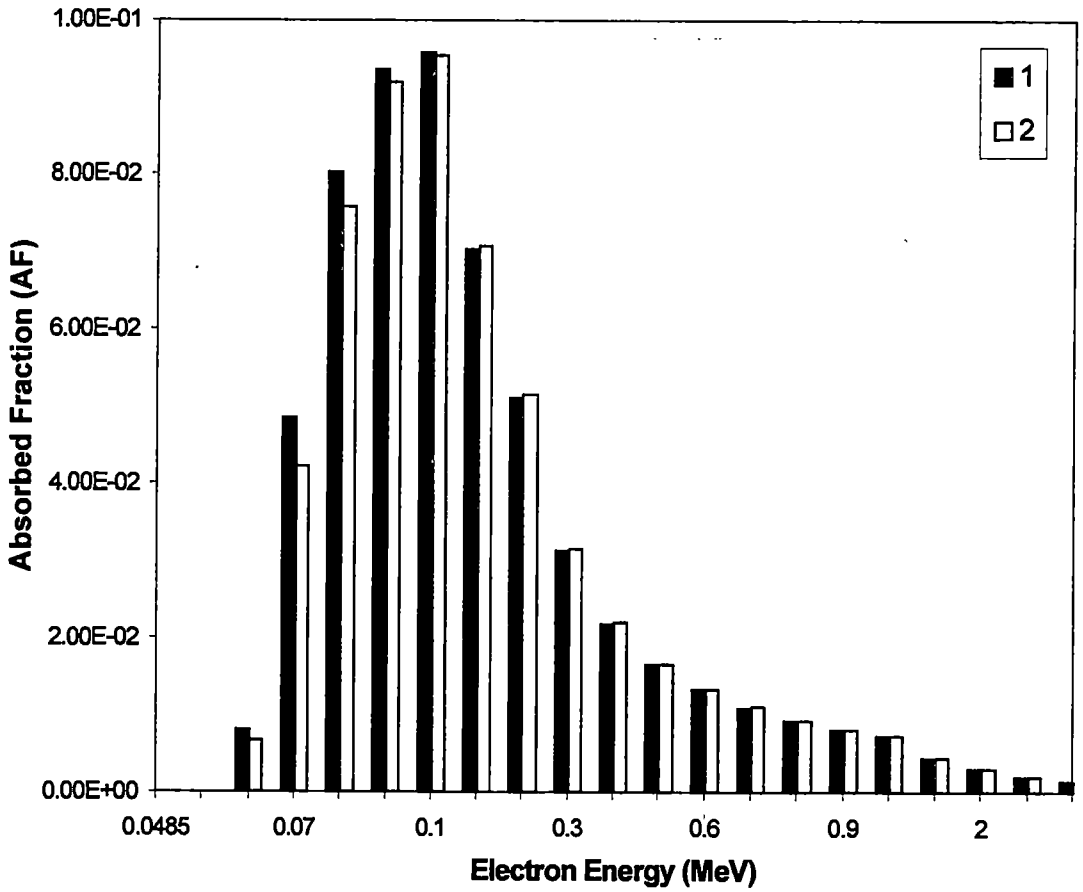


Figure 6.11 Histogram of electron absorbed fraction vs. energy (MeV). (1) values are displayed from ICRP 66 (no self-absorption) and (2) with the effect of self-absorption in a 1.5 μm particle radius (small dust particle size).

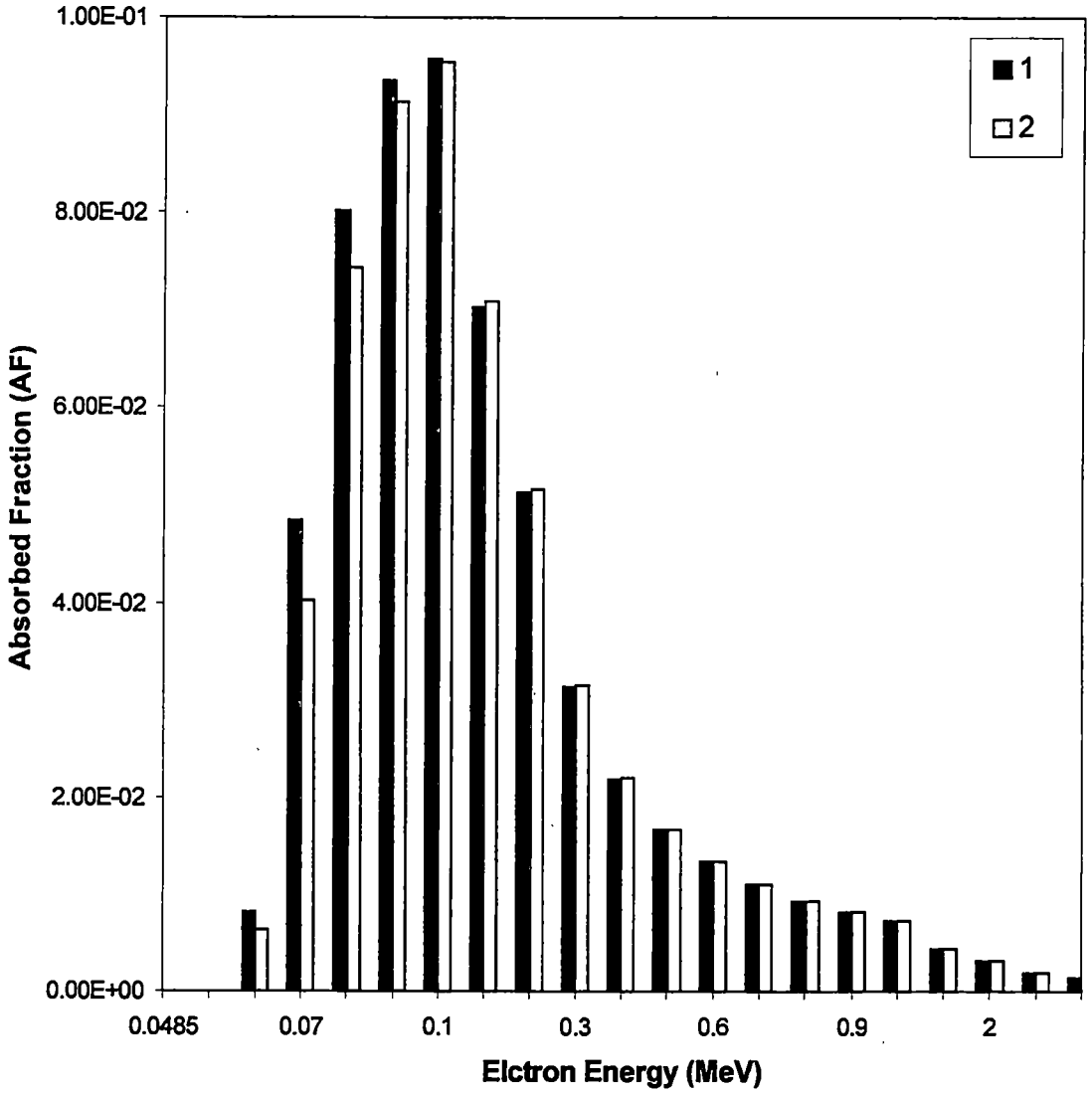


Figure 6.12 Histogram of electron absorbed fraction vs. energy (MeV). (1) values are displayed from ICRP 66 (no self-absorption) and (2) with the effect of self-absorption in a 2 μm particle radius (small dust particle size).

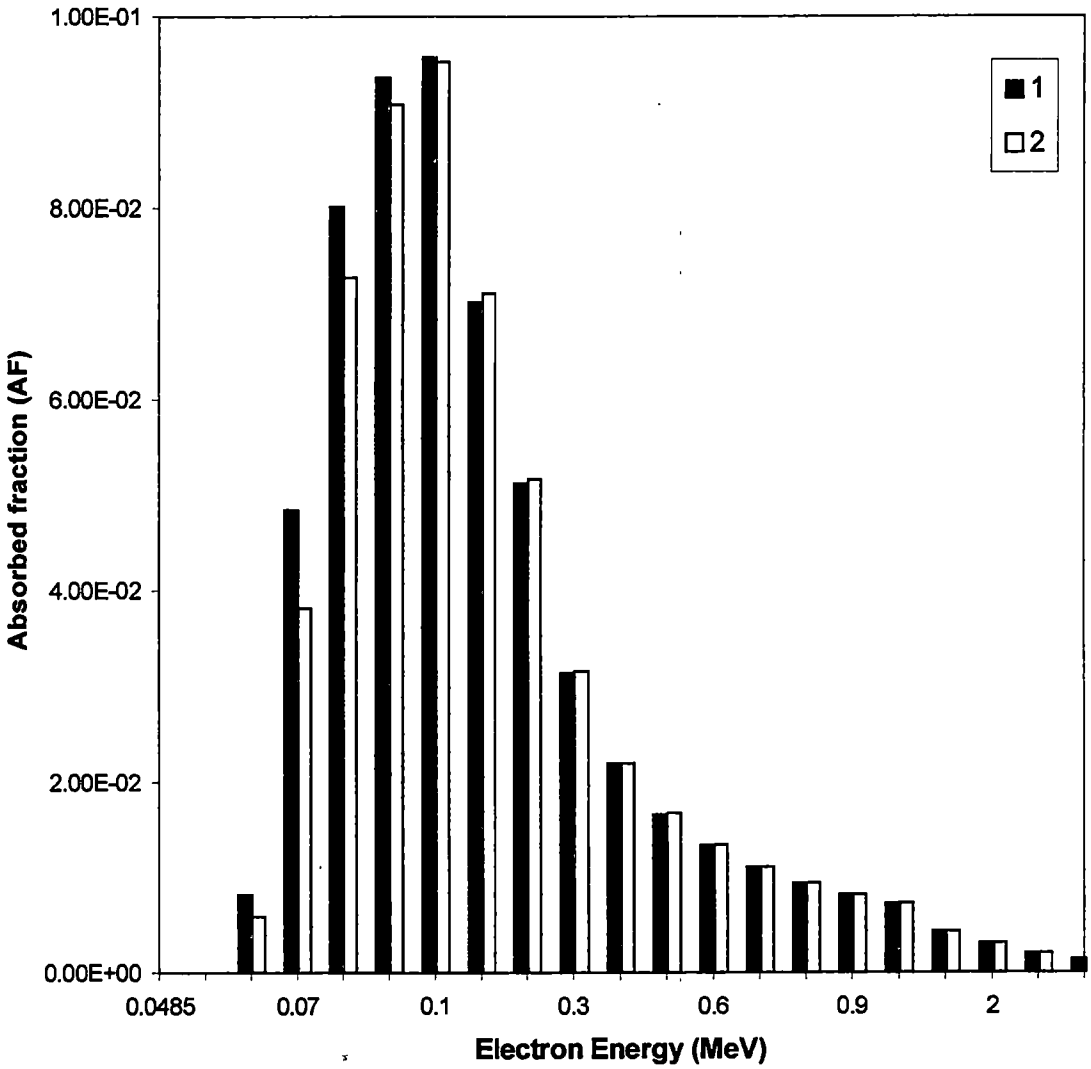


Figure 6.13 Histogram of electron absorbed fraction vs. energy (MeV). (1) values are displayed from ICRP 66 (no self-absorption) and (2) with the effect of self-absorption in a 2.5 μm particle radius (small dust particle size).

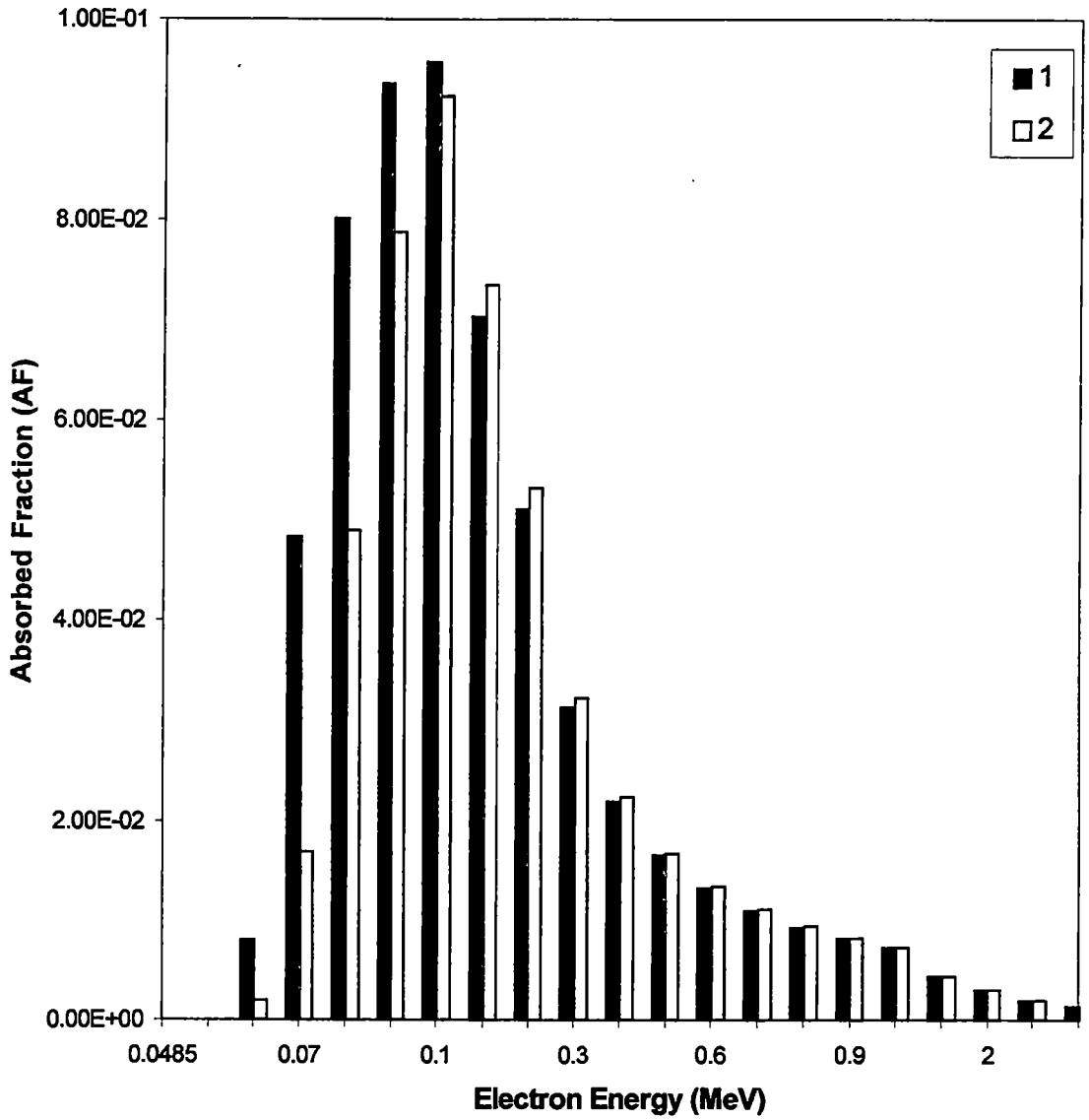


Figure 6.14 Histogram of electron absorbed fraction v. energy (MeV). (1) values are displayed from ICRP 66 (no self-absorption) and (2) with the effect of self-absorption in a 10 μm particle radius (intermediate dust particle size).

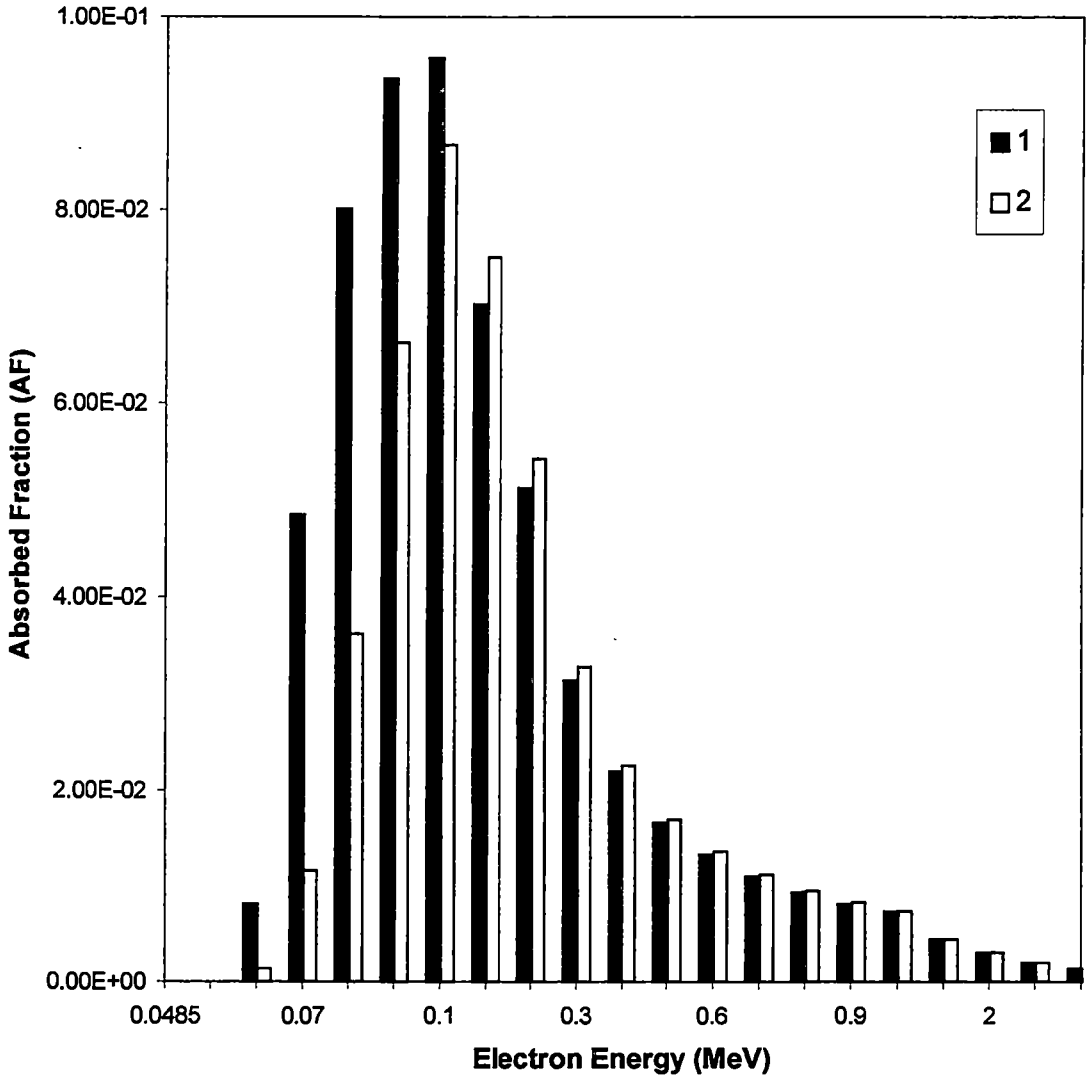


Figure 6.15 Histogram of electron absorbed fraction vs. energy (MeV). (1) values are displayed from ICRP 66 (no self-absorption) and (2) with the effect of self-absorption in a 15 μm particle radius (intermediate dust particle size).

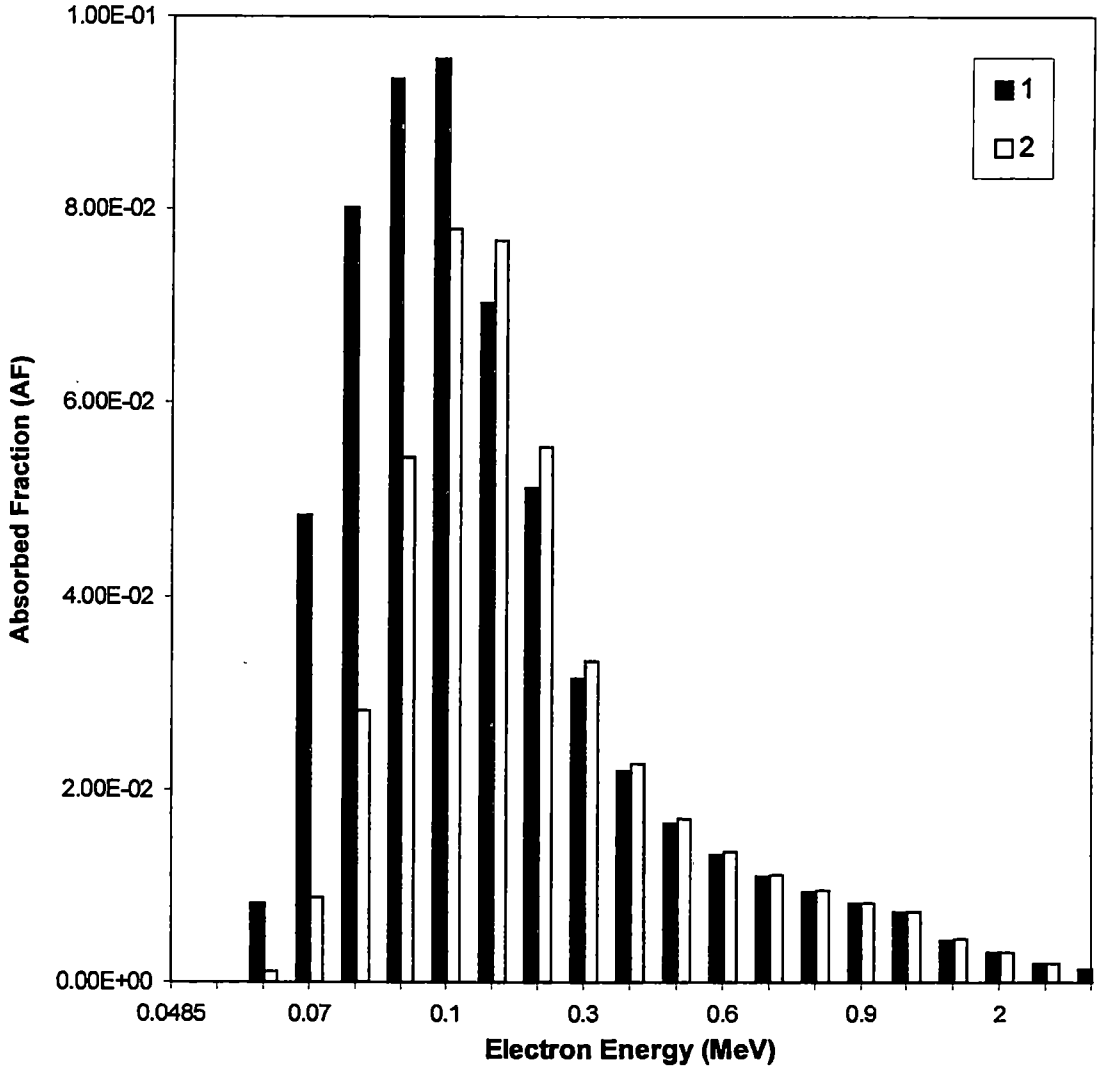


Figure 6.16 Histogram of electron absorbed fraction vs. energy (MeV). (1) values are displayed from ICRP 66 (no self-absorption) and (2) with the effect of self-absorption in a 20 μm particle radius (intermediate dust particle size).

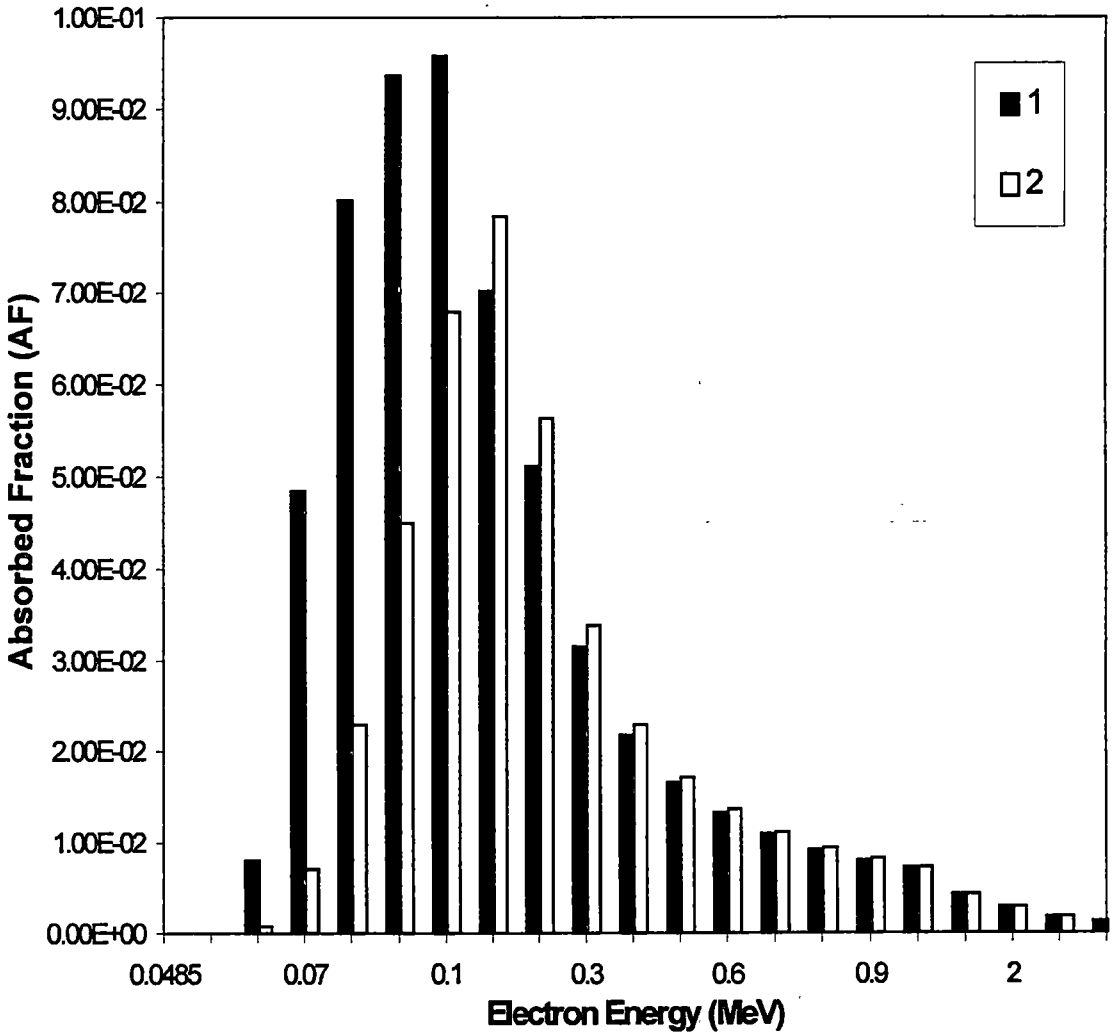


Figure 6.17 Histogram of electron absorbed fractions vs. energy (MeV). (1) values are displayed from ICRP 66 (no self-absorption) and (2) with the effect of self-absorption in a 25 μm dust radius (large dust particle size).

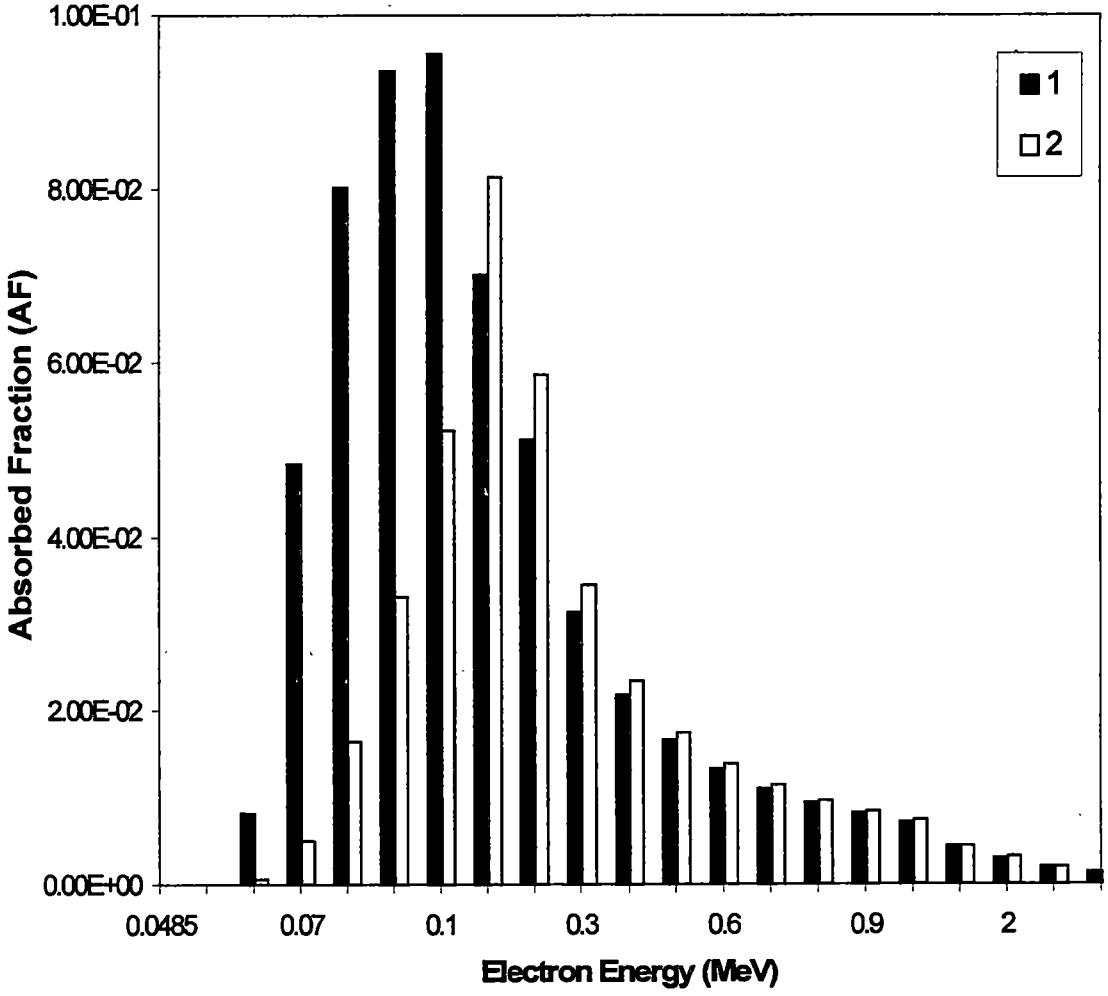


Figure 6.18 Histogram of electron absorbed fraction vs. energy (MeV). (1) values displayed from ICRP 66 (no self-absorption) and (2) with the effect of self-absorption in a 35 μm particle radius (large dust particle size).

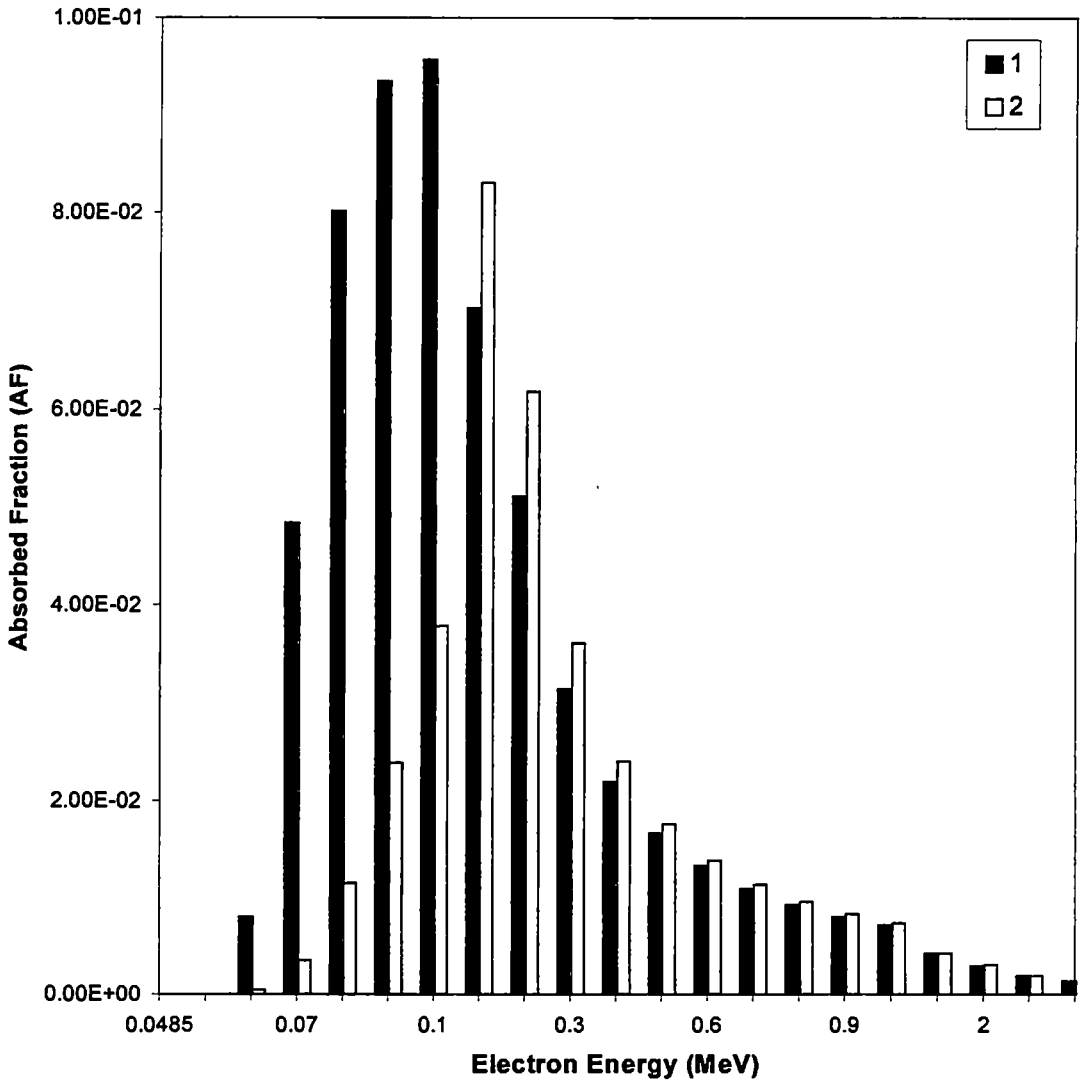


Figure 6.19 Histogram of electron absorbed fraction vs. energy (MeV). (1) values are displayed from ICRP 66 (no self-absorption) and (2) with the effect of self-absorption in a 50 μm dust radius (large dust particle size).

6.9 Program Validation

To ensure that the Matlab® program we created to estimate the electron absorbed fraction in the basal cells gives correct and reliable results for electrons generated anywhere inside various dust particle sizes, we ran the original Matlab® program using the truncated cone model. The results are tabulated in Appendix D (only the electron absorbed fractions are tabulated since the electron fractions in the bins are the same as for the cylinder model). Also, we estimate the electron absorbed fraction to the same target using equation 6.4. Equation 6.4 gives the average distance traveled by an electron in the spherical dust particle as $\frac{3}{8}d$, (where d is the particle diameter). We also ran this program using the real radii of the spheres. The results are tabulated in Tables 6.51-6.54 in Appendix D (these Tables are only for spherical dust particles having radii of 2.5 μm, 5 μm, 20 μm, and 50 μm).

6.9.1 Results

Plots of the electron absorbed fractions versus the electron initial energy are presented in Figures 6.20 through 6.23 for dust particles with radii of 2.5 μm to 50 μm. Two of the plots represent the electron absorbed fractions using cylinder and truncated cone models without self-absorption in the dust particles. The remaining plots present the electron absorbed fractions using the truncated cone model with self-absorption.

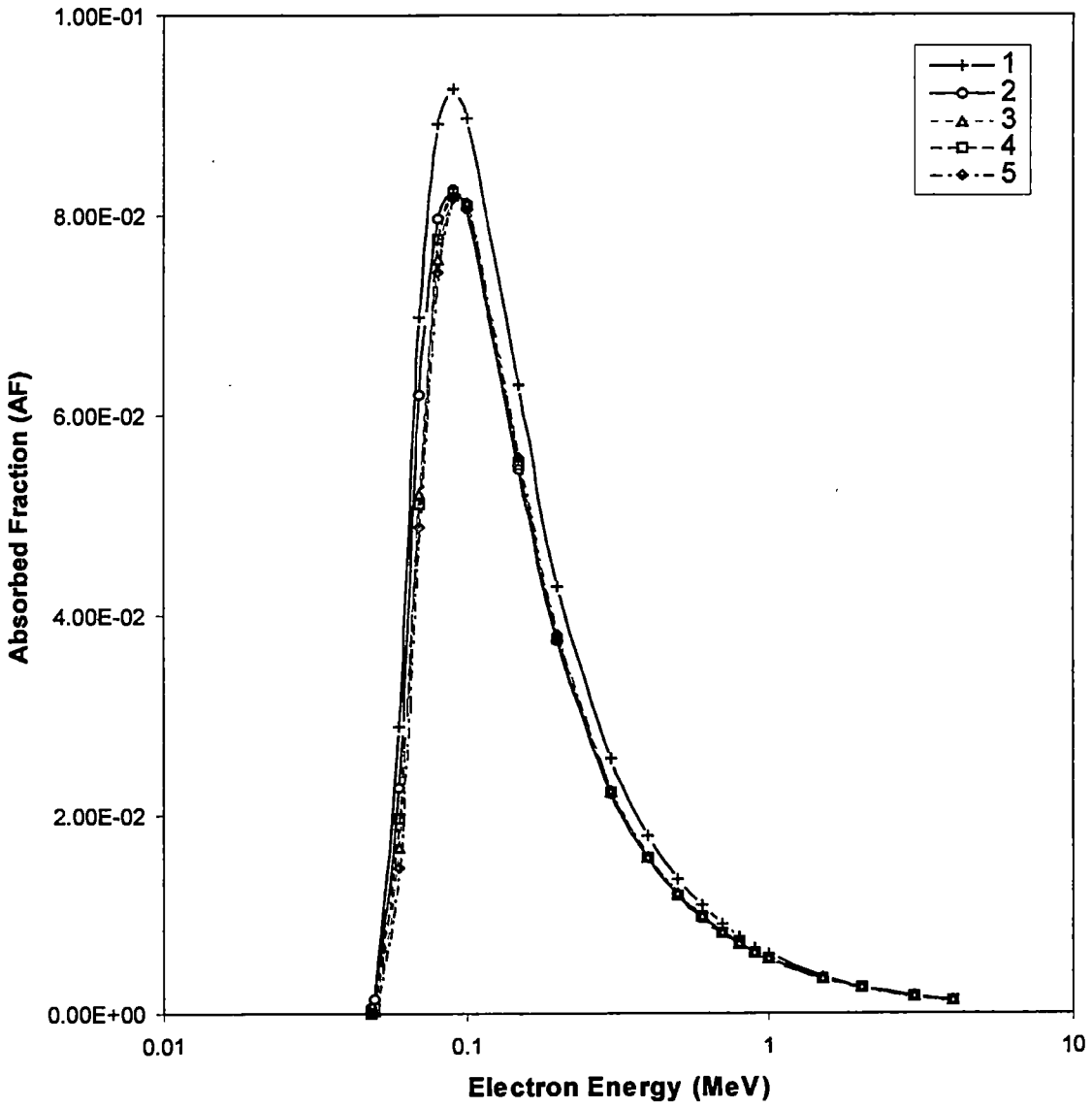


Figure 6.20 Electron absorbed fraction vs. energy (MeV) using (1) cylinder with no-self absorption, (2) truncated cone with no self-absorption, (3) truncated cone with self absorption (monte carlo program), (4) truncated cone with self-absorption (equation 6.4), and (5) truncated cone with self-absorption (actual radius 2.5 μm).

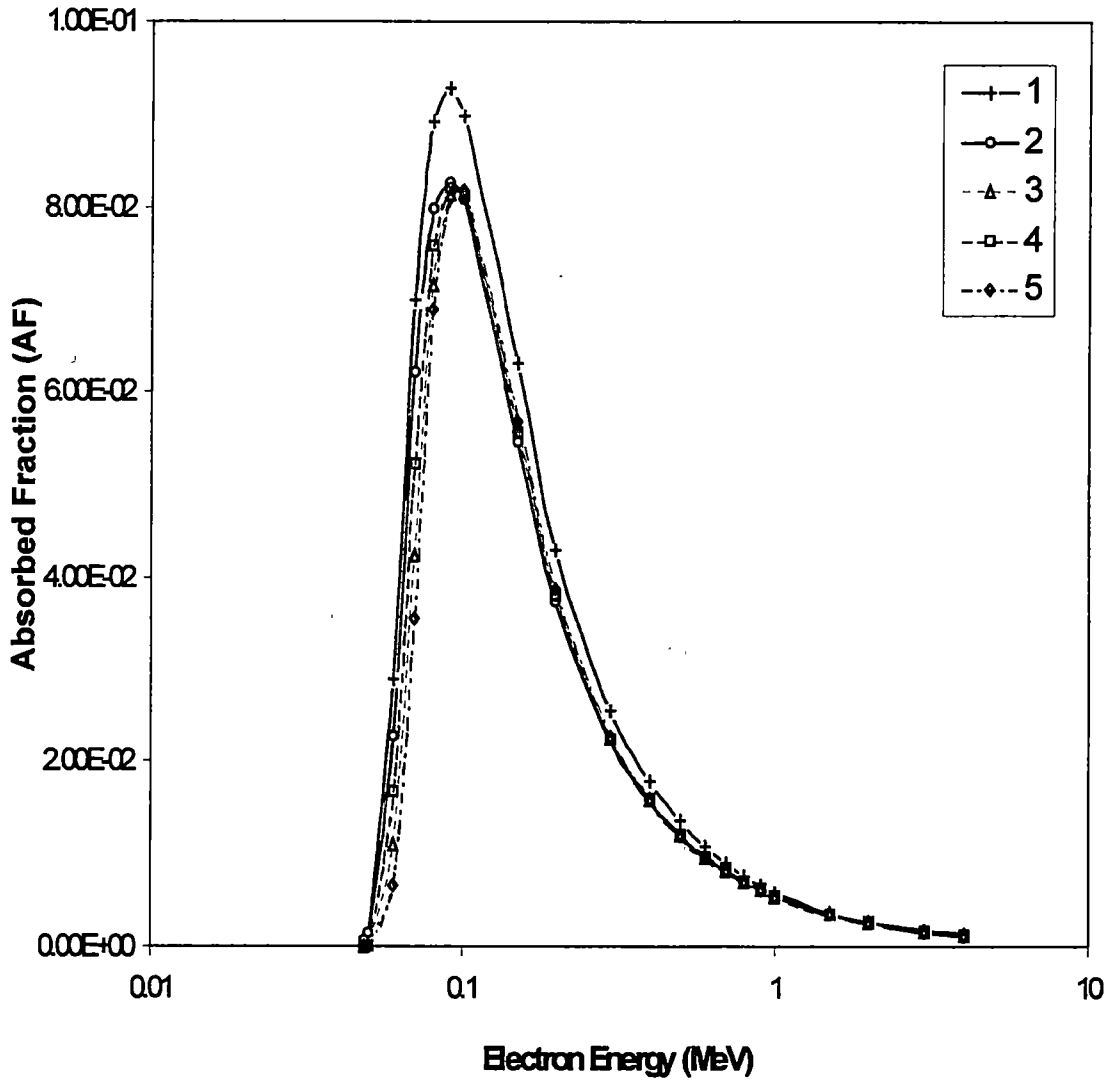


Figure 6.21 Electron absorbed fraction vs. energy (MeV) using (1) cylinder with no-self absorption, (2) truncated cone with no self-absorption, (3) truncated cone with self absorption (monte carlo program), (4) truncated cone with self-absorption (equation 6.4), and (5) truncated cone with self-absorption (actual radius 5 μm).

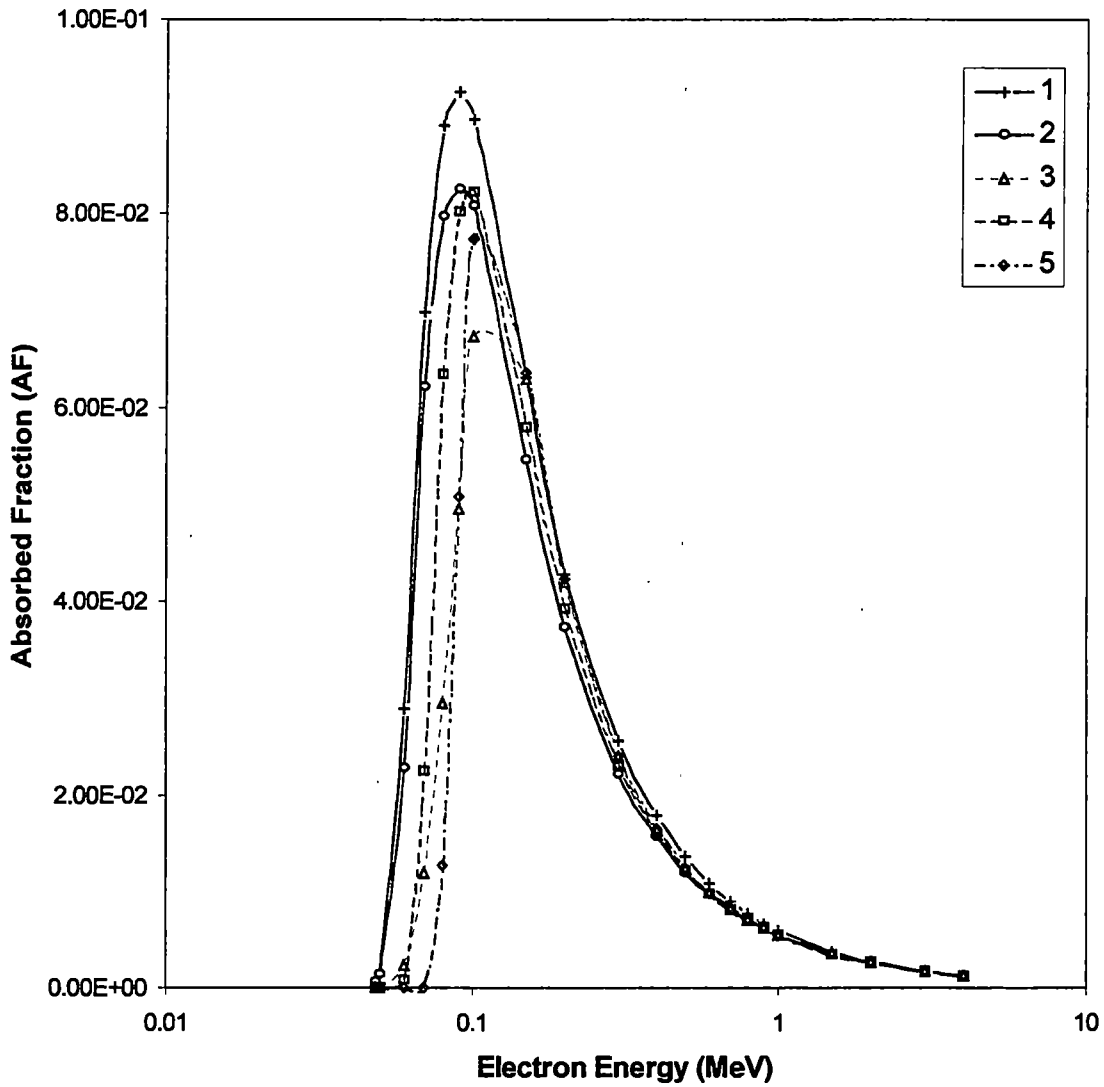


Figure 6.22 Electron absorbed fraction vs. energy (MeV) using (1) cylinder with no-self absorption, (2) truncated cone with no self-absorption, (3) truncated cone with self absorption (monte carlo program), (4) truncated cone with self-absorption (equation 6.4), and (5) truncated cone with self-absorption (actual radius 20 μm).

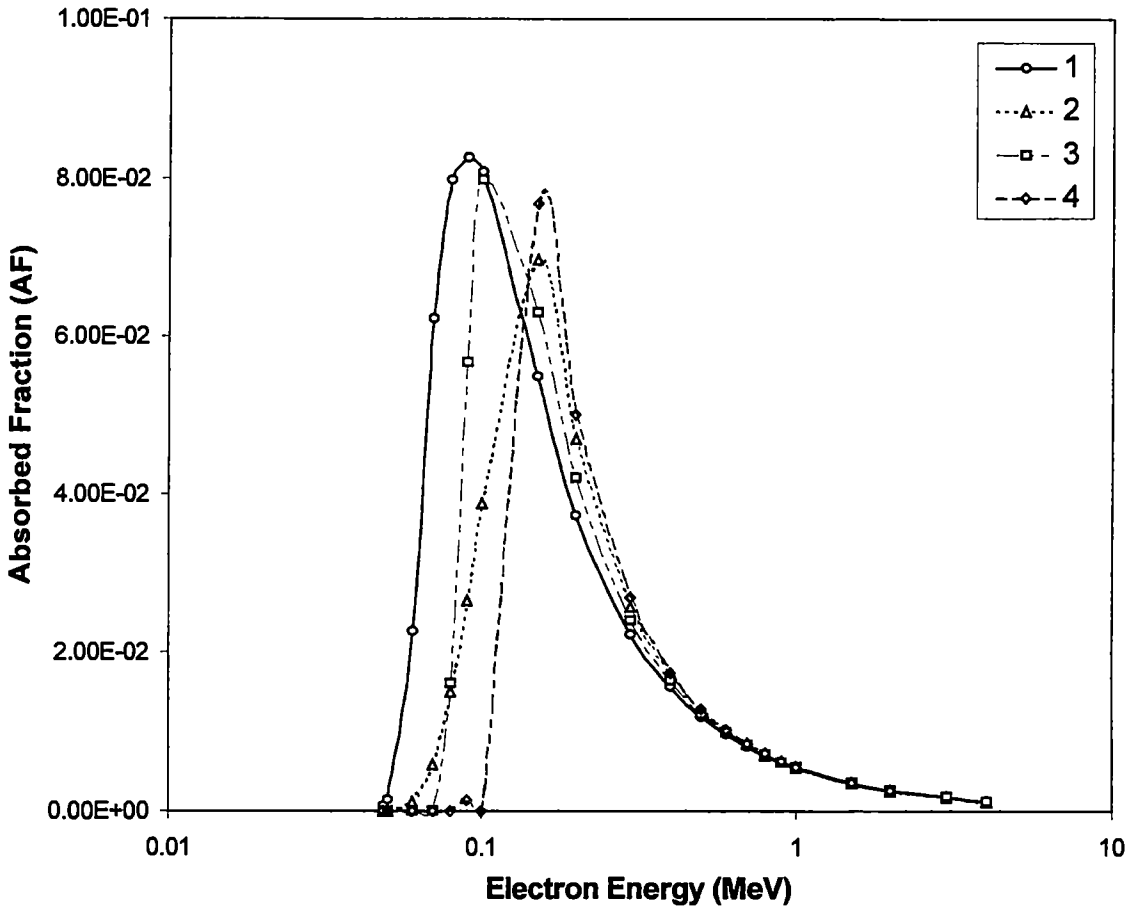


Figure 6.23 Electron absorbed fraction vs. energy (MeV) using (1) truncated cone with no self-absorption, (2) truncated cone with self absorption (monte carlo program), (3) truncated cone with self-absorption (equation 6.4), and (4) truncated cone with self-absorption (actual radius 50 μm).

6.9.2 Discussion

From Figures 6.20, 6.21, 6.22, and 6.23, the variations in electron absorbed fraction increase as the dust particle radius increases. In general, the electron absorbed fractions are smaller when self-absorption in the dust particles is included. Also, there is not much variation in the electron absorbed fractions estimated using Monte Carlo methods, equation 6.4 or the actual dust particle radius for the 2.5 μm dust particle. As the dust particle radius increases, there are substantial variations in the electron absorbed fractions estimated using the various techniques, especially for energies less than the peak energy near 0.1 MeV.

6.10 Code, Geometry and Dust Effects on the Electron Absorbed Fraction

The dust particle sizes present in some working areas may be relatively large (e.g., Uranium mining site). Therefore, dust particle size should be considered when estimating the electron absorbed fraction.

If the electron absorbed fractions obtained in chapter 4 for the cylinder model using the MCNP4B code are compared to the ones obtained using the EGS4 code, then the electron absorbed fraction is reduced by a factor of 1.25 (due to code differences). Moreover this electron absorbed fraction is reduced again in chapter 5,

by a factor of 1.27, due to the model change (truncated cone vs. cylinder). However, if we consider a dust particle of 20 μm radius in the working place, then from Table 6.56 in Appendix D the total electron absorbed fraction is further reduced between 2.3 and 16.7. Figure 6.24 illustrates the differences between the electron absorbed fraction for cylinder model using the EGS4 code without self-absorption in the dust particle and the electron absorbed fraction obtained for the truncated cone with self-absorption by a dust particle with a 20 μm radius estimated using the MCNP4B code.

6.11 Conclusions

In this chapter we investigated the effects of self-absorption as a function of dust particle size on the electron absorbed fraction. This is done by creating a code using Matlab® software, which generate electrons anywhere between the spherical dust particle center and its surface. Then we calculate the distance the electron will travel in a straight line to the surface and estimate the energy lost by the electron. This energy loss is subtracted from the electron initial energy. An ensemble of 100,000 electrons is generated and the electron absorbed fraction using the cylinder and truncated cone models are used to calculate the new electron absorbed fraction for each electron. Then, the average electron absorbed fraction for each energy is estimated. The new electron absorbed fractions (for cylinder model) are compared

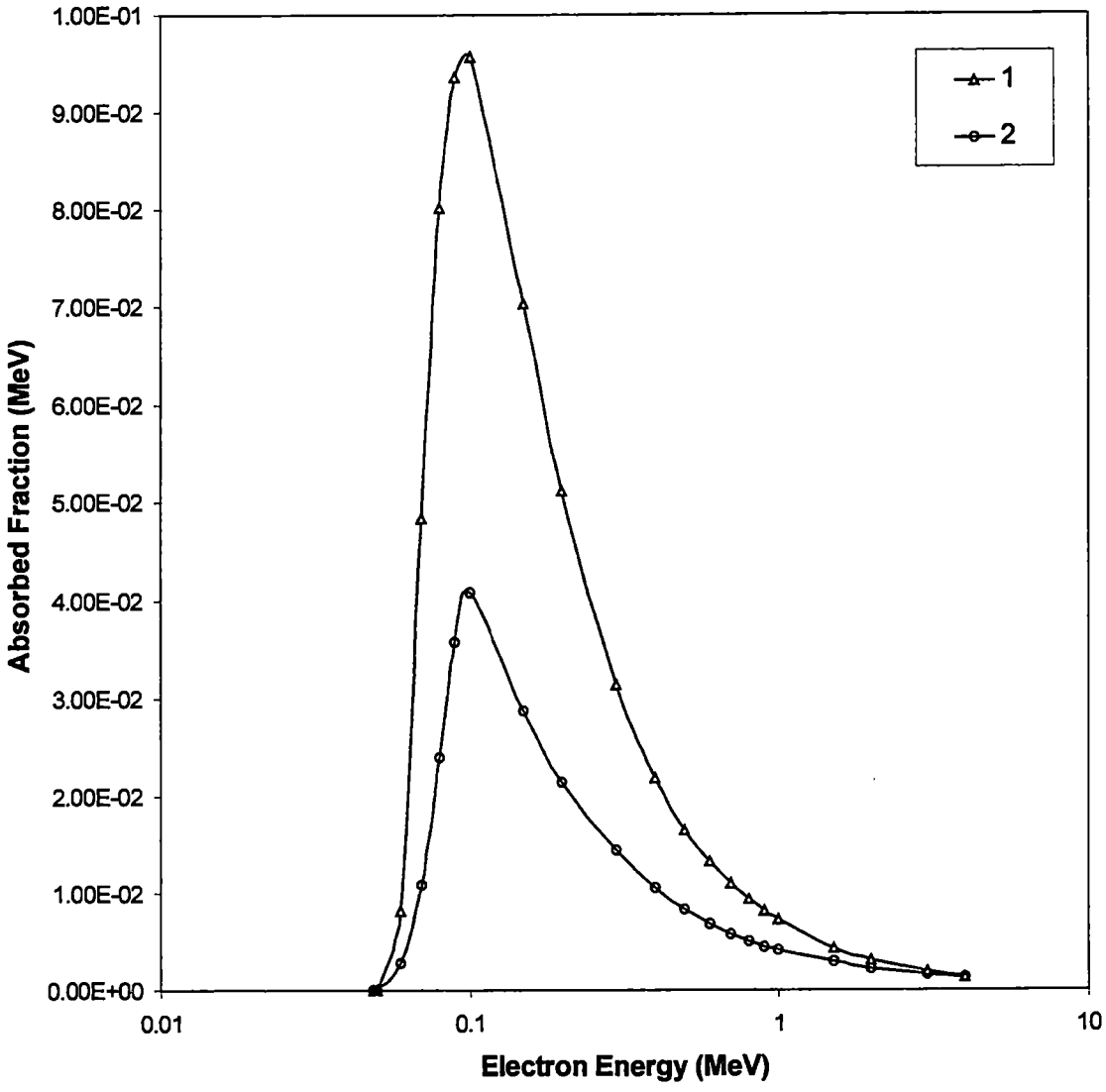


Figure 6.24 Comparison of the electron absorbed fraction for the cylinder model using (1) EGS4 code in the absence of self-absorption and the electron absorbed fraction obtained with (2) MCNP4B for a truncated cone with self-absorption by a 20 μm dust particle.

with the electron absorbed fractions obtained from ICRP Publication 66 for all energies. The conclusion is that self-absorption in dust has a significant effect on the electron absorbed fraction. The magnitude of the effect is dependent on the initial electron energy and the dust particle radius. Comparing the electron absorbed fractions obtained for truncated cone model, using MCNP4B, with the self-absorption in a dust particle of 20 μm, to the electron absorbed fractions obtained using EGS4 for a cylinder model with no self-absorption, shows that the electron absorbed fractions obtained in the former case are reduced by factors between 2.3 and 16.7 depending on the electron energy. Therefore to obtain more reliable electron absorbed fractions one should consider dust particle sizes when estimating the electron absorbed fractions in ET_1 and include the effects of self-absorption by these particles.

CHAPTER 7

Summary, Conclusions and Recommendations for Future Work

7.1 Summary and Conclusions

Possible causes of the larger equivalent doses to the anterior nose, previously estimated for inhaled beta and alpha emitters using the ICRP Publication 66 respiratory tract model have been investigated. First, estimates of the electron absorbed fractions from inhaled beta emitters were made using the MCNP4B code and the ICRP 66 model instead of EGS4 code used previously. Only small differences (≤20%) were noted at energies above 0.075 MeV, indicating that the EGS4 code was not the source of the unrealistically larger effective dose estimates. Varying the radius of the cylindrical geometry used in ICRP Publication 66 results in significant variations in the calculated electron absorbed fractions. These results indicate that a single anterior nose (ET_1) size is not sufficient to describe variations due to gender, age, and ethnic background. We proposed a new, more realistic model for the anterior nose using geometry based on a frustum of a cone. Varying the source location (upper part of the cone versus lower part) and the truncated cone size (bottom radius) produces significant variations in electron absorbed fractions calculated using the MCNP4B computer code. All of these results indicate that more

realistic estimates of electron absorbed fractions are obtained with the truncated cone model. However, the newer electron absorbed fraction estimates will not eliminate the apparent overestimates in effective dose to the basal cell layer in the ET_1 region.

For the first time, effects of beta self-absorption in the dust particles containing the beta-emitting radionuclides are investigated. Substantial reductions (nearly a factor of 16.7) in electron absorbed fraction estimates, depending on the energy, are obtained when self-absorption is included in the model. Taken together, the use of the MCNP4B code, the new frustum of a cone geometry, and incorporation of beta self-absorption in dust particles results in a very large reduction in electron absorbed fraction, which results in a large reduction in effective dose to the basal cells in the ET_1 region.

Nevertheless, additional work is needed since the estimated electron absorbed fractions are still much larger (nearly an order of magnitude) than values that are reasonable for these radiation sources

7.2 Recommendations for Future Work

The research presented in this dissertation is in fact the first step in investigating reasons for the large effective dose estimates to the extrathoracic region (ET_1) of the Human Respiratory Tract model (HRTM) developed in ICRP Publication

66. The electron absorbed fractions obtained in this work are reduced by a factor of 16.7 from the values published in ICRP Publication 66. However, even considering this reduction, the equivalent dose to the extrathoracic region is still high. Since electron absorbed fraction is one of several parameters involved in the dose calculation to the basal cells in the extrathoracic region (ET_1), the following are some recommendations for future research:

1. Investigate the effects of flow rate during the nose-breathing mode on the distribution of the dust particle deposition in the extrathoracic region (ET_1).

2. Since the anterior nose is the first filter in the human respiratory track model, it is play a major rule in estimating the equivalent dose to the other part of the respiratory track and to itself. Therefore, breathing habit (nose vs. mouth breathing) is essential and must be investigated correctly in order to estimate the concentration of the radioactive materials deposited on the inner surface of the extrathoracic region (ET_1).

3. Investigate the microscopic vs. macroscopic concepts used to calculate the electron absorbed fractions, especially if the region of interest has a very small mass. MCNP4B uses the stopping power (total and

collision) to calculate the E step and the energy lost along an electron track respectively. The tally *F8 output gives the energy deposition in the volume (region of interest). Since the target volume in this research is very small (20 cm^2 area and 10 μm thick), it is not necessarily true that the energy lost by the traversing particles is the same as the energy absorbed in this target region because some of the energy lost may escape this small volume. Therefore, the actual electron absorbed fraction could be less than the obtained one and further investigation is needed in this area.

4. The weighting factor assigned to the extrathoracic region (ET_1) is obtained based on the assumption that the anterior nose (ET_1) sensitivity is no different from the sensitivity of the skin elsewhere. A future investigation should attempt to find a new weighting factor since the inner surface of the anterior nose is not similar to skin (i.e., the depth of the receptor assumed in ICRP Publication 66 is 40 μm vs. 70 μm in the skin).

5. Since the electron absorbed fraction using the truncated cone is dependent on the source location, further investigation is needed to adjust the deposition fraction for different aerosol diameters.

REFERENCES

Ackerman, M. J. Accessing the visible human project. D-lib Magazine: The magazine of the digital library forum. 1995. http://www.dlib.org.

Batsaki,J.G (1976)" *Tumors of the head and neck. Clinical and pathological considerations".* Williams and Wilkins, Baltimore, Maryland, p. 124.

Bielajew, A. F.; Rogers, D. W. O. PRESTA, The parameter reduced electron-step size transport algorithm for electron Monte Carlo transport. National Research Council of Canada. Publication PIRS-0042; 1991.

Bond, J.A., Harakema, J.R., and Russwll, V.I (1988). "Regional distribution of xenobiotic metabolizing enzymes in respiratory airway of dogs," Drug Metab. Dispos. 16, 116-124.

Brin, L., Huband, J., Miller, J., Potter, L. K., Price,M., Kimbell, J., and Kepler, G.M. (1997). "Shape-based mathematics modeling of human nasal passage. *Proceeding, NCSU 1996 Industrial Mathematics Modeling Workshop For Graduate Students, CRSC-TR97-8 37-66.*

Cashwell, E. D., Neergaad, J. R., Evertt, C. J., Schrandt, R. G., Taylor, W. M., and Turner, G. D. "Monte Carlo Photon Codes: MCG and MCP," Los Alamos Scintific Laboratory Report, LA-5157-MS (March 1973).

Cheng, Kuo-His; Yung-Sing Cheng, Hsu-Chi Yeh; Raymond A. Guilmette; Steven Q. Simpson; Yi-Hsin Yang; and David L. Swift. "In vivo measurements of nasal airway dimensions and ultrafine aerosol deposition in the human nasal and oral airways." *J. Aerosol Sci.* Vol.27, No. 5,pp.785-801. 1996.

Eckerman K.F., Ryman J.C.,Tanner A.C., and Kerr G.D. (1986). Traversal of cells by radiation and absorbed fraction estimates for electrons and alpha particles. Proceedings of the Fourth International Radiopharmaceutical Dosimetry Symposium, edited by A.T. Schlafke-Stelson and E.E. Watson, pp. 67-81, CONF-851113-(DE86010102), 1986.

Eckerman K.F., Ryman J.C. (1993). External exposure to radionuclides in air, water, and soil. Federal Guidance Report No. 12, EPA-402-R-93-081 (Oak Ridge National Laboratory, Oak Ridge, TN; U.S. Environmental Protection Agency, Washington, DC).

Etherington G., Smith J.R.H., Baily M.R., Dorrian M.D., Shutt A.L., and Youngman M.J. (1998). "Deposition and clearance of inhaled particles in the human nasal passage: Implications for dose assessment." *Radiat. Prot. Dosim.* 79(1-3): 249-52.

Evans R.D., Keane A.T., Kolenkow K., Neal W.R., and Shanahan M.M. (1969). "Radiogenic tumors in the radium and mesothorium cases studies at MIT. In: *Delayed Effects of Bone-Seeking Radionuclides.* pp. 157-194 (Eds. Mays. C. W.,Jee, W. S., Lioyd,

R. D., Stover, B. J., Dougherty, J. H., and Taylor, G. N.). University of Utah Press, Salt Lake City, Utah.

G. Compte de Buffon, "Essai d'arithmetique morale," *Supplement a la Naturelle,* Vol. 4, 1777.

Harkema, J. R., Plopper, C.G., Hyde, D.M., Wilson, D. W., ST. George, J.A. and Womg, V.J. (1987). "Nonolfactory surface epithelium of the nasal cavity of the bonnet money: A morphologic and morphometric study of the transitional and respiratory epithelium." Health Phys. 23, 771-782.

Hendricks, J. S., Briesmeister, E. F. "Recent MCNP Development," *IEEE Transactions on Nuclear Scince*, 39, 4, 1035-1040 (August 1992).

Herman Kahn, "Modification of the Monte Carlo Method," *Proceedings, Seminar on Scientific Computation,* Nov. 1949, IBM, New York, 20-27 (1950).

International Commission on Radiological Protection (ICRP). ICRP Report of Committee II, p. 153. 1959.

International Commission on Radiological Protection (ICRP). Recommendations of the International Commission on Radiological Protection. ICRP Publication 10. Report of

Committee IV on evaluation of radiation doses to body tissues from internal contamination due to occupational exposure, 1968.

International Commission on Radiation Protection (ICRP). *Limits for Intakes of Radionuclides by Workers,* ICRP Publication 30. Annals of the ICRP 2(3/4). 1979.

International Commission on Radiation Protection (ICRP). *Human Respiratory Tract Model for Radiological Protection.* ICRP Publication 66, Ann. ICRP 24: (1-482);1994.

International Commission on Radiation Units and Measurements (ICRU). *Photon, Electron, Proton and Neutron Interaction Data for Body Tissue.* ICRU Report 46, p. 11. 1991

Jarup L., Bellander T., Hogstedt C. and Spang G., " Mortality and cancer incidence in Swedish battery workers exposed to cadmium and nickel ". *Occupational Environmental Medicine.* Vol. 55 (11): 755-9. Nov; 1998.

Lewis E.E., Miller Jr., W.F., Computational methods of neutron transport. American Nuclear Society Inc. La Grange Park, Illinois; 1993: 322-323.

Lodde J.P., Grangier Y., Le Roux P., and Fabre E. " Sclerodermiform basal cell carcinoma. A propos of a study of 83 cases. *Ann Chir Plast Esrhet* (1998) Aug; 43(4): 373-82.

National Council on Radiation Protection and Measurements (NCRP). *Deposition, Retention and Dosimetry of Inhaled Radioactive Substances.* NCRP Report No. 125; (1-253); 1997.

National Council on Radiation Protection and Measurements (NCRP). *Evaluation The Reliability of Biokinetic and Dosimetric Models and Parameters Used to Assess Individual Doses For Risk Assessment Purposes.* NCRP Commentary No. 15. P. 26. 1998.

Necie Grant Cooper, Ed., *From Cardinal to Chaso-Reflection on the Life and Legacy of Stanislaw Ulam,* Cambridge University Press, New York (1989).

Nelson C.B., Phipps A., Silk T. and Kendall G.M. The ICRP Publication 60 Formulation of Effective Dose and Contribution to Effective Dose in Internal Dosimetry. *Radiat. Prot. Dosim.* 71: (33-40). 1997.

Nelson, W. R.; Hirayama, H; Rogers, D. W. O. "The EGS4 Code System". Report SLAC-265-UC-32; December 1985.

Nationa Library of Medicine. U.S. Board of Regents. Electronic imaging: Report of the Board of Regents. Bethesda, MD: National Library of Medicine; NIH Publication 90-2197; 1990.

Phalen, R. F., Oldham, M. J., Beaucage, C. B., Crocker, T. T. and Mortensen, J. D. Postnatal enlargement of human tracheobronchial airways and implications for particle depostion. *Anat. Rec.* 212, 368-380. 1985.

Robert R. Johnson, "A General Monte Carlo Neutronics Code," Los Alamos Scintific Laboratory Report, LAMS-2856 (March 1963).

Subramaniam, Ravi. P.; Regina B. Richardson; Kevin T. Morgan; and Julia S. Kimbell. "Computational fluid dynamics simulations of inspiratory airway in the human nose and nasopharynx". *J. Inhalation Toxicology, 10:91-120.* 1998.

Swift, D. L. Age-related scaling for aerosol and vapor deposition in the upper airways of humans. *Health Phys.* **57** (Suppl.1), 293-297. 1989.

Yu, C. P., and Xu, G. B. (1987). Predicted deposition of diesel particles in young humans. *J. Aerosol Sci.* **18**, 419-429.

APPENDICES*

* All materials are on CD-ROM in Pocket.

INTERNATIONAL COMMISSION ON RADIOLOGICAL PROTECTION

Address: ICRP, SE-171 16 STOCKHOLM, Sweden
Tel: +46 8 729 7275 Fax: +46 8 729 7298
E-mail: jack.valentin@ssi.se

Dr Hanna M Moussa
University of Tennessee, Knoxville
Via e-mail

Our ref.: 51/286/99

28 November 2000

Permission to publish material from an ICRP Publication
Your ref.: E-mail 1999-11-25

Dear Dr Moussa,

Thanks for your e-mail requesting permission to reproduce some material from ICRP Publications.

On behalf of ICRP, I grant you permission to re-publish figures and tables from ICPR Publications 2, 30, 66, and 71, as detailed in your e-mail. As a condition, you must give proper references ('Reproduced by kind permission from ICRP Publication XX, Annals of the ICRP YY', or similar).

If reasonable, we would appreciate receiving a copy of the paper after publication. (We do realise that for large publications or papers with material from many sources, it would be difficult for the authors to supply copies).

Best wishes,

Yours sincerely,

Dr J Valentin
Scientific Secretary, ICRP

Chairman: Professor R H Clarke Scientific Secretary: Dr J Valentin

VITA

Hanna M. Moussa was born in a small Syrian village called Yazidiat Hamdaan, near the city of Safeta on October 13, 1957. There he received his education through high school. In 1975 he decided to join the army where he passed his high school examination and graduated from military college with a bachelor's degree. He became a lieutenant in 1980 and served in the army until 1984. He then went to Argentina before joining his family in the United States in 1985. He enrolled in a BS/MS degree program in the Department of Physics at the University of Massachusetts-Lowell in 1986. He received his bachelor's degree in Health Physics in May 1990 and his Master's degree in Radiological Sciences in August 1991. He was then accepted in 1993 into the Ph.D. Program in Mechanical Engineering at Georgia Tech. One semester later he transferred to the University of Tennessee. From 1994 to 1997 he was a teaching assistant at UT and developed Health Physics laboratories for graduate and undergraduate nuclear engineering courses. Since 1997 he has being employed at the University Radiation Safety Office. He was awarded his Ph.D. degree in Nuclear Engineering in December 2000.